Synthesis and Electronic Device Applications of Two-dimensional Materials

Juwon Lee

St. Anne's College

Department of Engineering Science

University of Oxford

DPhil Thesis

Hilary Term

2019

Abstract

Since it was first demonstrated that graphene could be successfully exfoliated from a graphite flake in 2004, two-dimensional materials have emerged as one of the most promising candidate materials for future electronic and optoelectronic applications due to their unique electrical and optical properties. However, graphene has been shown to possess almost no electronic band gap, which makes it unsuitable as a channel material in transistors because it cannot be used to switch off the transistors effectively. Transition metal dichalcogenides (TMDCs), on the other hand, have recently attracted tremendous attention because certain types of TMDC monolayers such as MoS_2 and WS_2 have large electronic band gaps, suitable for use in electronic devices.

In this thesis, chemical vapour deposition (CVD) of graphene is studied as a preliminary experiment for the subsequent growth of TMDC monolayers in order to gain an understanding of which parameters are important in the growth process. In this work, centimetre-scale graphene is successfully synthesized and a triboelectric nanogenerator is employed as a simple demonstration of an electronic application.

Secondly, a thermally stable synthesis procedure for growing a uniform and large-area TMDC monolayer with large-sized single crystal grains is studied based upon a solution-processed precursor deposition technique. With this synthesis approach, the nucleation density is found to dramatically decrease because of the low supersaturation level. In addition, vertically-stacked MoS_2/WS_2 heterostructure devices, fabricated using this new synthetic technique, show rectifying properties and exhibit a fast photoresponse and a high photoresponsivity due to a unipolar n-n heterojunction.

In the following chapter, a facile one-step CVD process for the MoS_2/WS_2 heterostructures and $Mo_{1-x}W_xS_2$ alloys is demonstrated through the precise control of the timing that the precursors are introduced as well as the supersaturation level of the precursors. The heterostructures grown using this one-step method are found to have a large crystal size and a clean interface. In addition, alloyed structures are intentionally obtained in the core, the shell regions of the lateral heterostructures or over the entire region of the monolayer by controlling the relative amounts of vaporised precursors and the growth temperature.

Finally, a monolayer MoS_2 optoelectronic memory device using artificially-structured charge trap layers is presented. The charge trap sites lead to localized electronic states that serve as a basis for electrically-induced charge trapping and optically-mediated charge release. The optical memory devices exhibit excellent photo-responsive memory characteristics with a large linear dynamic range and a long storage lifetime.

The work presented in this thesis investigates various growth strategies for synthesizing highly crystalline and large-area TMDC monolayers, and also demonstrates the realization of TMDC monolayer devices. These results provide a significant step forward in the development of future electronic and optoelectronic devices.

Acknowledgements

The research would not have been possible without the help of many supportive people whom I would like to acknowledge and thank. Above all, I want to express my gratitude to my first supervisor Professor Jong Min Kim, who left Oxford in 2016. I really appreciate the chance he gave me by accepting me as his student for this research. I was lucky to take the opportunity to work with him. I really appreciate Prof. Kim for his invaluable guidance and thoughtful suggestions throughout my research.

Indubitably, I want to thank my supervisors, Professor SeungNam Cha, Dr. Jung Inn Sohn, and Professor Stephen M. Morris. It has been an honour and pleasure to work with you all. I am immensely grateful to all your guidance, discussions, and great contribution of time, ideas and effort to encourage me to step forward and make my DPhil experience productive. The joy and enthusiasm you have shown for your research always motivated me. I also thank you all for the excellent work atmosphere you have fostered in the group and department.

I would also like to thank the following people in Oxford:

Dr. Jong Bae Park, Dr. Byung-Sung Kim, and Dr. Hyunchae Chun for their support and guidance when I first joined the Nano Science & Technology Group in 2013. Due to their help I was able to start my research without much difficulty and easily adjust myself to the research environment.

Yuljae Cho, who joined Nano Science & Technology together with me in 2013, for his considerate support that has been immensely helpful for me throughout the DPhil course.

Young-woo Lee, Sangyeon Park, John Hong, Paul Giraud, A-Rang Jang, Sanghyo Lee, Bo Hou for their helpful discussions which have been a source of inspiration and certainly improved the quality of my research.

Furthermore, I kindly acknowledge the Korean Government for the generous financial support of my DPhil. I would also like to thank the Department of Engineering Science and St Anne's College for their continuous support.

Most importantly, I express my love and gratefulness to my wonderful wife, Mikyeong, for her patience and understanding. Finally, I would like to express my deepest gratitude to my mother for her trust in me and all her sacrifices. To all of them I cannot thank you enough.

Table of Contents

List of Figures

List of Tables

1. Introduction

1.1. Motivation for the thesis

Since silicon-based transistors were invented, the performance of electronic devices has improved dramatically every year. These performance improvements have been mainly based on the reduction in the size of field-effect transistors (FET), which has enabled highly integrated circuit designs. Today, the gate lengths of metal-oxide-semiconductor FETs have decreased down to a length scale of the order of several tens of nanometres.[1] As a result, billions of transistors can be integrated onto an ultra-small logic chip, and can be operated at a frequency of hundreds of gigahertz. However, the reduction in size of silicon FETs is expected to reach a limit in the near future. In addition, the stiffness of silicon-based devices makes it difficult to implement them in future flexible and transparent devices. For these reasons, a large number of research teams are currently attempting to discover a new way to overcome the limitations faced with current silicon-based electronics. One approach is the introduction of completely new paradigms such as spintronics[2] and valleytronics.[3] Another avenue is to find new types of materials that exhibit unique properties that are not found in silicon, which can potentially have a more immediate impact in practical electronics and optoelectronics devices. In this respect, atomically thin two-dimensional (2D) materials have emerged as leading candidates to achieve this goal because of their unique electrical and optical properties.

Graphene became the first 2D material to be studied since it was successfully exfoliated from graphite flakes in 2004.[4] It has been reported that graphene has an ultra-thin thickness of ~0.5 nm and that it exhibits an extremely high mobility up to 200,000 $cm^2 V^{-1}$

s^{-1}.[5-6] However, graphene has almost no electronic band gap, thus it behaves as a semi-metal, which makes it difficult to switch-off electronic devices properly when it is used as a semiconducting channel material. Considerable efforts have been made to open up an electronic band gap in graphene,[7-9] but this has always led to a sacrifice of the high mobility, which is one of the primary advantages of the material, and the resultant band gap was always much less than that of silicon. Contrary to graphene, certain single-layer transition metal dichalcogenides (TMDCs) such as MoS_2 and WS_2 can be good alternative building blocks in transistors because some of these materials have semiconducting properties with a direct band gap. For example, a MoS_2 monolayer has a similar thickness to that of graphene, but has a larger band gap of 1.8 eV,[10] compared with that of silicon (1.1 eV). In addition, the charge mobility in this material is reported to be up to ~1,000 $cm^2 V^{-1} s^{-1}$ under vacuum and cryogenic conditions.[11] Even though this mobility is somewhat lower than the mobilities found in compound semiconductors such as GaAs (~8,500 $cm^2 V^{-1} s^{-1}$) and InP (~5,000 $cm^2 V^{-1} s^{-1}$), it is comparable to that of silicon (~1,000 $cm^2 V^{-1} s^{-1}$).

TMDCs have a MX_2-configuration (M = Mo, W, Nb, Ta; X = S, Se, Te) as shown in Figure 1-1 and have attracted widespread attention as a result of their considerable potential in the fields of electronics and optoelectronics.[12-13] Among these materials, the properties of molybdenum disulfide (MoS_2) and tungsten disulfide (WS_2) have been intensively studied over the past few years, because they have semiconducting characteristics that make them suitable for electronics applications in their 2D form. Although $MoSe_2$, WSe_2, $MoTe_2$, and WTe_2 also exhibit semiconducting properties, they have been less attractive because selenides are too toxic to be handled in the laboratory and tellurides are not stable at ambient temperatures. Therefore, in this thesis TMDC monolayers that are based upon MoS_2 and WS_2 are mainly investigated.

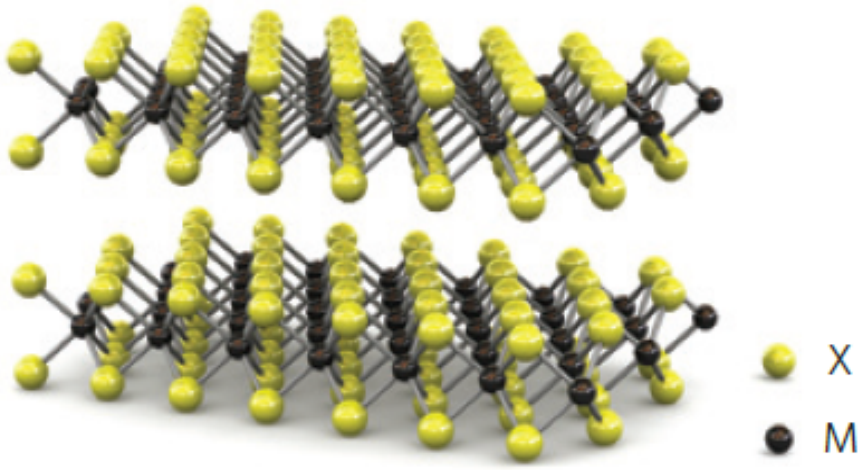

Figure 1-1. Atomic structure of TMDCs in the form of MX_2 (reproduced from ref [14]).

One of the critical obstacles for the use of 2D materials as electronic and optoelectronic applications is that it is difficult to synthesize large-area and high-crystalline 2D films. Mechanical exfoliation was usually used to obtain high-quality 2D monolayer flakes. However, in the case of mechanical exfoliation, it is not easy to increase the size of the monolayer over a hundred micrometres. Since the first report on chemical vapour deposition (CVD) of TMDC monolayers was published,[15] many research groups have utilized CVD techniques with powder-based precursors to grow TMDC monolayers as such approaches demonstrated the possibility of producing large-scale TMDC monolayer films with high-quality crystals.[16-17] However, it still remains a challenge to obtain large-scale TMDC monolayer films because it is difficult to control the vapour concentration of the solid-type precursors at high temperatures during the growth process. Therefore, there is a considerable need to devise a new method that allows for the facile adjustment of the concentration level in the CVD synthesis of large-scale TMDC monolayers.

On the other hand, it was predicted by density functional theory (DTF) calculations that type II heterojunctions could be formed with different TMDC monolayers.[18] It is known that type II heterojunctions can be used to fulfil an efficient separation of electron and hole pairs excited by photons, which is useful for fabricating optoelectronic devices. Although several vertically-stacked TMDC heterostructures were reported,[19-24] it is difficult to produce good-quality vertical TMDC heterostructures because the mismatch in the stacking angle between the monolayers as well as contaminants at the interface are unavoidable during the transfer process. The growth of lateral TMDC heterostructures synthesized by two-step growth have been also reported.[25-27] However, the crystal edges can be contaminated when they are exposed to ambient conditions between the first and the second growth process, which might induce a large number of defects near the interface. Therefore, it is desirable to introduce a new way to grow TMDC lateral heterostructures with a clean interface using a one-step process to avoid any contamination.

Since the demonstration that TMDC monolayers can be utilized for high-performance transistors, many electronic applications of TMDC monolayers have been reported.[23,28-30] However, the concept of an optoelectronic memory for practical image sensing based on TMDC monolayers has been rarely explored until recently. For image sensing, optoelectronic devices need to have the special requirement that they have to respond to exposure dose instead of exposure intensity in order to achieve complicated image processing. Ordinary photodetectors cannot meet this requirement because they usually only respond to the intensity of light. In addition, it is very important for image sensing devices to have a linear response to the exposure dosage so that the contrast of the original image can be represented accurately. For this reason, state-of-the-art image sensors such as charge-coupled devices (CCD) and complementary metal-oxide-semiconductor (CMOS) devices are usually designed to accumulate the photogenerated charge carriers

linearly during exposure. However, it is not easy to implement image sensors with general optical memory devices because they are usually not linearly responsive to exposure dose at high light power densities. Thus, the fabrication of CCD-like optical memory devices using atomically thin monolayer films, which use a potential well between the electrodes without a source-drain bias during light illumination and have a linear response to exposure dosage with a wide dynamic range, would be extremely valuable for the development of practical image sensors. More importantly, this approach can also provide the possibility of constructing flexible circuits based entirely on 2D materials along with the integration with other 2D material-based devices such as basic transistors and non-volatile electronic memories.

From the motivation explained above, the main objectives of the work presented in this thesis are:

A. To synthesize large-scale and high-quality TMDC monolayers using solution-processed precursor deposition that can control the supersaturation level of metal oxide precursors during the growth process;
B. To develop a one-step synthesis procedure to grow MoS_2/WS_2 heterostructures with a clean interface, and control the growth parameters to synthesize various types of MoS_2/WS_2 heterostructures and alloys;
C. To demonstrate a monolayer optical memory device and investigate its performance in order to address whether it can be used as a basic building block in image sensors that require a linear response to light exposure dosages.

1.2. History of 2D materials

In 1959, Richard Feynman gave his now famous lecture, "*There's plenty of room at the bottom*." In this lecture, he mentioned, "*What would the properties of materials be if we could really arrange the atoms the way we want them.*" Although this lecture is well-known for emphasizing the importance of nanotechnology, he also predicted the advent of 2D materials in the lecture. He asked, "*What could we do with layered structures with just the right layers*?"

Sporadic attempts to study 2D materials can be traced back to 1859. The British chemist, Benjamin Brodie, exposed graphite to strong acids and obtained what he called 'carbonic acid'.[31] It is now known that what he found was a suspension of tiny crystals of graphene oxide which consists of a graphene sheet densely covered with hydroxyl and epoxide groups.[32] Over the next decades, there were several papers published on investigating the laminated structure of graphite oxide. In 1916, the structure of graphite was identified by the powder diffraction method.[33] John Desmond Bernal also identified the layered structure of graphite, using the method of single-crystal diffraction in 1914.[34] Later, in 1947, Phil Wallace first calculated the band structure of graphene as a preliminary study to understand the electronic properties of bulk graphite.[35] The earliest transmission electron microscopy (TEM) images of few-layer graphite flakes down to a few nm in thickness were observed in 1948 by G. Ruess and F. Vogt, after drying a droplet of a graphene-oxide suspension on a TEM grid.[36] Subsequently, in 1962, Ulrich Hofmann and Hanns-Peter Boehm tried to observe the thinnest fragments of reduced graphite oxide and, finally, identified some of them as monolayers, even though their findings relied on a relative TEM

contrast which depends significantly on the focusing conditions. Furthermore, in 1986, Boehm *et al* introduced the term ‘graphene’, combining the word 'graphite' and the suffix ‘-ene’ which means polycyclic aromatic hydrocarbons.[37]

In addition to the TEM observations, there were some attempts to grow graphene. After John Grant and Blakely *et al* reported graphitic films grown epitaxially on Ru and Rh,[38] and on Ni,[39] respectively, the epitaxial growths on other metal substrates[40-42], insulating carbides[43-46] and graphite[47] followed. Efforts to obtain ultra-thin films of graphite by mechanical exfoliation were also introduced in 1990 by Heinrich Kurz's group which tried to exfoliate thin layers from graphite to study carrier dynamics in graphite.[48] However, monolayer graphene was not demonstrated before 2004.

Graphene was successfully exfoliated from a lump of bulk graphite with sticky tape by scientists at the University of Manchester (UK) in 2004.[4] Since then, graphene has received tremendous attention due to its unique properties such as high transparency and ultrahigh electrical mobility. The scientists who first exfoliated graphene and investigated its properties won the Nobel Prize in Physics in 2010 for their pioneering research. However, the band gap of graphene is almost non-existent, which means that it is very difficult to use it as a channel material in field-effect transistors. Consequently, many researchers have tried to introduce a gap in the electronic bands in graphene, although it is still a significant challenge to apply graphene to commercial transistor circuits.

Since research on graphene has become one of the leading topics in condensed matter physics, there have been similar attempts to mechanically exfoliate or directly synthesize monolayers from a variety of other materials that are known to have a layered structure. Even though the structures of these monolayers are very similar to that of graphene, the optical and electrical properties can be significantly different (Figure 1-2). For example,

diatomic hexagonal boron nitride monolayers, which have exactly the same hexagonal structure as graphene, exhibit insulating properties.[49] Among these materials, TMDC monolayers are emerging as one of the most promising candidates for electronic and optoelectronic devices because they have a sizable band gap in the visible range.

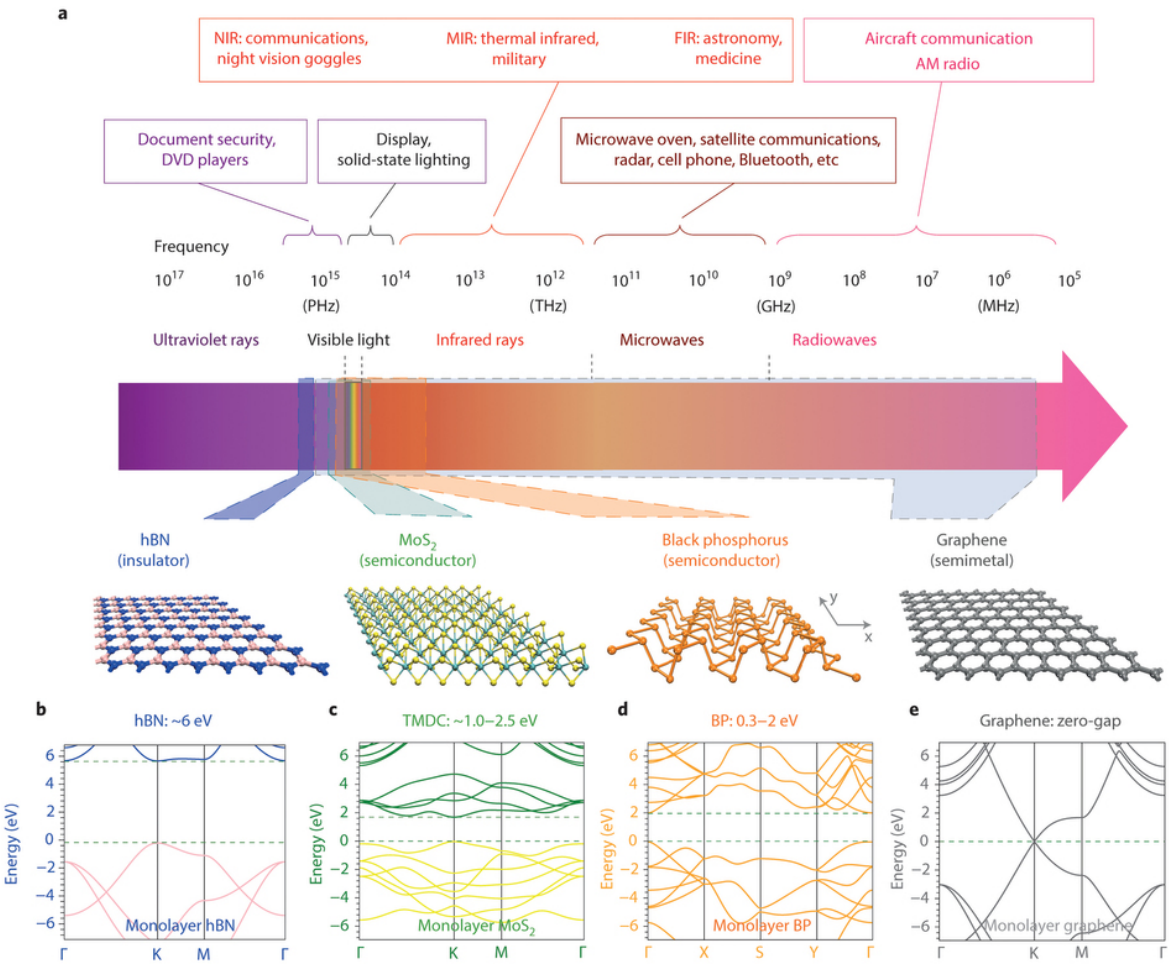

Figure 1-2. Various 2D materials, their corresponding spectral range and their electronic band structures (reproduced from ref[50]).

The number of research reports on 2D materials increases dramatically every year. Besides single monolayers, the investigation of heterostructures between 2D materials is becoming an attractive research area due to a variety of interesting phenomena occurring at

the interface, such as ultrafast charge transfer.[51] The heterostructures between semiconducting bulk materials have already played a crucial role in the modern electronics industry, and are currently being used for various electronic devices such as photodetectors,[52] solar cells,[53] and light-emitting diodes.[54] For example, in 2000, the Nobel Prize in Physics was awarded to Zhores I. Alferov and Herbert Kroemer for their work on developing the semiconductor heterostructures used in high-speed electronics and optoelectronics applications.[55]

Even though 2D materials are only one to three atoms thick, the weak van der Waals interlayer forces and the absence of dangling bonds between the layers make it possible to isolate a monolayer and stack it onto other 2D materials much more easily when compared to typical bulk semiconductor heterostructures. Thus, for the last few years, there have been many attempts to fabricate heterostructures with a variety of combinations between 2D materials so as to investigate their interesting physical properties.[56-57] For these reasons, 2D heterostructure devices are considered as very promising structures for the development of future electronic and optoelectronic devices.

1.3. Crystal structure of TMDC monolayers

Under ambient conditions, TMDC compounds (MX_2, M: transition metals, X: chalcogen atoms) have been reported to have three types of layered crystal structures as shown in Figure 1-3: the octahedral structure (1T phase), the trigonal prismatic structure (2H phase), and the trigonal prismatic structure with a different stacking order from the 2H phase (3R phase). The prefix '1', '2', '3' refers to the bulk stacking mode. All these crystal structure types have metal atom (M) layers that are sandwiched between two chalcogenide (X) layers. In their bulk form, TMDC compounds have been found to be composed of vertically stacked layers via weak van der Waals forces between the layers, which ensures that the surface is free from dangling bonds. In contrast, for the in-plane structure, the molybdenum and sulfur atoms are coupled by much stronger covalent bonds. However, the 1T phase of TMDC compounds usually displays metallic-like behaviour, while both the 2H and 3R types exhibit semiconducting behaviour. In the case of MoS_2, the 2H phase is thermodynamically stable and frequently observed in nature or when artificially synthesized, unlike the 1T and the 3R phases which are rarely found in nature or in the laboratory.

From the perspective of electronics applications, semiconducting materials that exhibit a band gap in the electronic structure can be much more interesting from a scientific point of view, compared with metallic ones. Therefore, research on TMDC materials has been mainly focused on the 2H phase, even though the 1T phase has received attention in terms of electrode applications in electronic devices and electrochemical energy storage.[58] In addition, when the thickness of the TMDC compound is reduced to a monolayer, the stacking order is meaningless and the 3R phase can no longer be described in the form of monolayers. Therefore, in terms of monolayers, only the 2H phase and the 1T phase have

been studied up to now. In particular, the semiconducting 2H phase has dominated the research area of TMDC monolayers.

In a MoS_2 monolayer, the thickness of each layer has been reported to be around 6.5 Å.[14,59] It is also found that the lattice constant, the covalent bond length of Mo-S, and the angle between the Mo and S atoms are 3.22 Å, 2.43 Å and 80.6°, respectively.[60-62] In addition, MoS_2 monolayers have a much higher Young's modulus of ~270 GPa than that of steel (~205 GPa).[63-64] As a result, they can therefore maintain their intrinsic properties even if they are bent to a radius of curvature of 0.75 mm.[64-65] These combined properties make MoS_2 monolayers particularly attractive for flexible electronic and optoelectronic devices.

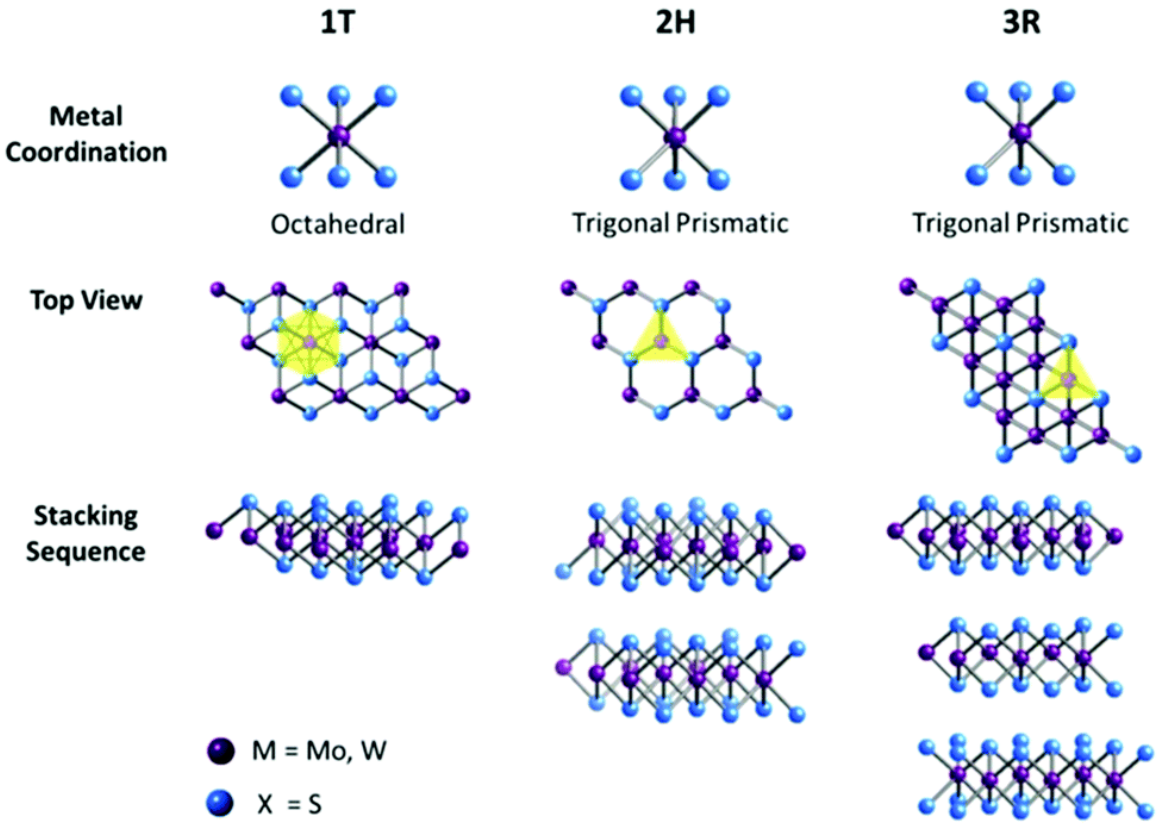

Figure 1-3. Crystal structures of TMDC monolayers (reproduced from ref[66]).

1.4. Vibrational properties of TMDC monolayers

It is known that Raman spectroscopy is one of the most useful and powerful tools to investigate the vibrational properties of materials. In TMDC materials, Raman spectroscopy is also commonly used to determine the number of the layers because the vibration of the atoms in the TMDC materials is easily affected by the change in the number of the layers. Theoretical analysis predicts that there are four Raman active vibration modes ($E^2_{2g} \approx 32$ cm^{-1}, $E_{1g} \approx 286$ cm^{-1}, $E^1_{2g} \approx 383$ cm^{-1}, and $A_{1g} \approx 408$ cm^{-1}), two IR active modes ($E^1_{1u} \approx 384$ cm^{-1}, $A_{2u} \approx 470$ cm^{-1}), and four silent modes ($B^2_{2g} \approx 58$ cm^{-1}, $E_{2u} \approx 287$ cm^{-1}, $B_{1u} \approx 403$ cm^{-1}, and $B^1_{2g} \approx 470$ cm^{-1}) in a 2H-MoS_2 crystal[67-69] (Figure 1-4). Only the E^2_{2g} mode is related to the interlayer vibration between adjacent layers while all the other modes involve intralayer vibration.

It is found that the two Raman active vibrational modes, the E^1_{2g} and A_{1g} peaks, are clearly observed in 2H-MoS_2 and used for investigating the number of the layers in the crystal. The E^1_{2g} mode originates from the opposite in-plane vibrational activity between the two sulfur atoms and the Mo atom, and the A_{1g} mode is related to the out-of-plane vibration of the sulfur atoms surrounding the Mo atom.[70] As a result, these two peaks are significantly sensitive to the number of layers. In general, the interlayer van der Waals interaction in MoS_2 tends to restrain the atomic vibrations and induce a strong restoring force between the atoms. Therefore, both the in-plane E^1_{2g} peak and the out-of-plane A_{1g} peak are expected to be stiffened or blue-shifted.[71] However, all the experiments on the vibrational analysis of MoS_2 crystals have shown that only the A_{1g} peak in the Raman spectrum is blue-shifted when the number of layers increases, while the E^1_{2g} peak is red-shifted, which is the opposite to the predictions.[72] This phenomenon can be explained by the stronger long-range

Coulombic interaction in a few-layer or multilayer crystal compared to the case of monolayers. As a result, the Raman frequency difference between the E^1_{2g} peak and the A_{1g} peak has been found to decrease from ~25 cm^{-1} in the bulk form (consisting of more than five layers) to ~19 cm^{-1} in a monolayer.[71,73] Although the thickness of the TMDC monolayers can be measured directly by using atomic force microscopy (AFM), Raman spectroscopy has become the most powerful tool to investigate the number of layers due to the change in the vibrational properties according to the thickness.

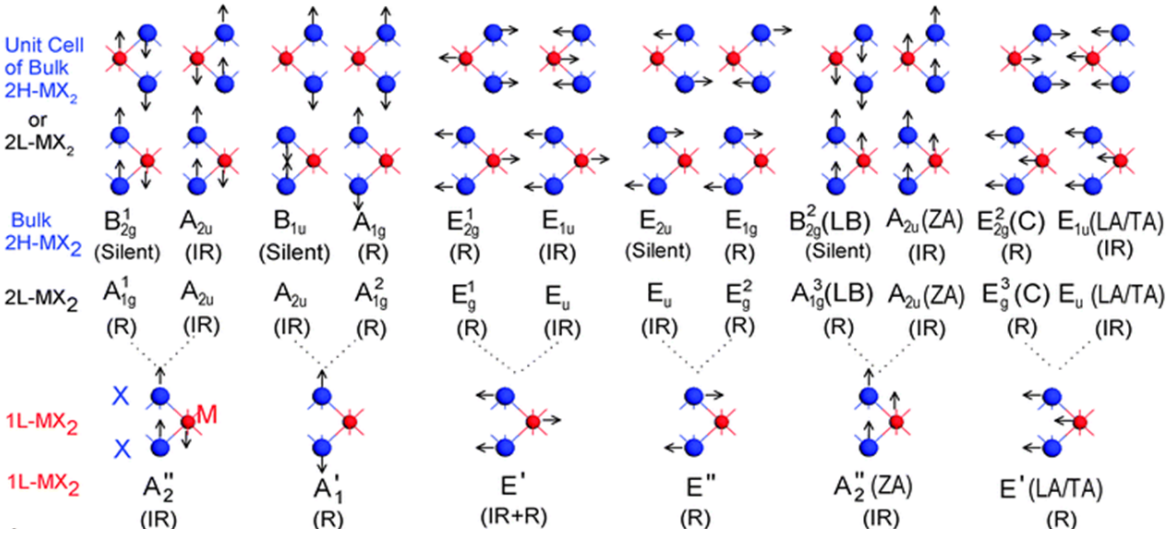

Figure 1-4. Vibrational modes of TMDCs (reproduced from ref[74]).

1.5. Electronic band structure of TMDC monolayers

An understanding of the electronic band structure is needed to predict and analyse the phenomena associated with the optical and electrical processes in a variety of electronic and optoelectronic devices. Theoretical analysis obtained from density functional theory (DFT)[75] shows that the valence band maximum (VBM) is located at the centre of the G point and the conduction band minimum (CBM) is found between the G and K point, which means that the bulk form of MoS_2 has an indirect band gap (Figure 1-5). However, a change in the electronic band is observed when the number of layers or the thickness of MoS_2 decreases to a monolayer. The difference in the energy levels at the K point, which is related to the direct excitonic properties, remains unchanged in both the conduction and the valence bands regardless of the thickness of the material. On the other hand, the conduction band level between the G and the K points, and the valence band level at the G point become much wider when the thickness decreases. As a result, if the thickness reduces to a monolayer, this energy level difference becomes larger than that of the indirect excitonic band gap at the K point, which means that the MoS_2 monolayer has a direct band gap of ~1.9 eV. The transition from the indirect to the direct band gap has also been found in other TMDC monolayers such as WS_2,[76] and can be explained by a quantum confinement effect when reducing the thickness to a monolayer. In addition, changes in the long-range Coulombic force and in the hybridization between the p_z orbitals of sulfur atoms and the *d*-orbitals of Mo atoms are also known to cause a change in the electronic band structure.[61,75]

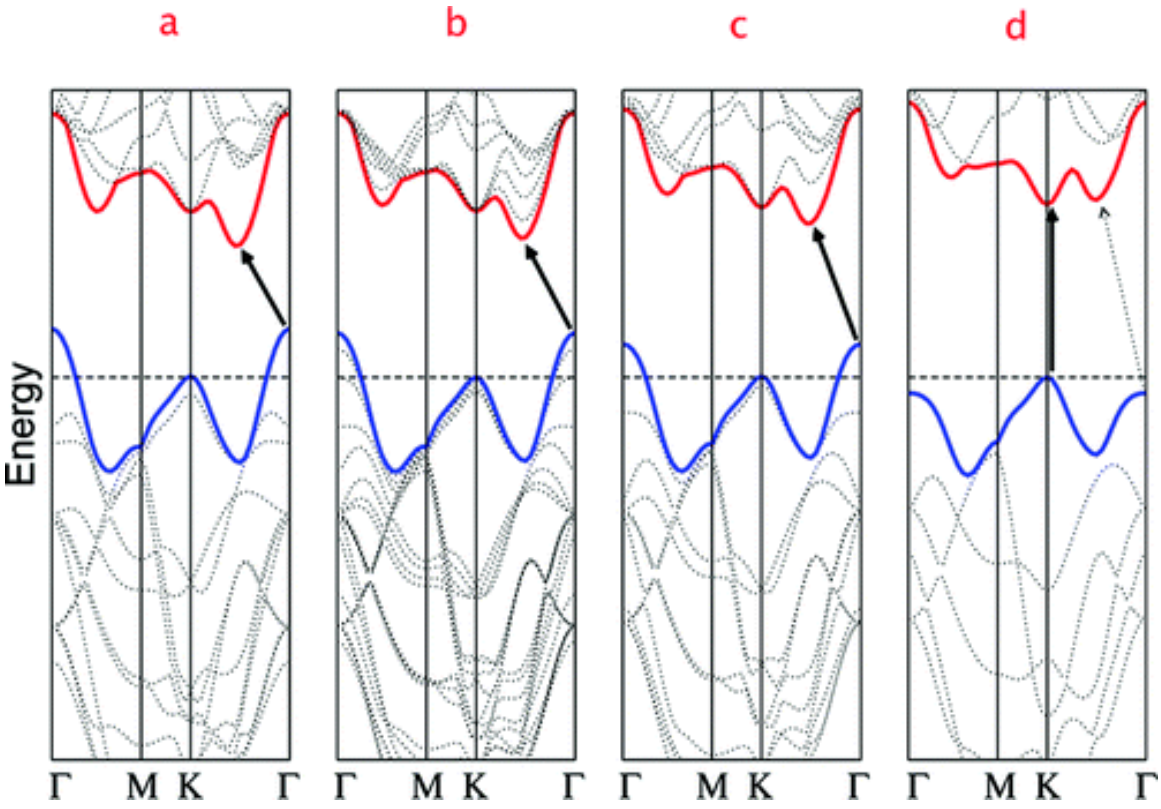

Figure 1-5. Indirect to direct transition in the electronic band structure of TMDCs (reproduced from ref[75]).

The transition from the indirect to the direct band gap of TMDC monolayers also changes the properties of the photoluminescence (PL). In the bulk form of MoS_2, PL is rarely observed even when the thickness of the MoS_2 decreases to only a few layers. However, the intensity of the PL in MoS_2 monolayers is found to be much larger than that of bulk MoS_2. It is known that an increase in the exciton binding energy from ~0.1 eV in the bulk to 1.1 eV in monolayers contributes to a dramatically-increased PL intensity.[77] Interestingly, two excitonic peaks can be easily identified in the PL spectra, with a more intense one at ~1.9 eV and a weaker one at ~ 2.05 eV, which are known as the A and B exciton peaks, respectively[10] (Figure 1-6). These two peaks originate from the band gaps at the K point,

and it is known that the energy splitting results from the spin-orbit coupling in the valence band.[10,78] The PL of the TMDC monolayers is easily affected by the environment such as underlying substrates and adsorbed gas molecules on the surface because of their high surface-to-volume ratio, which makes it easy to change the properties of the PL with chemical or electrical doping.[79] With different substrates, the doping level of the monolayer can be controlled and thus the intensity of the PL is modulated easily. In addition, the gate voltage can change the doping level. The chemical and electrical doping changes the relative intensity between the charged exciton (trion) and neutral exciton,[80] which is one of the reasons why the total intensity of the PL varies according to the doping level.

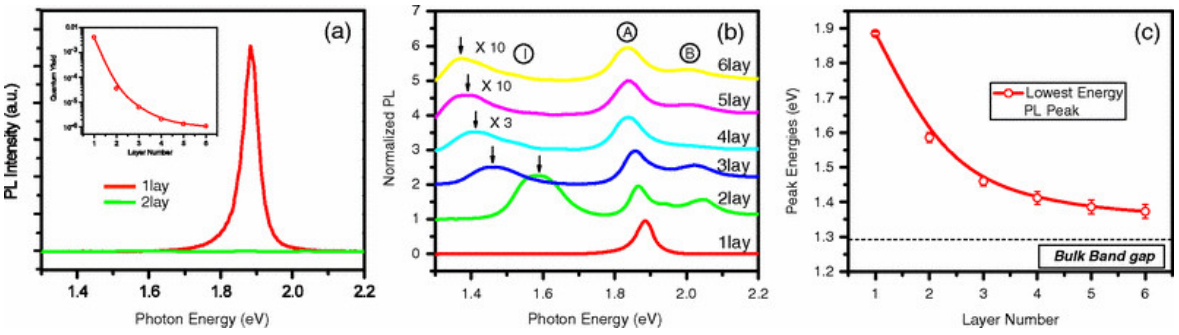

Figure 1-6. PL of MoS_2 monolayers according to the number of layers (reproduced from ref[10]).

1.6. Layout of the thesis

This thesis consists of six chapters focusing on the synthesis of atomically thin TMDC monolayers and their use in electronic and optoelectronic applications. Specifically, MoS_2 and WS_2 monolayers and their heterostructures are studied as representative examples of TMDC monolayers.

Chapter 1 has provided the motivation for the thesis, a brief history of 2D materials, and a broad overview of the properties of the 2D TMDC materials. Chapter 2 presents the preliminary experiments conducted with graphene. Graphene is the most well-known monolayer amongst the 2D materials. Even though it has been just over 10 years since graphene was first exfoliated from flakes to form a monolayer, there have been many reports on graphene over the last decade. Therefore, before beginning the studies on TMDC monolayers, the synthesis, transfer, characterization, and applications of graphene are discussed in this chapter.

Chapter 3 describes the synthesis procedure used for the MoS_2 monolayers and their fundamental vibrational properties and optical properties. In particular, this study includes the thermodynamically stable synthesis procedure of the monolayers, using a solution-processed precursor deposition, and the understanding of growth dynamics and behaviour of the monolayers. How the supersaturation level of precursors affects the growth is explored in order to grow large-sized and high-quality TMDC monolayers. In addition, the properties of MoS_2/WS_2 vertical heterostructured devices are also investigated. Chapter 4 explores the generality of the solution-processed precursor deposition for synthesizing TMDC

heterostructures/alloys. Lateral MoS_2/WS_2, MoS_2/alloy, alloy/WS_2 heterostructures and $Mo_{1-x}W_xS_2$ alloys are synthesized by understanding and controlling different growth parameters. In particular, the bound excitons in $Mo_{1-x}W_xS_2$ alloys are studied using low-temperature PL measurements.

Chapter 5 presents a MoS_2 monolayer optical memory device with a surface treatment. The role of the intentionally-introduced charge trap layers between the monolayer and the substrate and the importance of the linear optical response are discussed in terms of the operating principle of the device. Finally, Chapter 6 summarizes the results of the experiments and the discussions, before presenting further work that could be explored in the future regarding the development of TMDC monolayers.

1.7. References

[1] H. Iwai. Roadmap for 22 nm and beyond. *Microelectronic Engineering* 86, 1520-1528 (2009).

[2] D. D. Awschalom, M. E. Flatté. Challenges for semiconductor spintronics. *Nature Physics* 3, 153-159 (2007).

[3] H. Zeng, J. Dai, W. Yao, D. Xiao, X. Cui. Valley polarization in MoS_2 monolayers by optical pumping. *Nature Nanotechnology* 7, 490-493 (2012).

[4] K. S. Novoselov, A. K. Geim, S. V. Morozov, D. Jiang, Y. Zhang, S. V. Dubonos, I. V. Grigorieva, A. A. Firsov. Electric field effect in atomically thin carbon films. *Science* 306, 666-669 (2004).

[5] J.-H. Chen, C. Jang, S. Xiao, M. Ishigami, M. S. Fuhrer. Intrinsic and extrinsic performance limits of graphene devices on SiO_2. *Nature Nanotechnology* 3, 206-209 (2008).

[6] A. Akturk, N. Goldsman. Electron transport and full-band electron-phonon interactions in graphene. *Journal of Applied Physics* 103, 53702 (2008).

[7] M. Y. Han, B. Özyilmaz, Y. Zhang, P. Kim. Energy band-gap engineering of graphene nanoribbons. *Physical Review Letters* 98, 206805 (2007).

[8] X. Li, X. Wang, L. Zhang, S. Lee, H. Dai. Chemically derived, ultrasmooth graphene nanoribbon semiconductors. *Science* 319, 1229-1232 (2008).

[9] Z. Chen, Y.-M. Lin, M. J. Rooks, P. Avouris. Graphene nano-ribbon electronics. *Physica E: Low-dimensional Systems and Nanostructures* 40, 228-232 (2007).

[10] K. F. Mak, C. Lee, J. Hone, J. Shan, T. F. Heinz. Atomically thin MoS_2: A new direct-gap semiconductor. *Physical Review Letters* 105, 136805 (2010).

[11] B. W. H. Baugher, H. O. H. Churchill, Y. Yang, P. Jarillo-Herrero. Intrinsic electronic transport properties of high-quality monolayer and bilayer MoS_2. *Nano Letters* 13 (2013).

[12] Q. Wang, K. Kalantar-Zadeh, A. Kis, J. N. Coleman, M. S. Strano. Electronics and optoelectronics of two-dimensional transition metal dichalcogenides. *Nature Nanotechnology* 7, 699-712 (2012).

[13] M. Chhowalla, H. Shin, G. Eda, L.-J. Li, K. Loh, H. Zhang. The chemistry of two-dimensional layered transition metal dichalcogenide nanosheets. *Nature Chemistry* 5, 263-275 (2013).

[14] B. Radisavljevic, A. Radenovic, J. Brivio, V. Giacometti, A. Kis. Single-layer MoS_2 transistors. *Nature Nanotechnology* 6, 147-150 (2011).

[15] Y. H. Lee, X. Q. Zhang, W. Zhang, M. T. Chang, C. T. Lin, K. D. Chang, Y. C. Yu, J. Wang, C. S. Chang, L. J. Li, T. W. Lin. Synthesis of large-area MoS2 atomic layers with chemical vapor deposition. *Advanced Materials* 24, 2320-2325 (2012).

[16] S. Najmaei, Z. Liu, W. Zhou, X. Zou, G. Shi, S. Lei, B. I. Yakobson, J.-C. Idrobo, P. M. Ajayan, J. Lou. Vapour phase growth and grain boundary structure of molybdenum disulphide atomic layers. *Nature Materials* 12, 754-759 (2013).

[17] A. M. van der Zande, P. Y. Huang, D. A. Chenet, T. C. Berkelbach, Y. You, G.-H. Lee, T. F. Heinz, D. R. Reichman, D. A. Muller, J. C. Hone. Grains and grain boundaries in highly crystalline monolayer molybdenum disulphide. *Nature Materials* 12, 554-561 (2013).

[18] J. Kang, S. Tongay, J. Zhou, J. Li, J. Wu. Band offsets and heterostructures of two-dimensional semiconductors. *Applied Physics Letters* 102, 12111 (2013).

[19] R. Cheng, D. Li, H. Zhou, C. Wang, A. Yin, S. Jiang, Y. Liu, Y. Chen, Y. Huang, X. Duan. Electroluminescence and photocurrent generation from atomically sharp WSe_2/MoS_2 heterojunction p–n diodes. *Nano Letters* 14, 5590-5597 (2014).

[20] C.-H. Lee, G.-H. Lee, A. M. van der Zande, W. Chen, Y. Li, M. Han, X. Cui, G. Arefe, C. Nuckolls, T. F. Heinz, J. Guo, J. Hone, P. Kim. Atomically thin p–n junctions with van der Waals heterointerfaces. *Nature Nanotechnology* 9, 676-681 (2014).

[21] M. M. Furchi, A. Pospischil, F. Libisch, J. Burgdörfer, T. Mueller. Photovoltaic effect in an electrically tunable van der Waals heterojunction. *Nano Letters* 14, 4785-4791 (2014).

[22] N. Choudhary, J. Park, J. Hwang, H.-S. Chung, K. H. Dumas, S. I. Khondaker, W. Choi, Y. Jung. Centimeter scale patterned growth of vertically stacked few layer only 2D MoS_2/WS_2 van der Waals heterostructure. *Scientific Reports* 6, 25456 (2016).

[23] Y. Xue, Y. Zhang, Y. Liu, H. Liu, J. Song, J. Sophia, J. Liu, Z. Xu, Q. Xu, Z. Wang, J. Zheng, Y. Liu, S. Li, Q. Bao. Scalable production of a few-layer MoS_2/WS_2

vertical heterojunction array and its application for photodetectors. *ACS Nano* 10, 573-580 (2015).

[24] J. M. Woods, Y. Jung, Y. Xie, W. Liu, Y. Liu, H. Wang, J. J. Cha. One-step synthesis of MoS_2/WS_2 layered heterostructures and catalytic activity of defective transition metal dichalcogenide films. *ACS Nano* 10, 2004-2009 (2016).

[25] K. Chen, X. Wan, J. Wen, W. Xie, Z. Kang, X. Zeng, H. Chen, J.-B. B. Xu. Electronic properties of MoS_2-WS_2 heterostructures synthesized with two-step lateral epitaxial strategy. *ACS Nano* 9, 9868-9876 (2015).

[26] Y. Yoo, Z. P. Degregorio, J. E. Johns. Seed crystal homogeneity controls lateral and vertical heteroepitaxy of monolayer MoS_2 and WS_2. *Journal of the American Chemical Society* 137, 14281-14287 (2015).

[27] X. Ling, Y. Lin, Q. Ma, Z. Wang, Y. Song, L. Yu, S. Huang, W. Fang, X. Zhang, A. L. Hsu, Y. Bie, Y. H. Lee, Y. Zhu, L. Wu, J. Li, P. Jarillo-Herrero, M. Dresselhaus, T. Palacios, J. Kong. Parallel stitching of 2D materials. *Advanced Materials* 28, 2322-2329 (2016).

[28] S. B. Desai, S. R. Madhvapathy, A. B. Sachid, J. Llinas, Q. Wang, G. Ahn, G. Pitner, M. J. Kim, J. Bokor, C. Hu, H. S. Wong, A. Javey. MoS2 transistors with 1-nanometer gate lengths. *Science* 354, 99-102 (2016).

[29] J. Wang, Q. Yao, C. W. Huang, X. Zou, L. Liao, S. Chen, Z. Fan, K. Zhang, W. Wu, X. Xiao, C. Jiang, W. W. Wu. High mobility MoS_2 transistor with low Schottky barrier contact by using atomic thick h-BN as a tunneling layer. *Advanced Materials* 28, 8302-8308 (2016).

[30] S. Lei, F. Wen, L. Ge, S. Najmaei, A. George, Y. Gong, W. Gao, Z. Jin, B. Li, J. Lou, J. Kono, R. Vajtai, P. Ajayan, N. J. Halas. An atomically layered InSe avalanche photodetector. *Nano Letters* 15, 3048-3055 (2015).

[31] B. Brodie. Xiii. On the atomic weight of graphite. *Philosophical Transactions of the Royal Society of London* 149, 249-259 (1859).

[32] D. R. Dreyer, S. Park, C. W. Bielawski, R. S. Ruoff. The chemistry of graphene oxide. *Chemical Society Reviews* 39, 228-240 (2009).

[33] P. Debye, P. Scherrer. Interferenzen an regellos orientierten teilchen im röntgenlicht. I. *Nachrichten von der Gesellschaft der Wissenschaften zu Göttingen, Mathematisch-Physikalische Klasse* (1916).

[34] J. D. Bernal. The structure of graphite. *Proceedings of the Royal Society of London A: Mathematical, Physical and Engineering Sciences* 106, 749-773 (1924).

[35] P. R. Wallace. The band theory of graphite. *Physical Review* 71, 622-634 (1947).

[36] G. Ruess, F. Vogt. Höchstlamellarer kohlenstoff aus graphitoxyhydroxyd. *Monatshefte für Chemie und verwandte Teile anderer Wissenschaften* 78, 222-242 (1948).

[37] H. P. Boehm, R. Setton, E. Stumpp. Nomenclature and terminology of graphite intercalation compounds. Report by a subgroup of the international committee for characterization and terminology of carbon and graphite on suggestions for rules for the nomenclature and terminology of graphite intercalation compounds. *Synthetic metals* 11, 363-371 (1985).

[38] J. T. Grant, T. W. Haas. A study of Ru(0001) and Rh(111) surfaces using leed and Auger electron spectroscopy. *Surface Science* 21, 76-85 (1970).

[39] J. M. Blakely, J. S. Kim, H. C. Potter. Segregation of carbon to the (100) surface of nickel. *Journal of Applied Physics* 41, 2693-2697 (1970).

[40] R. Rosei, D. M. Crescenzi, F. Sette, Q.-C. B. Structure of graphitic carbon on ni (111): A surface extended-energy-loss fine-structure study. *Physical Review B* (1983).

[41] C. F. McConville, D. P. Woodruff, S. D. Kevan, W.-M. B. Electronic structure of the (2×2) Cρ4g carbidic phase on ni{100}. *Physical Review B* (1986).

[42] T. A. Land, T. Michely, R. J. Behm, J. C. Hemminger, G. Comsa. Stm investigation of single layer graphite structures produced on Pt(111) by hydrocarbon decomposition. *Surface Science* 264, 261-270 (1992).

[43] A. J. Bommel, J. E. Crombeen, V. A. Tooren. Leed and Auger electron observations of the SiC(0001) surface. *Surface Science* 48, 463-472 (1975).

[44] A. Nagashima, K. Nuka, K. Satoh, H. Itoh, T. Ichinokawa, C. Oshima, S. Otani. Electronic structure of monolayer graphite on some transition metal carbide surfaces. *Surface Science* 287, 609-613 (1993).

[45] M. Terai, N. Hasegawa, M. Okusawa, S. Otani, C. Oshima. Electronic states of monolayer micrographite on TiC(111)-faceted and TiC(410) surfaces. *Applied Surface Science* 130, 876-882 (1998).

[46] I. Forbeaux, J. M. Themlin, J. M. Debever. Heteroepitaxial graphite on 6h-SiC(0001): Interface formation through conduction-band electronic structure. *Physical Review B* 58, 16396-16406 (1998).

[47] A. M. Affoune, B. L. V. Prasad, H. Sato, T. Enoki, Y. Kaburagi, Y. Hishiyama. Experimental evidence of a single nano-graphene. *Chemical Physics Letters* 348, 17-20 (2001).

[48] K. Seibert, G. C. Cho, W. Kütt, H. Kurz, D. H. Reitze, J. I. Dadap, H. Ahn, M. C. Downer, A. M. Malvezzi. Femtosecond carrier dynamics in graphite. *Physical Review B* 42, 2842 (1990).

[49] L. Ci, L. Song, C. Jin, D. Jariwala, D. Wu, Y. Li, A. Srivastava, Z. F. Wang, K. Storr, L. Balicas, F. Liu, P. M. Ajayan. Atomic layers of hybridized boron nitride and graphene domains. *Nature Materials* 9, 430-435 (2010).

[50] F. Xia, H. Wang, D. Xiao, M. Dubey, A. Ramasubramaniam. Two-dimensional material nanophotonics. *Nature Photonics* 8, 899-907 (2014).

[51] X. Hong, J. Kim, S.-F. Shi, Y. Zhang, C. Jin, Y. Sun, S. Tongay, J. Wu, Y. Zhang, F. Wang. Ultrafast charge transfer in atomically thin MoS_2/WS_2 heterostructures. *Nature Nanotechnology* 9, 682-686 (2014).

[52] T. Rauch, M. Böberl, S. F. Tedde, J. Fürst, M. V. Kovalenko, G. Hesser, U. Lemmer, W. Heiss, O. Hayden. Near-infrared imaging with quantum-dot-sensitized organic photodiodes. *Nature Photonics* 3, 332-336 (2009).

[53] S. Park, A. Roy, S. Beaupré, S. Cho, N. Coates, J. Moon, D. Moses, M. Leclerc, K. Lee, A. J. Heeger. Bulk heterojunction solar cells with internal quantum efficiency approaching 100%. *Nature Photonics* 3, 297-302 (2009).

[54] X. M. Zhang, M. Y. Lu, Y. Zhang, L. J. Chen, Z. Wang. Fabrication of a high-brightness blue-light-emitting diode using a ZnO-nanowire array grown on p-GaN thin film. *Advanced Materials* 21, 2767-2770 (2009).

[55] The nobel prize in physics 2000, accessed on 17 Sep 2017 from <https://www.nobelprize.org/nobel_prizes/physics/laureates/2000/>.

[56] Y. Liu, N. O. Weiss, X. Duan, H.-C. Cheng, Y. Huang, X. Duan. Van der Waals heterostructures and devices. *Nature Reviews Materials* 1, 16042 (2016).

[57] M.-Y. Li, C.-H. Chen, Y. Shi, L.-J. Li. Heterostructures based on two-dimensional layered materials and their potential applications. *Materials Today* 19, 322-335 (2016).

[58] M. Acerce, D. Voiry, M. Chhowalla. Metallic 1T phase MoS_2 nanosheets as supercapacitor electrode materials. *Nature Nanotechnology* 10, 313-318 (2015).

[59] J. A. Stewart, D. E. Spearot. Atomistic simulations of nanoindentation on the basal plane of crystalline molybdenum disulfide (MoS_2). *Modelling and Simulation in Materials Science and Engineering* 21, 45003 (2013).

[60] R. Ganatra, Q. Zhang. Few-layer MoS_2: A promising layered semiconductor. *ACS Nano* 8, 4074-4099 (2014).

[61] C. Ataca, H. Şahin, S. Ciraci. Stable, single-layer MX_2 transition-metal oxides and dichalcogenides in a honeycomb-like structure. *The Journal of Physical Chemistry C* 116, 8983-8999 (2012).

[62] C. Ataca, M. Topsakal, E. Aktürk, S. Ciraci. A comparative study of lattice dynamics of three- and two-dimensional MoS_2. *The Journal of Physical Chemistry C* 115, 16354-16361 (2011).

[63] S. Bertolazzi, J. Brivio, A. Kis. Stretching and breaking of ultrathin MoS_2. *ACS Nano* 5, 9703-9709 (2011).

[64] A. Castellanos-Gomez, M. Poot, G. A. Steele, H. S. J. van der Zant, N. Agraït, G. Rubio-Bollinger. Elastic properties of freely suspended MoS_2 nanosheets. *Advanced Materials* 24, 772-775 (2012).

[65] J. Pu, Y. Yomogida, K.-K. Liu, L.-J. Li, Y. Iwasa, T. Takenobu. Highly flexible MoS_2 thin-film transistors with ion gel dielectrics. *Nano Letters* 12, 4013-4017 (2012).

[66] R. Toh, Z. Sofer, J. Luxa, D. Sedmidubský, M. Pumera. 3R phase of MoS_2 and WS_2 outperforms the corresponding 2H phase for hydrogen evolution. *Chemical Communications* 53, 3054-3057 (2017).

[67] T. J. Wieting, J. L. Verble. Infrared and raman studies of long-wavelength optical phonons in hexagonal MoS_2. *Physical Review B* (1971).

[68] M. Viršek, A. Jesih, I. Milošević, M. Damnjanović, M. Remškar. Raman scattering of the MoS_2 and WS_2 single nanotubes. *Surface Science* 601, 2868-2872 (2007).

[69] C. V. Ramana, U. Becker, V. Shutthanandan, C. M. Julien. Oxidation and metal-insertion in molybdenite surfaces: Evaluation of charge-transfer mechanisms and dynamics. *Geochemical transactions* 9, 8 (2008).

[70] P. A. Bertrand. Surface-phonon dispersion of MoS_2. *Physical Review B* 44 (1991).

[71] C. Lee, H. Yan, L. E. Brus, T. F. Heinz, J. Hone, S. Ryu. Anomalous lattice vibrations of single- and few-layer MoS_2. *ACS Nano* 4, 2695-2700 (2010).

[72] B. Chakraborty, R. H. S. S. Matte, A. K. Sood, C. N. R. Rao. Layer-dependent resonant raman scattering of a few layer MoS_2. *Journal of Raman Spectroscopy* 44, 92-96 (2013).

[73] H. Li, Q. Zhang, C. Yap, B. Tay, T. Edwin, A. Olivier, D. Baillargeat. From bulk to monolayer MoS_2: Evolution of raman scattering. *Advanced Functional Materials* 22, 1385-1390 (2012).

[74] X. Zhang, X.-F. Qiao, W. Shi, J.-B. Wu, D.-S. Jiang, P.-H. Tan. Phonon and raman scattering of two-dimensional transition metal dichalcogenides from monolayer, multilayer to bulk material. *Chemical Society Reviews* 44, 2757-2785 (2015).

[75] A. Splendiani, L. Sun, Y. Zhang, T. Li, J. Kim, C.-Y. Y. Chim, G. Galli, F. Wang. Emerging photoluminescence in monolayer MoS_2. *Nano Letters* 10, 1271-1275 (2010).

[76] H. Zeng, G.-B. Liu, J. Dai, Y. Yan, B. Zhu, R. He, L. Xie, S. Xu, X. Chen, W. Yao, X. Cui. Optical signature of symmetry variations and spin-valley coupling in atomically thin tungsten dichalcogenides. *Scientific Reports* 3, 1608 (2013).

[77] H.-P. Komsa, A. V. Krasheninnikov. Effects of confinement and environment on the electronic structure and exciton binding energy of MoS_2 from first principles. *Physical Review B* 86 (2012).

[78] E. S. Kadantsev, P. Hawrylak. Electronic structure of a single MoS_2 monolayer. *Solid State Communications* 152, 909-913 (2012).

[79] M. Buscema, G. A. Steele, H. S. J. van der Zant, A. Castellanos-Gomez. The effect of the substrate on the raman and photoluminescence emission of single-layer MoS_2. *Nano Research* 7, 561-571 (2014).

[80] K. Mak, K. He, C. Lee, G. Lee, J. Hone, T. F. Heinz, J. Shan. Tightly bound trions in monolayer MoS_2. *Nature Materials* 12, 207-211 (2012).

2. Preliminary experiments of 2D materials: Graphene

2.1. Introduction

Graphene is a 2D single-layered sheet of sp^2-bonded carbon atoms in a honeycomb structure, resembling hexagons with a lattice constant of 0.25 nm (Figure 2-1a). Every single carbon atom is connected to the three nearest atoms via σ-bonds, while one π-bond is perpendicular to three σ-bonds and forms a side-by-side overlap with another π-bond of the nearest atom, as opposed to the end-to-end overlap of the σ-bonds (Figure 2-1b). This π-bond is not free to rotate, which makes the structure of graphene flat and planar. Graphite, a three-dimensional (3D) form of carbon atoms, consists of stacks of individual graphene layers bonded together with weak van der Waals forces.

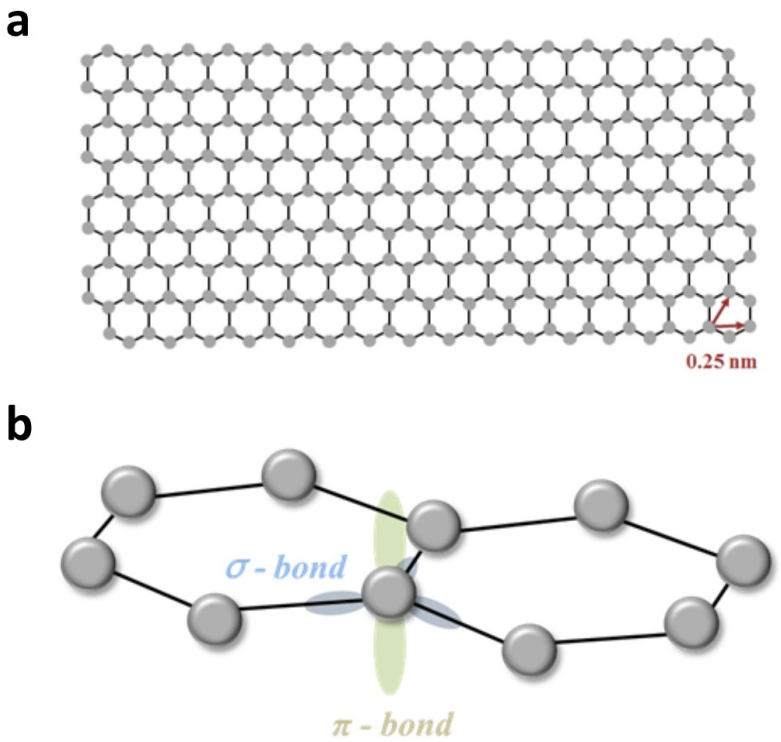

Figure 2-1. Crystal structures of graphene. a) Atomic structure of graphene and b) the carbon bonding of graphene.

As already stated, graphene has attracted considerable attention[1] because of its unique physical properties including extremely high electrical conductivity, good thermal stability, and a mechanical strength greater than that of steel.[2],[3] All of these properties are remarkably different to the bulk properties of graphite. Above all, graphene is a transparent[4] and flexible[5] material, which is suitable for modern electronic devices such as transparent displays. These properties make it interesting with regards to fundamental research and future device applications. In addition to its inherent properties, the dimensionality of graphene has been one of its most attractive material parameters since its discovery.

Simple substances and chemical compounds usually have a 3D crystal structure and their basic properties do not generally depend on the shape and size of these structures. However, this is not the case when the dimensionality of the material decreases to 2D, 1D, and 0D, as demonstrated with carbon-based materials. Graphite has been widely known since the sixteenth century, and used in various industrial sectors for refractories, battery electrodes, lubricant, and pencils. However, it was not until 1985 that fullerene and a 0D-type of graphite were discovered.[6] Subsequently, the first demonstration of a carbon nanotube was conducted in 1991.[7] Even though graphene is the basic building block for these carbon nanostructures and has a unique zero band gap, graphite behaves like a metal whereas diamond, an allotrope of carbon, behaves as an insulator.[8] In the case of carbon nanotubes, it is known that the rolling angle and radius determine whether the nanotube acts as a metallic or semiconducting material. Therefore, dimensionality is one of the most defining parameters when determining the resultant material properties.

In this chapter, the characteristics of graphene will be examined and the process of growing graphene using chemical vapour deposition (CVD) will be explained. CVD synthesis

is selected because it can produce large-sized and highly-crystalline graphene film. In addition, the functionality of simple electronic devices based on graphene will be demonstrated.

2.2. Synthesis of graphene

Since the first discovery of graphene, a mechanical exfoliation method has been widely used to produce various 2D materials, because of its reliability and convenience for synthesis. Until recently, the best quality 2D materials were synthesized using this method. However, the dimensions of the crystals that can be obtained using this method is limited to only a few tens of micrometres. A further problem is that the number of exfoliated layers cannot be controlled precisely. For large-scale growth of graphene or 2D material films with low structural defects, another method is therefore required.

Even though the method of depositing graphite by heterogeneous catalysis on transition metals has been known for some time, the first report on the CVD synthesis of a few layers of graphene (with camphor ($C_{10}H_{16}O$) as a carbon precursor and Ni sheets as substrates) was only published in 2006[19]. Genuine single-layer graphene produced using a CVD method was reported in 2009, using Ni and Cu sheets as the substrates.[20], [21] Since then, the CVD method has been examined for other transition metals such as Ru,[22] Ir,[23] Pt,[24] Co,[25] Pd[26] and Re,[27] and it has been shown that the growth quality is strongly related to the metal catalysts used. In this work, the synthesis is conducted on Cu foils, mainly because the lower activity and lower carbon solubility of Cu, compared to Ni and other metals, make it easier to synthesize large-scale single-layer graphene.[20]

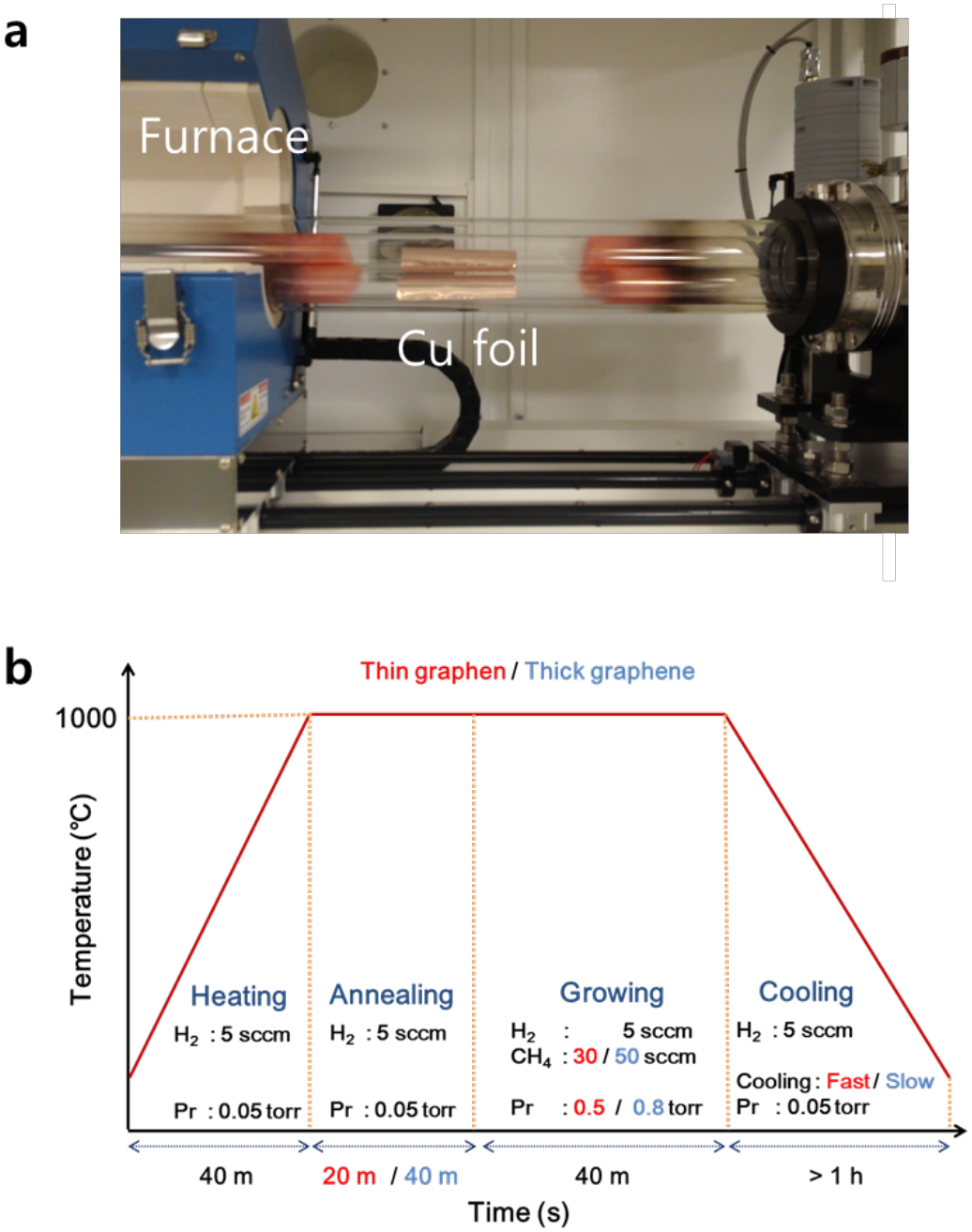

Figure 2-2. CVD growth process for graphene. a) A photograph of the CVD machine used to grow graphene (The inner tubes were intentionally taken out from the furnace in order to clearly show the Cu foil in the inner tubes). b) The growth recipe for thin- and thick-layered graphene. The growth conditions for thin and thick graphene are coloured in red and blue, respectively.

The graphene film was synthesized on 250-μm thick Cu foil in the CVD machine with a method similar to that reported in previous studies[20], [21] (Figure 2-2). The synthesis process can be divided into six separate steps: (1) substrate cleansing, (2) heating, (3) annealing, (4) growth, (5) cooling, and (6) opening. Before inserting the Cu foil into the hot-wall furnace, it was first cleaned to form a good quality graphene film on the surface without defects. The foil was dipped into a 1M HCl solution (36% HCl: 16.4 ml and deionized water: 200 ml), followed by a general substrate cleansing process (acetone, ethanol, and deionized water). Then, a 50-mm inner tubular quartz tube containing a sheet of Cu foil was inserted into a 100-mm outer tube, which was then heated to 1000°C at a rate of ~25°C per minute under vacuum conditions (0.05 torr) under a H_2 flow (5 sccm). To stabilize the growth temperature at 1000°C, the tube was annealed for 20 min. During the CVD synthesis period, the Cu foil was exposed to CH_4/H_2 (30 and 5 sccm) gas mixture. In the meantime, the pressure in the tube was maintained at 0.5 torr.

Growth kinetics and reaction mechanisms can be explained more in detail as follows.[28-30] During the annealing step, the surface of the Cu foil is reduced by H_2 molecules. As a result, the bare metal surface is exposed to H_2 molecules before the flow of the CH_4 gas. Strong C–H bonds in the methane molecules usually make it difficult for molecular decomposition to occur at temperatures under 1200 °C without catalysts. However, transition metal catalysts such as Cu and Ni can reduce the temperature of the decomposition of CH_4 at low temperatures (< 900 °C). Therefore, when a mixture of H_2/CH_4 was introduced into the system to initiate the graphene growth, the Cu foil used in the synthesis process plays a role not only as a substrate but also as a catalyst, and contributes to the decomposition of CH_4 into CH_x on the Cu substrate at 1000 °C. It is known that the dissolute carbon atoms diffuse into the bulk metal when Ni foils are used as a catalyst in the synthesis process. In contrast, Cu has an ultralow carbon solubility and only a very small amount of carbon can dissolve into the Cu foil when the growth

time and the flow rate of CH_4 are properly controlled. Therefore, the growth of graphene on the Cu foil is considered to be due to a surface reaction process or surface migration process. The surface migration continues until the concentration of carbon in the bulk metal reaches equilibrium. After the monolayer growth, the Cu foil is fully covered with carbon structures and no catalyst is exposed to CH_4 to promote the decomposition and the growth process, which decreases the catalytic activity. Finally, this can finish the reaction and the monolayer growth and is known as a self-limiting effect and has been observed in the CVD process when Cu foils are used as a substrate. For these reasons, Cu foils are used as a catalyst and a substrate for the growth of graphene in this chapter.

During the cooling stage, the temperature of the sample was rapidly decreased to room temperature by moving the furnace outwards and exposing the tube to the current of an electric fan with a H_2 flow (5 sccm). This rapid cooling rate is critical for the formation of a single-layer graphene film.[21], [31] During the cooling process, a small amount of carbon atoms can diffuse from the Cu-C solid solution and form additional graphene films on the surface of the Cu foil, so the number of graphene layers can be controlled by changing the cooling rate, as will be explained below. Finally, the furnace chamber was opened after backfilling the tube with argon gas up to atmospheric pressure.

To control the number of layers of graphene grown on the substrate, some modifications to the growth process were made. Graphene films with more than two layers can be grown by increasing the annealing time and the flow of methane gas during the growth period. As the growth time increases, more carbon atoms can diffuse into the Cu foil.[32] Similarly, the methane gas flow rate in the growth process was increased to 50 sccm to supply more carbon atoms. As the carbon atoms that are diffused into the foil can emerge on the foil surface during the slow cooling period before they are fixed inside the Cu foil, multilayered graphene was grown on the foil.

2.3. Transfer of graphene film

For device applications it is important to transfer the graphene film grown on the surface of the Cu foil to a target substrate. The transfer process[21] used in this chapter is summarized in Figure 2-3. The Cu foil containing the graphene film was placed on a PET film and the edge of the film was attached with tape in order to hold the foil firmly in position. The PET film helps prevent the Cu foil from folding during the subsequent spin-coating process. A Poly(methyl methacrylate) (PMMA) solution was dropped onto the surface of the graphene-grown Cu foil to produce a polymer support, followed by spin-coating of the solution at a rate of 500 rpm for 10 s, 3500 rpm for 30 s, and 500 rpm for 10 s. Following this, the foil was then baked on a hot-plate at 70°C for 3 minutes and then at 120°C for more than 4 minutes after the removal of the tape, in order to strengthen the bond between the PMMA and the graphene film. As copper can be etched using a strong oxidizing agent, 0.1M ammonium persulfate ($(NH_4)_2S_2O_8$) (4.564 g with 200 ml deionized water) was used as an etchant to remove the copper layers. The graphene-grown copper foil was floated on the Cu etchant for more than 12 hours, and the net ionic equation of the etching reaction can be represented as follows:

$$(NH_4)_2S_2O_8\ (aq) + Cu\ (s) \rightarrow (NH_4)_2SO_4\ (aq) + CuSO_4\ (aq). \qquad (2.1)$$

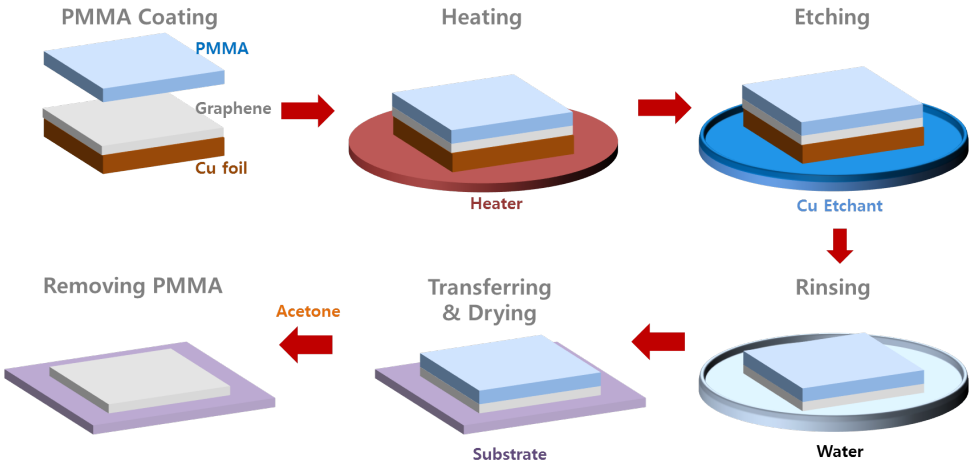

Figure 2-3. Transfer process for CVD-grown graphene films.

This reaction etches away the copper layers slowly without damaging the graphene film because no gas or precipitates are produced during the process. To obtain a high quality single-layer graphene film, one additional process is needed. The graphene film was grown on both sides of the Cu foil during the CVD growth process, so it was necessary to remove the graphene film on the redundant back side of the foil, which made contact with the Cu etchant. The graphene film is not easily damaged by the Cu etchant, so the back side should be removed by plasma cleaning machines or manually. In this work, the manual removal process with wipes was conducted 30 minutes after the Cu film was floated on the etchant. It is important to conduct this process before the graphene film on the back side of the Cu foil meets the graphene film on the front side directly. After this process, the Cu film was again placed on the etchant. When the copper film was completely etched away from the PMMA/graphene film, only a transparent film remained on the etchant, and the colour of the etchant changed from transparent to cyan. To remove any etchant residue, the transparent film was transferred to deionized water, using a slide glass as a transferring tool, and floated there for 15 minutes. The deionized water cleaning processes were repeated three times.

It is worth noting that the PMMA/graphene film can be transferred onto arbitrary substrates such as slide glass and Si/SiO_2 substrates. After transfer onto a targeting substrate, the substrate was dried on a hot-plate at 90-100°C for 1 hour. After complete evaporation of the water vapour had occurred, the PMMA film, which had supported the graphene film, was removed by slowly dipping the substrate into an acetone solution without damaging the graphene film. This removal process was conducted very carefully, because rapidly dipping the substrate into acetone could simultaneously remove the graphene film as well as the PMMA layers. The thin and thick graphene films transferred on the glass substrates can be seen in Figure 2-4a.

2.4. Characterization of graphene

The thickness of graphene is known to be ~0.4 nm and AFM is one of the most powerful tools for measuring the layer thickness of graphene because the detection limit of a typical AFM is ~0.1 nm. However, it is not easy to measure the precise thickness of graphene using AFM because of the interaction between the AFM tip and the graphene film or the underlying substrate. Previous studies using AFM have resulted in graphene thickness data in the range of 0.4-1.0 nm.[33-34] The thicknesses of thin graphene films measured in this work were also smaller than 1.0 nm (Figure 2-4b).

In addition, Raman spectroscopy was used as a tool to identify the number of graphene layers on the substrate. The Raman spectrum was first used for graphite analysis 40 years ago.[35] Since then, Raman spectroscopy has played an important role in the study of carbon-based materials such as graphite, fullerenes, and carbon nanotubes,[36] and a report on Raman spectrum of graphene was first published in 2006.[37] Raman spectroscopy has also become one of the most popular tools to confirm the numbers of layers of graphene films.

Before Raman spectroscopy was conducted, the graphene films were transferred onto a Si/SiO_2 (300 nm) substrate. The Raman spectra were measured with a Horiba Jobin Yvon LabRam Aramis Microscope with a 532-nm green laser as an excitation source. Figure 2-4c shows the Raman spectra of the graphene grown in this work. The major Raman peaks of carbon-related materials are called the G band (~1580 cm^{-1}), 2D band (~2670 cm^{-1}), and D band (~1350 cm^{-1}). The G band is known to be related to the in-plane vibration of sp^2 carbon bonding, and its absolute intensity tends to increase as the number of graphene layers increases. The 2D peak originates from a two phonon double resonance Raman process, and is related to out-plane vibrations.[36], [38], [39] The G band and 2D band do not require a defect for their activation, so they are always present in the Raman spectra of graphite-related materials.[37]

The most striking feature with the increase in the number of graphene layers is the ratio of the G band to the 2D band. The Raman spectra of single-layer graphene has a 2D peak whose intensity is about 2 times greater than that of the G peak. However, in the spectra of bilayer graphene, the intensities of the G peak and the 2D peak become almost the same.

In graphene films of more than 3 layers, the G band becomes more dominant than the 2D band.[40] This trend was also found in the Raman spectra measured in this work. The Raman spectrum of the thin graphene film was confirmed to be single layer because the 2D band peak was twice as large as the G band peak. The thick graphene film was found to have about 3 layers because its Raman spectrum showed a similar trend to the spectrum of 3-layered graphene. In addition, in Figure 2-4d, the transmittance of the thin graphene film (~97%) also indicated that it was a monolayer.[41]

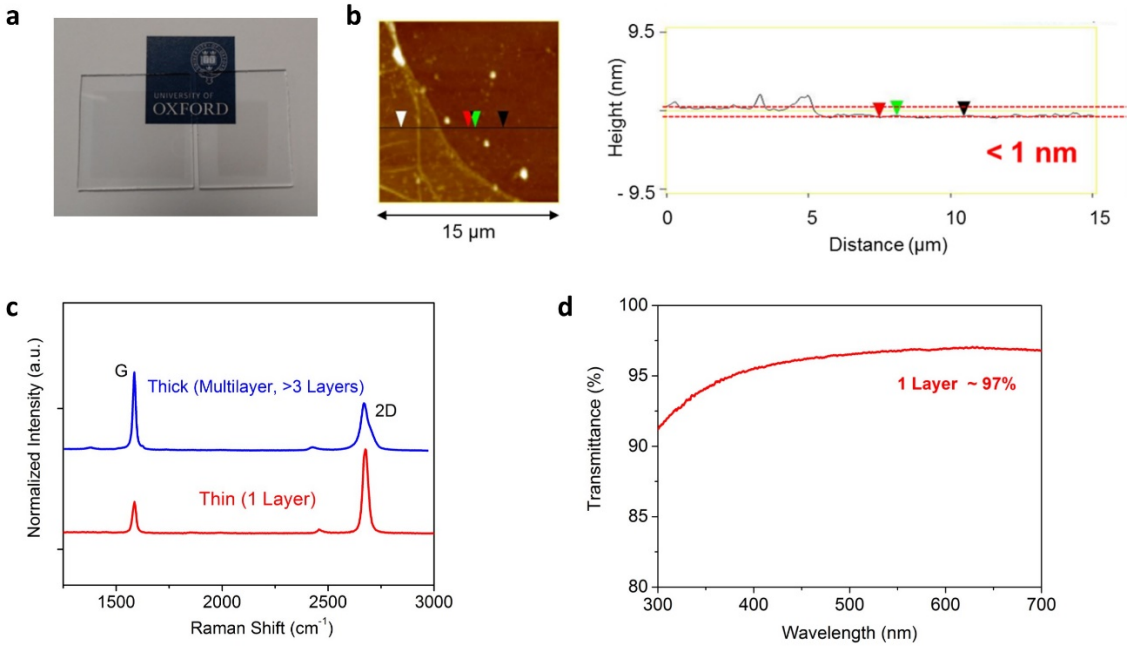

Figure 2-4. Characterisation of a graphene film. a) Thin (left) and thick (right) graphene films on glass slides. b) AFM image of the thin graphene film. The different coloured arrows in the right panel represent the positions marked by the corresponding coloured arrows, respectively. c) Raman spectra for thin (red) and thick (blue) graphene films and d) Transmittance of graphene for white light.

2.5. Application of graphene: triboelectric generators

To determine the quality of graphene as an electrode, a graphene-based triboelectric nanogenerator was fabricated using thick (few-layer) graphene films grown by CVD on a Cu foil. Biomechanical energy harvesting from human motion is emerging as one of the most attractive research fields in this area because the need for charging portable electronic devices has increased dramatically. If batteries can be charged by human motion, people will be free from the effort of looking for electrical sockets to charge their various devices. In this respect, many studies on biomechanical energy harvesting using piezoelectricity and triboelectricity have been conducted to address this challenge.[42-50] This energy harvesting process uses human-driven forces as energy sources by attaching energy harvesting devices to the human body. Recently, a triboelectric generator using the human body itself as a power-generating material was developed; this device is designed so that human touch can generate energy.[51] Triboelectric generators usually require two metal electrodes deposited on triboelectric materials to produce electricity, which makes it difficult for human skin to touch the materials directly. To solve this problem a single-electrode generator was introduced using polydimethylsiloxane (PDMS) as the triboelectric material and ITO as the electrode. This generator was found to produce an open-circuit voltage up to 1000 V, a short-circuit current density of 8 mA m^{-2}, and a power density of 500 mW m^{-2}.[51]

In this work, a similar triboelectric generator was fabricated using graphene as an electrode instead of ITO (Figure 2-5a). A PDMS block grown on a petri dish was placed on the graphene film. A load resistance of 1 MΩ was connected using silver paint and the end of the load was grounded. According to the triboelectric series,[52-53] the periodic change in distance between the human skin and the PDMS film induces charge transfer, thus causing electrons to flow across the external load.

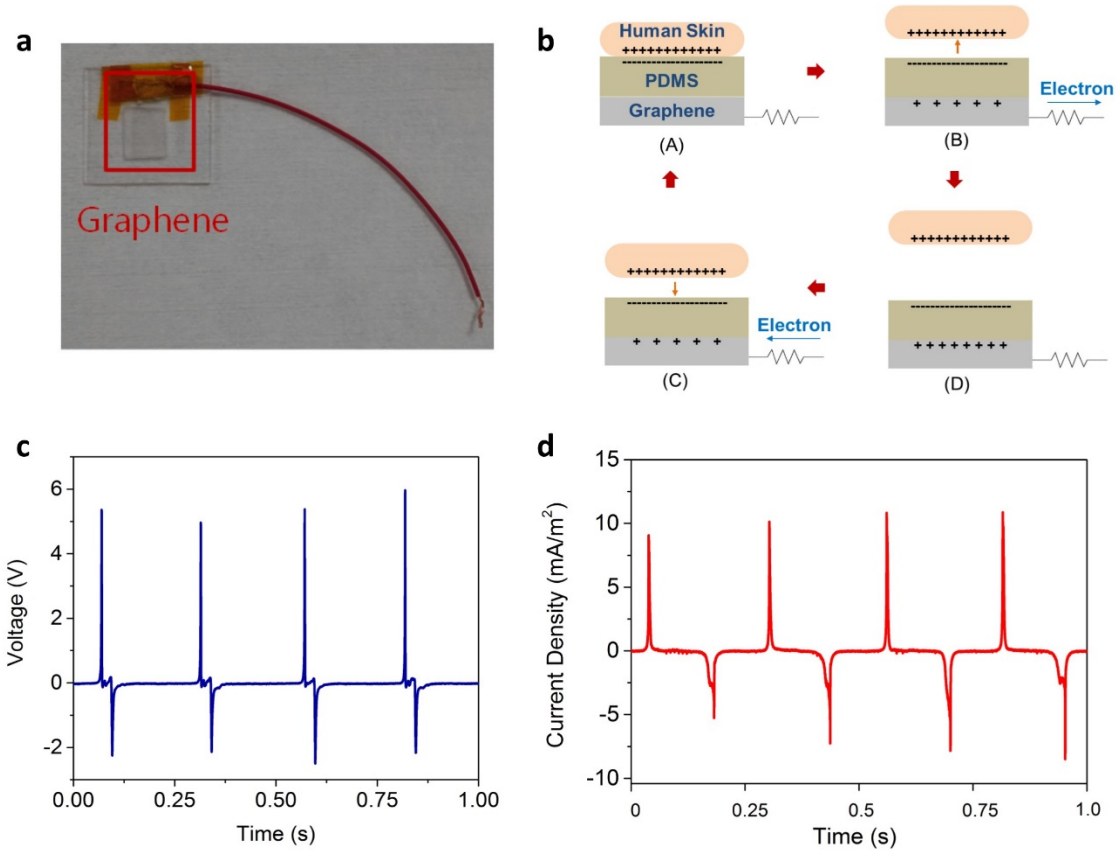

Figure 2-5. Graphene triboelectric generators. a) Photograph of a graphene-based triboelectric generator. b) Illustration of the operating principle. c) Time resolved open-circuit voltage and d) short-circuit current density.

The basic working principle of the single-electrode triboelectric generator is described in Figure 2-5b.[51] If the human skin and PDMS film make contact with each other, positive charge on the skin and negative charge on the PDMS are induced, because PDMS is more triboelectrically negative than human skin according to the triboelectric series[54] (Figure 2-5b (A)). However, once the human skin is detached from the PDMS film, the balance in the charge between the skin and the PDMS film will be broken, which leads to positive charge induction on the graphene electrode from the ground due to the negative charge on the PDMS film (Figure 2-5b (B)). This induction causes an output voltage and current in the generator. This output signal will vanish if the skin becomes sufficiently distant from the PDMS film and, thus, the

negative charge on the PDMS film is completely balanced by the positive charge from the ground (Figure 2-5b (C)). As the skin approaches the PDMS films again, this causes positive charge on the graphene electrode to decrease and electrons flow from the ground to the graphene electrode, resulting in a reverse output voltage and current signal (Figure 2-5b (D)). These steps will be repeated continuously in response to periodic contact. Figures 2-5c and 2-5d show the measured open-circuit voltages and short-circuit current density of the triboelectric generator, respectively. The pressure from the human skin was maintained at 0.1 kgf cm^{-2} with a contact frequency of 4 Hz. Positive voltages and currents are generated by contact, and negative voltages and currents are due to detachment. The device produced a peak output voltage of 5 V with a peak current density of 9 mA m^{-2}, resulting in an instantaneous power density of 45 mW m^{-2}. This result shows the potential of graphene as a large-area electrode and is a significant step toward the practical application of skin-based biomechanical energy harvesting technology.

2.6. Conclusions

In this work, a CVD synthesis process has been successfully employed to synthesize graphene films on Si/SiO_2 substrates, using Cu foils as substrates and catalysts. Even though high-quality graphene flakes can be obtained through mechanical cleavage, CVD synthesis has been selected for the fabrication process in this work because it can produce large-area graphene films, which are suitable for fabricating electronic devices. Cu has a relatively low carbon solubility at a high temperature, compared to other transition metals. This means that the growth of graphene using Cu foils is due to a surface reaction process, which makes it easier to produce one-layer-thick graphene films on the substrates. The synthesized film has been found to be a monolayer from measurements of the optical contrast, Raman spectra, and AFM

analysis. It was also confirmed that the number of graphene layers could be controlled by adjusting the annealing time and the H_2 and CH_4 flow rates. In addition, it was revealed that graphene could be used as an electrode in a triboelectric generator. The 2D electrode and semiconducting materials are expected to provide a new avenue for the development of electronic devices because of their mechanical stability, flexibility, and transparency. Therefore, it would be intriguing and worthwhile to further investigate these 2D monolayers as post-silicon materials.

2.7. References

[1] K. S. Novoselov, A. K. Geim, S. V. Morozov, D. Jiang, Y. Zhang, S. V. Dubonos, I. V. Grigorieva, and A. A. Firsov. Electric field effect in atomically thin carbon films. *Science* 306, 666-669 (2004).

[2] A. K. Geim and K. S. Novoselov. The rise of graphene. *Nature Materials* 6, 183–191 (2007).

[3] E. Castro, H. Ochoa, M. Katsnelson, R. Gorbachev, D. Elias, K. Novoselov, A. Geim, and F. Guinea. Limits on charge carrier mobility in suspended graphene due to flexural phonons. *Physical Review Letters* 105, 266601 (2010).

[4] D. Hecht, L. Hu, and G. Irvin. Emerging transparent electrodes based on thin films of carbon nanotubes, graphene, and metallic nanostructures. *Advanced Materials* 23, 1482-1513 (2011).

[5] S.-K. Lee, B. Kim, H. Jang, S. Yoon, C. Lee, B. Hong, J. Rogers, J. Cho, and J.-H. Ahn, Stretchable graphene transistors with printed dielectrics and gate electrodes. *Nano Letters* 11, 4642–4646 (2011).

[6] H. Kroto, J. Heath, S. O'Brien, R. Curl, and R. Smalley. C60: Buckminsterfullerene. *Nature* 318, 162-163 (1985).

[7] S. Iijima. Helical microtubules of graphitic carbon. *Nature* 354, 56-58 (1991).

[8] K. S. Novoselov, A. K. Geim, S. V. Morozov, D. Jiang, M. I. Katsnelson, I. V. Grigorieva, S. V. Dubonos, and A. A. Firsov. Two-dimensional gas of massless Dirac fermions in graphene. *Nature* 438, 197–200 (2005).

[9] L. Mattheiss. Band structures of transition-metal-dichalcogenide layer compounds. *Physical Review B* 8, 3719-3740 (1973).

[10] J. A. Wilson and A. D. Yoffe. The transition metal dichalcogenides discussion and interpretation of the observed optical, electrical and structural properties. *Advances in Physics* 18, 193-335 (1969).

[11] M. Osada and T. Sasaki. Two-dimensional dielectric nanosheets: Novel nanoelectronics from nanocrystal building blocks. *Advanced Materials* 24, 210-228 (2012).

[12] A. Ayari, E. Cobas, O. Ogundadegbe, and M. Fuhrer. Realization and electrical characterization of ultrathin crystals of layered transition-metal dichalcogenides. *Journal of Applied Physics* 101, 014507 (2007).

[13] C. Dean, A. Young, I. Meric, C. Lee, L. Wang, S. Sorgenfrei, K. Watanabe, T. Taniguchi, P. Kim, K. Shepard, and J. Hone. Boron nitride substrates for high-quality graphene electronics. *Nature Nanotechnology* 5, 722-726 (2010).

[14] D. Pacile, J.C. Meyer, C.O. Girit, and A. Zettl. The two-dimensional phase of boron nitride: Few-atomic-layer sheets and suspended membranes. *Applied Physics Letters* 92, 133107 (2008).

[15] K. F. Mak, C. Lee, J. Hone, J. Shan, and T. F. Heinz. Atomically thin MoS_2: A new direct-gap semiconductor. *Physical Review Letters* 105, 136805 (2010).

[16] A. Yoffe. Layer Compounds. *Annual Review of Materials Science* 3, 147-170 (1973).

[17] A. D. Yoffe. Low-dimensional systems: Quantum size effects and electronic properties of semiconductor microcrystallites (zero-dimensional systems) and some quasi-two-dimensional systems. *Advances in Physics* 42, 799-890 (1993).

[18] B. Radisavljevic, A. Radenovic, J. Brivio, V. Giacometti, and A. Kis. Single-layer MoS_2 transistors. *Nature Nanotechnology* 6, 147-150 (2011).

[19] P. Somani, S. Somani, and M. Umeno. Planer nano-graphenes from camphor by CVD. *Chemical Physics Letters* 430, 56-59 (2006).

[20] X. Li, W. Cai, J. An, S. Kim, J. Nah, D. Yang, R. Piner, A. Velamakanni, I. Jung, E. Tutuc, S. K. Banerjee, L. Colombo, and R. S. Ruoff. Large-area synthesis of high-quality and uniform graphene films on copper foils. *Science* 324, 1312-1314 (2009).

[21] K. S. Kim, Y. Zhao, H. Jang, S. Y. Lee, J. M. Kim, K. S. Kim, J.-H. H. Ahn, P. Kim, J.-Y. Y. Choi, and B. H. Hong. Large-scale pattern growth of graphene films for stretchable transparent electrodes. *Nature* 457, 706-710 (2009).

[22] P. Sutter, J.-I. Flege, and E. Sutter. Epitaxial graphene on ruthenium. *Nature Materials* 7, 406-411 (2008).

[23] E. Loginova, N. Bartelt, P. Feibelman, and K. McCarty. Factors influencing graphene growth on metal surfaces. *New Journal of Physics* 11, 063046 (2009).

[24] L. Gao, W. Ren, H. Xu, L. Jin, Z. Wang, T. Ma, L.-P. Ma, Z. Zhang, Q. Fu, L.-M. Peng, X. Bao, and H.-M. Cheng. Repeated growth and bubbling transfer of graphene with

millimetre-size single-crystal grains using platinum. *Nature Communications* 3, 699 (2012).

[25] H. Ago, Y. Ito, N. Mizuta, K. Yoshida, B. Hu, C. Orofeo, M. Tsuji, K. Ikeda, and S. Mizuno. Epitaxial chemical vapor deposition growth of single-layer graphene over cobalt film crystallized on sapphire. *ACS Nano* 4, 7407-7414 (2010).

[26] S.-Y. Kwon, C. Ciobanu, V. Petrova, V. Shenoy, J. Bareño, V. Gambin, I. Petrov, and S. Kodambaka. Growth of semiconducting graphene on palladium. *Nano Letters* 9, 3985–3990 (2009).

[27] C. Tonnoir, A. Kimouche, J. Coraux, L. Magaud, B. Delsol, B. Gilles, and C. Chapelier. Induced superconductivity in graphene grown on rhenium. *Physical Review Letters* 111, 246805 (2013).

[28] M. Losurdo, M. Giangregorio, P. Capezzuto & G. Bruno. Graphene CVD growth on copper and nickel: Role of hydrogen in kinetics and structure. *Physical Chemistry Chemical Physics* 13, 20836-20843 (2011).

[29] Y. Zhang, L. Zhang & C. Zhou. Review of chemical vapor deposition of graphene and related applications. *Accounts of Chemical Research* 46, 2329-2339 (2013).

[30] R. Muñoz & C. Gómez-Aleixandre. Review of CVD synthesis of graphene. *Chemical Vapor Deposition* 19, 297-322 (2013).

[31] A. Reina, X. Jia, J. Ho, D. Nezich, H. Son, V. Bulovic, M. S. Dresselhaus, and J. Kong. Large area, few-layer graphene films on arbitrary substrates by chemical vapor deposition. *Nano Letters* 9, 30-35 (2009).

[32] Z. Robinson, P. Tyagi, T. Murray, C. Ventrice, S. Chen, A. Munson, C. Magnuson, and R. Ruoff. Substrate grain size and orientation of Cu and Cu-Ni foils used for the growth of graphene films. *Journal of Vacuum Science & Technology A: Vacuum, Surfaces, and Films* 30, 011401 (2012).

[33] M. Connolly and C. Smith. Nanoanalysis of graphene layers using scanning probe techniques. *Philosophical Transactions of the Royal Society A: Mathematical, Physical and Engineering Sciences* 368, 5379-5389 (2010).

[34] A. Deshpande and B. LeRoy. Scanning probe microscopy of graphene. *Physica E: Low-dimensional Systems and Nanostructures* 44, 743-759 (2012).

[35] F. Tuinstra. Raman spectrum of graphite. *The Journal of Chemical Physics* 53, 1126 (1970).

[36] M. S. Dresselhaus, G Dresselhaus, R Saito, and A. Jorio. Raman spectroscopy of carbon nanotubes. *Physics Reports* 409, 47-99 (2005).

[37] A. C. Ferrari, J. C. Meyer, V. Scardaci, C. Casiraghi, M. Lazzeri, F. Mauri, S. Piscanec, D. Jiang, K. S. Novoselov, S. Roth, and A. K. Geim. Raman spectrum of graphene and graphene layers. *Physical Review Letters* 97, 187401 (2006).

[38] S. Reich and C. Thomsen. Raman spectroscopy of graphite. *Philosophical Transactions of the Royal Society A* 362, 2271-2288 (2004).

[39] M. Dresselhaus, G. Dresselhaus, R. Saito, and A. Jorio. Raman spectroscopy of carbon nanotubes. *Physics Reports* 409, 47-99 (2005).

[40] A. Ferrari and D. Basko. Raman spectroscopy as a versatile tool for studying the properties of graphene. *Nature Nanotechnology* 8, 235–246 (2013).

[41] R. R. Nair, P. Blake, A. N. Grigorenko, K. S. Novoselov, T. J. Booth, T. Stauber, N. M. Peres, and A. K. Geim. Fine structure constant defines visual transparency of graphene. Science 320, 1308 (2008).

[42] G. Zhu, C. Pan, W. Guo, C.-Y. Y. Chen, Y. Zhou, R. Yu, and Z. L. Wang. Triboelectric-generator-driven pulse electrodeposition for micropatterning. *Nano Letters* 12, 4960-4965 (2012).

[43] G. Zhu, Z.-H. H. Lin, Q. Jing, P. Bai, C. Pan, Y. Yang, Y. Zhou, and Z. L. Wang. Toward large-scale energy harvesting by a nanoparticle-enhanced triboelectric nanogenerator. *Nano Letters* 13, 847-853 (2013).

[44] J. Zhong, Q. Zhong, F. Fan, Y. Zhang, S. Wang, B. Hu, Z. Wang, and J. Zhou. Finger typing driven triboelectric nanogenerator and its use for instantaneously lighting up LEDs. *Nano Energy* 2, 491-497 (2013).

[45] S. Wang, L. Lin, and Z. L. Wang. Nanoscale triboelectric-effect-enabled energy conversion for sustainably powering portable electronics. *Nano Letters* 12, 6339-6346 (2012).

[46] S. Wang, L. Lin, Y. Xie, Q. Jing, S. Niu, and Z. L. Wang. Sliding-triboelectric nanogenerators based on in-plane charge-separation mechanism. *Nano Letters* 13, 2226-2233 (2013).

[47] G. Zhu, J. Chen, Y. Liu, P. Bai, Y. S. Zhou, Q. Jing, C. Pan, and Z. L. Wang. Linear-grating triboelectric generator based on sliding electrification. *Nano Letters* 13, 2282-2289 (2013).

[48] L. Lin, S. Wang, Y. Xie, Q. Jing, S. Niu, Y. Hu, and Z. L. Wang. Segmentally structured disk triboelectric nanogenerator for harvesting rotational mechanical energy. *Nano Letters* 13, 2916-2923 (2013).

[49] P. Bai, G. Zhu, Y. Liu, J. Chen, Q. Jing, W. Yang, J. Ma, G. Zhang, and Z. Wang. Cylindrical rotating triboelectric nanogenerator. *ACS Nano* 7, 6361-6366 (2013).

[50] Y. Yang, H. Zhang, J. Chen, Q. Jing, Y. S. Zhou, X. Wen, and Z. L. Wang. Single-electrode-based sliding triboelectric nanogenerator for self-powered displacement vector sensor system. *ACS Nano* 7, 7342-7351 (2013).

[51] Y. Yang, H. Zhang, Z.-H. Lin, Y. Zhou, Q. Jing, Y. Su, J. Yang, J. Chen, C. Hu, and Z. Wang. Human skin based triboelectric nanogenerators for harvesting biomechanical energy and as self-powered active tactile sensor system. *ACS Nano* 7, 9213-9222 (2013).

[52] J. F. Hughes. Electrostatics: Principles, problems and applications. *J A Cross* (1987).

[53] A. F. Diaz and R. M. Felix-Navarro. A semi-quantitative tribo-electric series for polymeric materials: the influence of chemical structure and properties. *Journal of Electrostatics* 62, 277-290 (2004).

[54] V. E. Shashoua. Static electricity in polymers. I. Theory and measurement. *Journal of Polymer Science* 33, 65-85 (1958).

3. Synthesis of TMDC monolayers and their use in vertical heterostructure devices

3.1. Introduction

As already discussed, atomically thin transition metal dichalcogenides (TMDCs) have great potential in a range of nanoelectronic devices such as transistors,[1-4] photodetectors,[5-8] and memory elements.[9-12] It is known that the electrical and optical properties of TMDC devices are influenced by the number of layers and the grain boundaries.[13-16] Accordingly, numerous studies have focused on developing scalable synthetic schemes for the production of TMDC monolayer films with large-sized crystals, using a variety of growth techniques such as thermolysis,[17-19] pulsed laser deposition,[20-22] the sulfurization of metal or metal oxide films,[23-25] and chemical vapor deposition (CVD).[16,26-28] Among these methods, CVD has been shown to be the most practical method for synthesizing highly-crystalline TMDC monolayers, exhibiting relatively good optical and electrical properties.[16,29] However, it still remains a challenge to grow large-scale TMDC monolayer films with a large single-crystalline domain size that is suitable for practical devices.

Most of the CVD processes used for growing TMDC monolayers have involved the use of a solid transition metal oxide powder as a precursor (e.g. MoO_3), and it has been shown that controlling the nucleation reaction at the initial growth stage is an important factor in obtaining a large domain size.[26,30-31] For example, some research groups have tried to induce nucleation and growth by placing the growth substrate upside down, facing directly towards the MoO_3 powder.[16,26,32-34] With this powder-based approach, however, it is not easy to obtain a uniform

large-area monolayer film reproducibly because of the limited control over the nucleation density, resulting from the fast kinetic reactions at high temperatures, and the non-uniform distribution of the MoO_3 powder. As a result, clean monolayer crystals tend to grow only in a specific area where the MoO_3 vapor concentration is relatively low (e.g. at the sides of the substrates).[16,33,35] For this reason, there have been many alternative attempts carried out to control the nucleation density by placing the growth substrate away from the precursor,[30,36-40] or adjusting the oxygen flow,[41] argon flow,[42] growth temperature,[43-44] as well as the furnace position during the growth process.[31] However, these have all resulted in a non-uniform and position-dependent crystal quality, a relatively small crystal size, low coverage, or a contaminated film. From this perspective, it is highly desirable to develop a new growth protocol in order to achieve precise control over the nucleation density even at high temperatures for synthesizing large-scale, highly crystalline, and uniform TMDC monolayers.

In this chapter, a new method for synthesizing a uniform, large-area TMDC monolayer film with large-sized single-crystal grains via a solution-processed precursor deposition technique is presented. Using this method, a thin precursor film with an extremely small amount of MoO_3 (~0.01 mg) has been prepared on the source substrate, which induces low supersaturation and hence reduces the nucleation density dramatically down to 32 nuclei mm^{-2} over the whole substrate surface with a thermodynamically stable environment even at a high temperature of around $T = 800°C$. As a result, a highly-crystalline and centimeter-scale MoS_2 monolayer has been grown directly onto the SiO_2 substrates, and single crystals with a large size of up to 500 μm have been readily observed over the substrate. It is found that the TMDC monolayer possesses an excellent optical quality with a very small full-width-half-maximum (FWHM) of ~48 meV, which is comparable to or even better than that of exfoliated and

suspended single crystal TMDC monolayers. It is also demonstrated that the growth strategy can be extended to the growth of other TMDC monolayers such as WS_2, and that it can be used to fabricate robust TMDC heterostructure devices due to the large crystal sizes. The MoS_2/WS_2 heterostructure devices, fabricated using the synthesis technique introduced in this work, show rectifying properties and exhibit a faster photoresponse of ~45 ms than that observed for single TMDC monolayer photodetectors because of the built-in potential at the heterojunction. In addition, a considerably high photoresponsivity of ~40 AW^{-1}, compared to that of minority-carrier dominant p-n junction devices using TMDC monolayers, is achieved due to the high photogain that arises from the majority carrier transport at the unipolar n-n heterojunction.

3.2. Synthesis of MoS_2 monolayers

3.2.1. Solution-processed precursor deposition

The synthesis of the MoS_2 monolayer was performed by using MoO_3 and sulfur as the precursors. Instead of using a solid powder precursor, a facile and economical method for solution-processed precursor deposition was devised so as to induce a relatively low supersaturation state from the vapor reactants, leading to a reduced nucleation density, which is essential for the growth of large-sized crystals.[45-46] MoO_3 powder rarely dissolves in water and exhibits a white opaque color, however, it is highly soluble in ammonium hydroxide (NH_4OH) (Figure 3-1a). The dissolved precursor solution in NH_4OH (20 mg/ml) was then spincoated at 3000 rpm for 1 min onto the SiO_2 substrate that was treated with oxygen plasma for 10 minutes (Figure 3-1b). The deposited MoO_3 film was then annealed at 300°C for 10 minutes before the growth process in order to completely remove the solvent. Figure 3-1c and

Figure 3-2a clearly show that the deposited MoO_3 film exhibits a uniform and single-color contrast in comparison with the blank SiO_2 substrate. The roughness of the film was significantly small with a root mean square (RMD) thickness variation of 0.482 nm, which indicates the formation of a uniform film thickness (Figure 3-2b). The weight of the deposited film can be calculated from the thickness measured using AFM and the density of MoO_3 (Figure 3-2c,d). Figure 3-2c was intentionally taken at the edge of the substrate, where the SiO_2 substrate was exposed. The bright and thick areas between the MoO_3 film and the SiO_2 substrate were thought to be formed by a centrifugal force when spin-coating the film. In Figure 3-2d, the thickness of the film was found to be 11 nm. The deposited amount of MoO_3 (~0.01 mg) could be easily calculated from the measured thickness, the substrate area (2 cm^2), and the density of MoO_3 (6.49 g/cm^3). It is worth noting that the amount of MoO_3 precursor in this work was 2-3 orders of magnitude lower and much more uniformly distributed than that of solid precursors that are typically used in other reports,[16,30] which ensures that the precursor vapor concentration remains significantly low during the growth process.

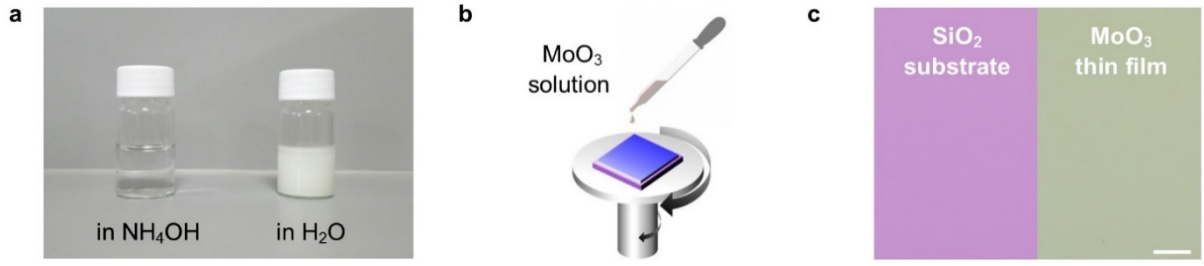

Figure 3-1. Preparation of a MoO_3 thin film. a) MoO_3 solution in NH_4OH and in H_2O. b) Deposition of the MoO_3 film onto the SiO_2 substrate by spin-coating the MoO_3 solution. c) Optical images of the blank SiO_2 substrate and the MoO_3 film. Scale bar: 10 μm.

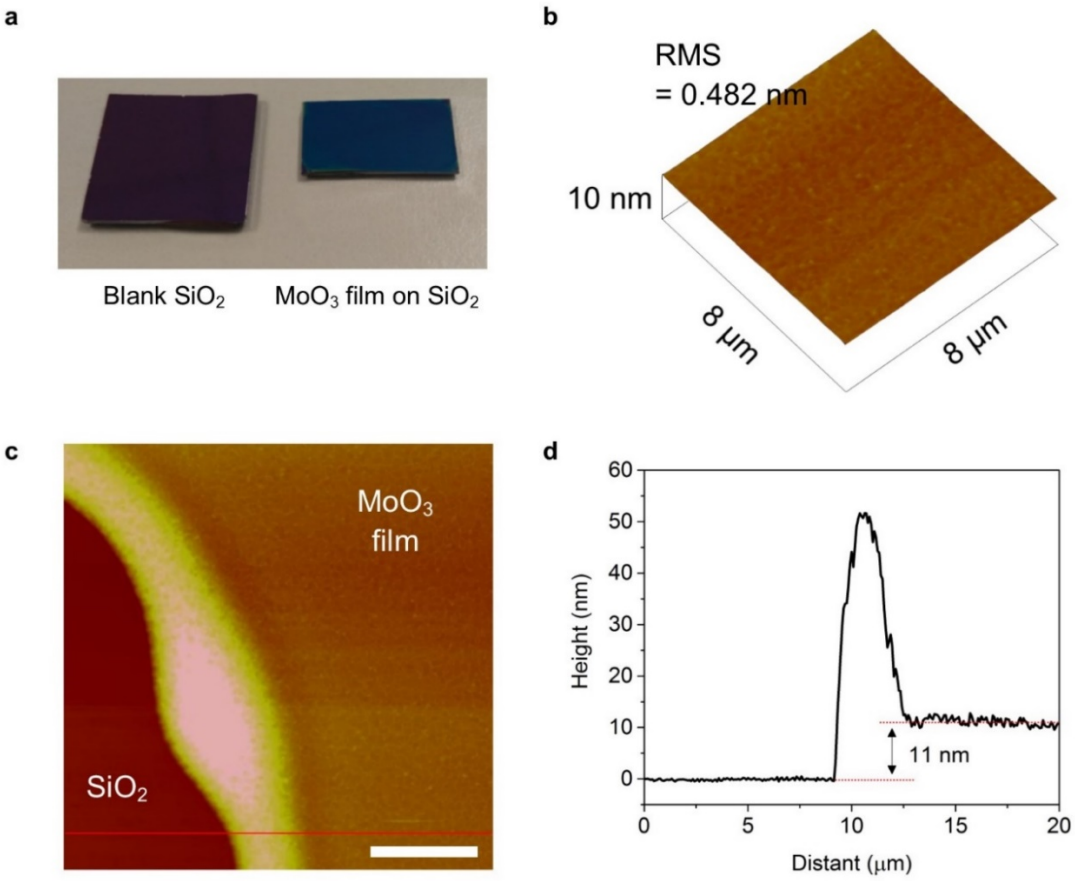

Figure 3-2. AFM images of a deposited MoO_3 film on SiO_2. a) Optical images of the blank SiO_2 substrate (2 x 2 cm^2, left) and the spin-coated MoO_3 film on the SiO_2 substrate (2 x 1 cm^2, right). b) 3D AFM image of the MoO_3. c) AFM image of the MoO_3 film. Scale bar: 5 μm. d) AFM height profile along the red line in (b).

3.2.2. CVD synthesis process

The CVD process was conducted in a quartz tube using a furnace under atmospheric pressure as shown in Figure 3-3a. A SiO_2 substrate with a MoO_3 film deposited by the solution-processed method was used as the source substrate. The source substrate was then placed in an alumina crucible in the middle of the 50-mm quartz tube. All the crucibles were used after annealing them in a furnace at T = 1000°C for over 1 hour at atmospheric pressure to

completely remove any precursor residue. In addition, long inner tubes inside the outer tubes were replaced with new or clean ones for each growth process. The growth substrate was loaded upside down above the crucible. Another crucible containing 50 mg of sulfur powder was placed upstream. The CVD growth process was then performed at atmospheric pressure with a continuous flow of pure argon gas. The temperature of the furnace was raised to 300°C and remained at that temperature for 20 minutes under a 1000 sccm flow of argon gas so as to remove the oxygen and water in the tube, before the temperature was then increased to T = 800 °C at a rate of 20 °C/min with 150 sccm of argon.

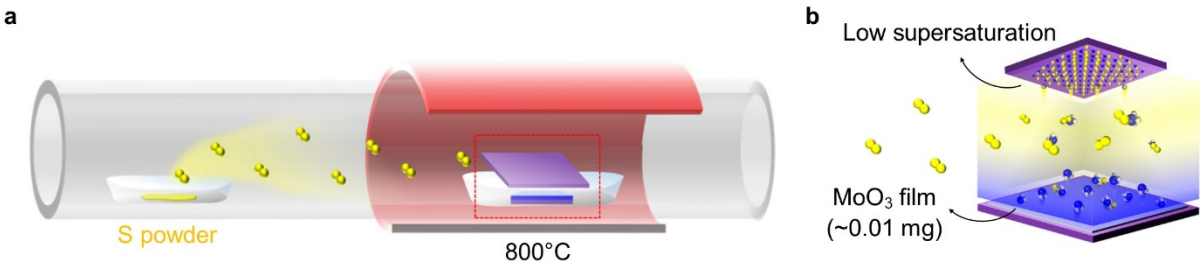

Figure 3-3. Growth of a MoS_2 monolayer film. a) Illustration of the synthesis process. b) Enlarged diagram of the source substrate and the target substrate in the red-dashed box shown in (a).

3.2.3. Control of growth parameters

The growth temperature (800 °C) was much higher than that used in previous reports,[16,26,28,47] in order to maximize the crystal size due to the high diffusivity of the precursor and the increased number of active species generated at the high temperature, compared to lower temperature growth processes (Figure 3-4). The sublimed sulfur was transported downstream by the Ar carrier gas when the temperature of the furnace approached $T \sim 720$°C and then sulfurized precursor molecules induced a supersaturation state around the substrate, which results in the nucleation of MoS_2. At this stage, it is important to note that the extremely small

amount of precursor in the solution-processed thin film results in a significantly low supersaturation level near the substrate, which leads to a very low nucleation density on the surface (Figure 3-3b). Due to the significantly low nucleation density, the growth of the MoS_2 monolayer diffuses extensively along the surface with little disturbance from neighboring crystals. As a result, a uniform centimeter-scale MoS_2 monolayer film has been obtained within a growth time of 5 minutes as shown in Figure 3-5a. While the continuous MoS_2 monolayer film was found on the center of the substrate (Figure 3-5b), large triangular crystals with a size ranging from 200 to 400 μm were found to meet each other to form interconnected shapes on the edges of the substrate where the flow of the precursor was insufficient (Figure 3-5c). The size of the largest triangular crystals was found to reach up to 500 μm (Figure 3-5d).

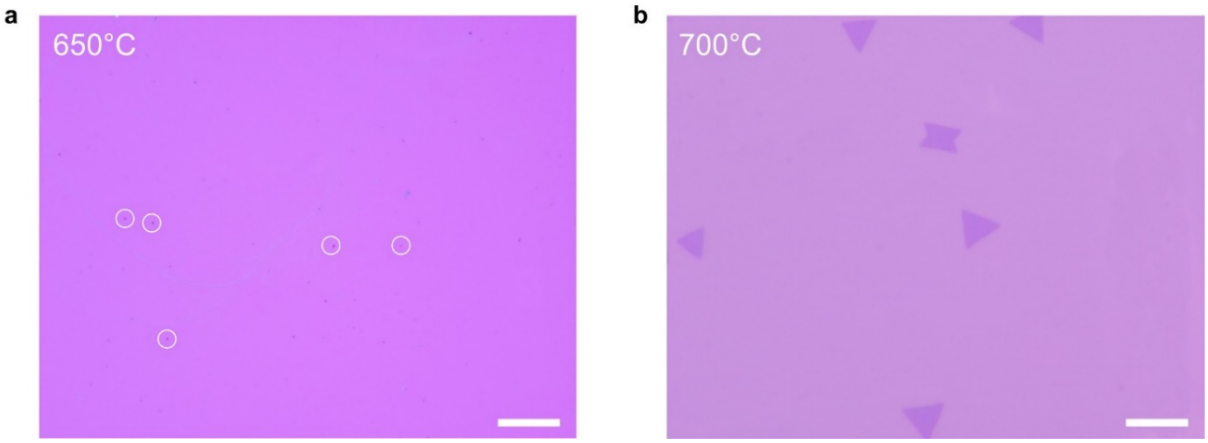

Figure 3-4. Optical images of MoS_2 crystals grown at low temperatures. a) Optical image of the substrate grown at T = 650°C shows only small particles, some of which are marked with circles. Scale bar: 100 μm. b) The small crystals were found on the substrate grown at T = 700°C. Scale bar: 100 μm. These results indicate that the low temperature process is not suitable for large-scale growth in this work because of the low vapor concentration resulting from the extremely small amount of precursor.

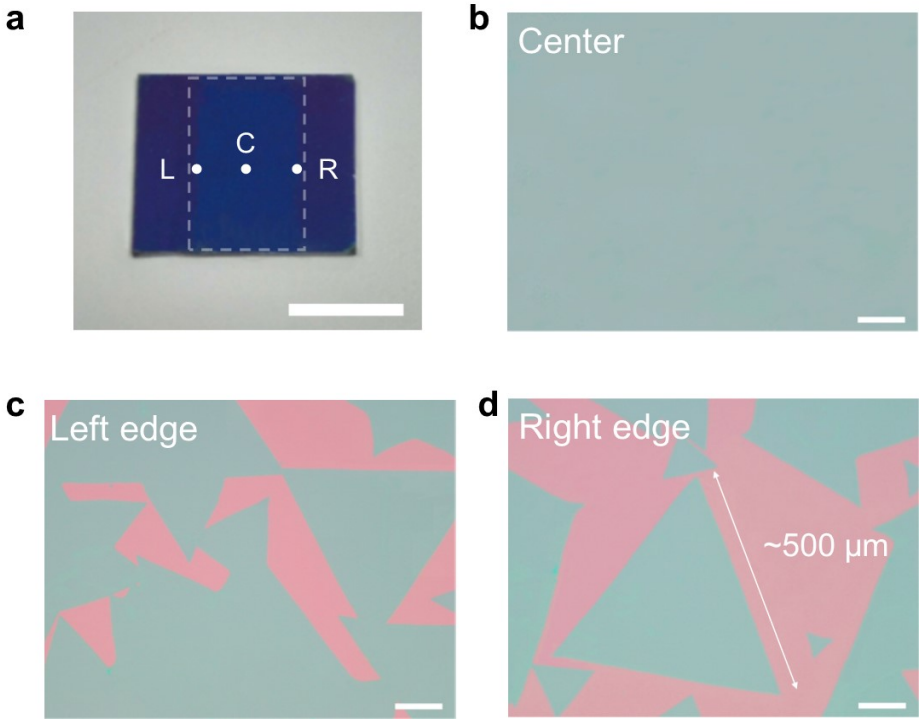

Figure 3-5. Optical images of MoS_2 monolayers grown at 800°C. a) Optical image of the as-grown MoS_2 film. The film was grown mainly on the area directly exposed to MoO_3 inside the crucible. Scale bar: 1 cm. b-d) Typical images of MoS_2 crystals grown in the center, the left edge, and the right edge of the substrate, as marked in (a). Scale bars: 100 μm.

To identify whether the crystal size could be enlarged, the growth time was increased to 30 minutes (Figure 3-6). However, the size of the crystals observed on the edge was almost within the same range as those grown for 5 minutes. Interestingly, the monolayer film was rarely contaminated by additional nucleation or growth upon the crystals even during the relatively long growth time. Furthermore, the grain size was also similar to that of the crystals grown on the edge, even though grain boundaries were observed in some parts of the film (Figure 3-6b), which might be associated with a grain boundary uplifting phenomenon

frequently found when using long growth times or high precursor concentrations.[48] These results indicate that the growth process was almost completed within a 5 minute period, without any overgrowth due to a small precursor supply, therefore, the crystals were rarely contaminated by the additional growth time even at the center of the substrate where the supersaturation level is expected to be at its highest. On the contrary, when the MoO_3 precursor powder (10 mg) was used in the growth process, noticeable contamination was found at the center of the substrate by the bombardment of small particles that nucleated on the surface of the crystals (Figure 3-7). Collectively, these results show that the monolayer films grown by the solution-processed precursor deposition is insensitive to the growth time, which can be advantageous for practical applications, along with the use of an extremely small amount of precursor and the large size of the crystals that are obtained.

It is worthwhile to mention that the solution-processed precursor deposition used in this chapter makes it much easier to control the nucleation reaction during the initial growth stage, compared to the general powder-based approach.[16,26,32-34] With the powder-type precursors, it is much more difficult to produce a clean and uniform monolayer film because of a relatively high supersaturation level of precursors during the synthesis process. However, the solution-processed precursor deposition can make the supersaturation level significantly low, which decreases the nucleation density dramatically and increases the domain size of the monolayer film. In addition, the solution-processed precursor deposition can be much more easily prepared without any complex control process, compared to other large-scale growth strategies such as placing the growth substrate away from the precursor,[30,36-40] or adjusting the oxygen flow,[41] argon flow,[42] growth temperature,[43-44] as well as the furnace position[31] during the growth process. For these reasons, the solution-processed precursor deposition was used for growing TMDC monolayers throughout the thesis.

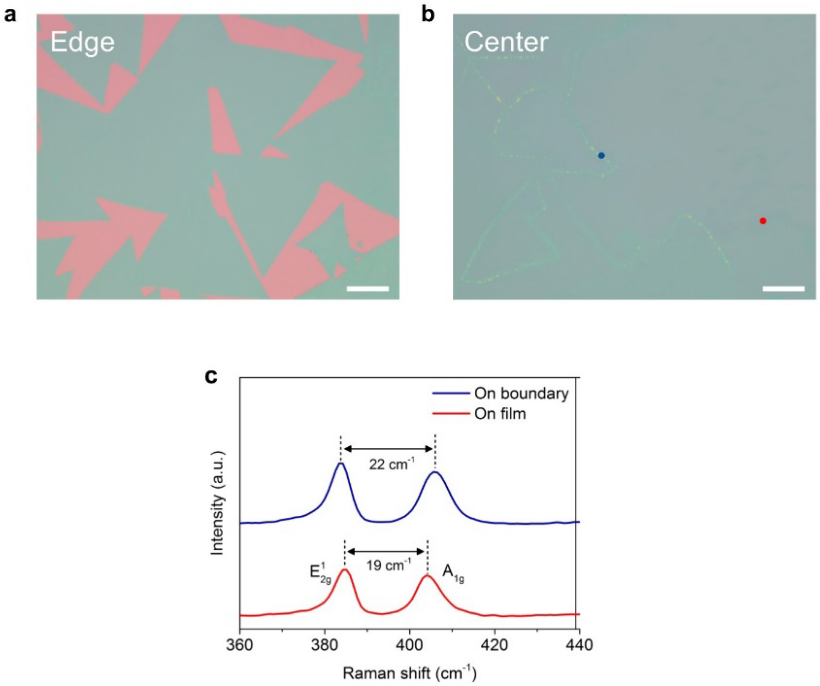

Figure 3-6. MoS_2 monolayer grown for 30 minutes. a) Optical image on the edge of the substrate. Scale bar: 100 µm. b) Optical image at the centre of the substrate. Scale bar: 100 µm. c) The Raman spectrum at the boundary (blue dot in (b)) showed that the thickness corresponds to approximately 2-3 layers, while the Raman spectrum on the film (red dot in (b)) indicated that it was single-layered.

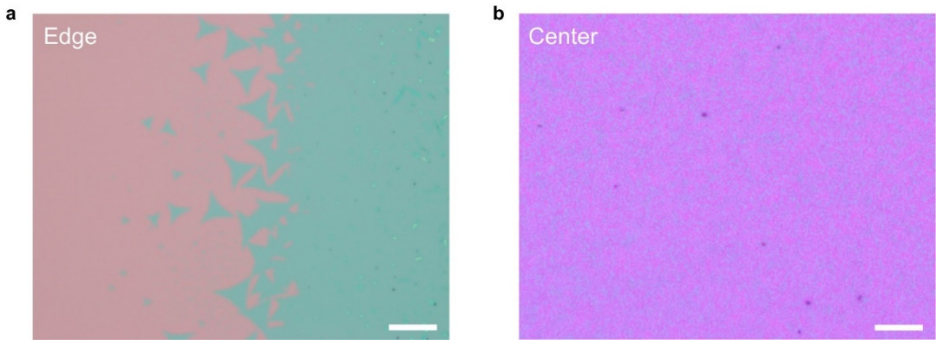

Figure 3-7. Powder-based MoS_2 monolayer growth. a) Optical image of MoS_2 crystals on the edge of the substrate grown with 10 mg of MoO_3 powder. The image shows clearly that the merged monolayer film was contaminated by the additional nucleation of particles. Scale bar: 100 µm. b) The crystals were completely contaminated on the centre of the substrate because of the high vapor concentration of the precursor. Scale bar: 100 µm.

3.3. Characterization of MoS_2 monolayers

3.3.1. AFM, Raman and PL analysis of MoS_2 monolayers

The quality of the monolayer MoS_2 film was characterized by AFM, Raman spectroscopy, and PL spectroscopy. Figure 3-8 shows a typical AFM topography image of the MoS_2 crystal grown in this work. The height profile shows that the thickness of the MoS_2 crystal is around 0.8 nm, corresponding to a MoS_2 monolayer. The Raman spectrum also demonstrates that the frequency difference between the E^1_{2g} and A_{1g} peak is ~18.8 cm^{-1} (Figure 3-9a), which is a clear signature of a monolayer of MoS_2 as explained in Chapter 1.4. The frequency difference between two vibrational modes is expected to be much larger over 25 cm^{-1} in the bulk form of MoS_2, while it becomes smaller when the thickness of the layer decreases down to one layer because the interlayer van der Waals interaction and the long-range Coulombic interaction in MoS_2 becomes weaker. It is also well-known that the quality of the crystal can be clearly assessed using PL measurements. Figure 3-9b shows the PL intensity normalized to the intensity of the A_{1g} Raman peak. Noticeably, the PL intensity of the monolayer grown from the solution-processed precursor deposition is much more intense than that observed for the monolayer fabricated using the solid powder-based growth process. (Figure 3-10a-c). The FWHM was found to be as small as 48 meV, which is similar to or in some cases better than that observed for exfoliated and suspended crystals.[13,49] In addition, the crystal grown in a low supersaturation level is found to have similar or better electrical properties in the FET configuration, showing a higher mobility of 17 $cm^2\ V^{-1}\ s^{-1}$ than that of the exfoliated one (10 $cm^2\ V^{-1}\ s^{-1}$). From these results it is believed that the MoS_2 crystals grown under low supersaturation conditions are highly crystalline.

The distinct difference in optical properties can be explained by the additional nucleation and crystal growth process, which can be easily initiated under a high

supersaturation condition when using a relatively large amount of precursor.[29,31-32,50] However, with an extremely small amount of precursor, a continuous growth of the crystal is preferred over multiple nucleation sites because the low supersaturation level limits any additional nucleation processes. Therefore, the crystals grown in a low supersaturation environment exhibit a very clean surface, which is why they show much clearer and sharper spectra in the Raman and PL measurements and is indicative of a high-quality monolayer. Figure 3-11 also reinforces this finding as it shows the Raman mapping images for the E^1_{2g} and A_{1g} peaks along with a PL map at 667 nm, highlighting that a single crystal exhibits a good uniformity.

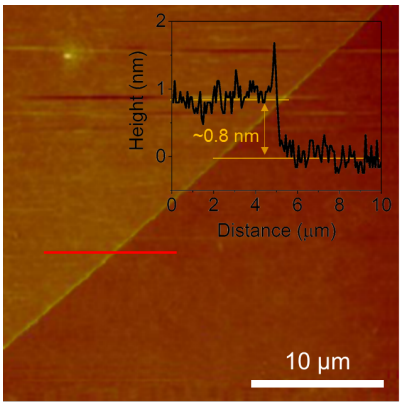

Figure 3-8. AFM image of a MoS_2 monolayer crystal. The inset shows that the thickness of the crystal corresponds to a MoS_2 monolayer. Scale bar: 10 μm.

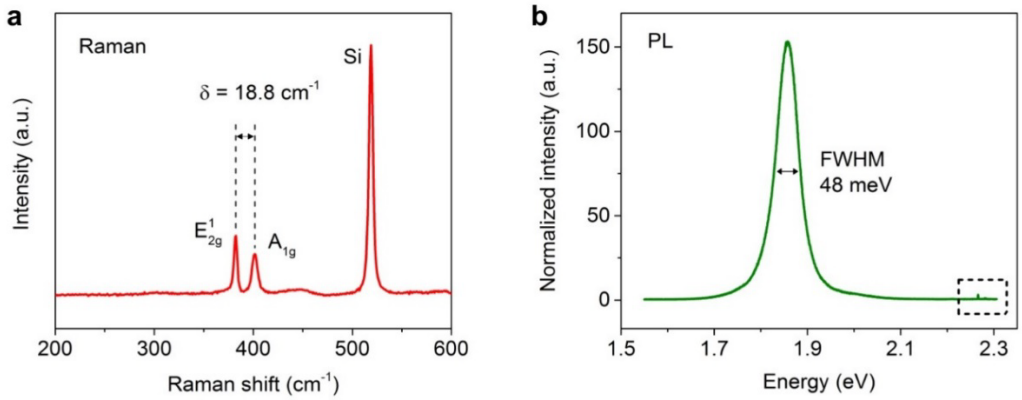

Figure 3-9. Raman and PL spectrum of MoS_2 monolayers. a) Raman spectrum of the MoS_2 monolayer. b) PL spectrum of the MoS_2 monolayer normalized to the intensity of the A_{1g} peak. The Raman peaks of MoS_2 and SiO_2 in the dashed box appear to be negligible because the PL peak is extremely intense.

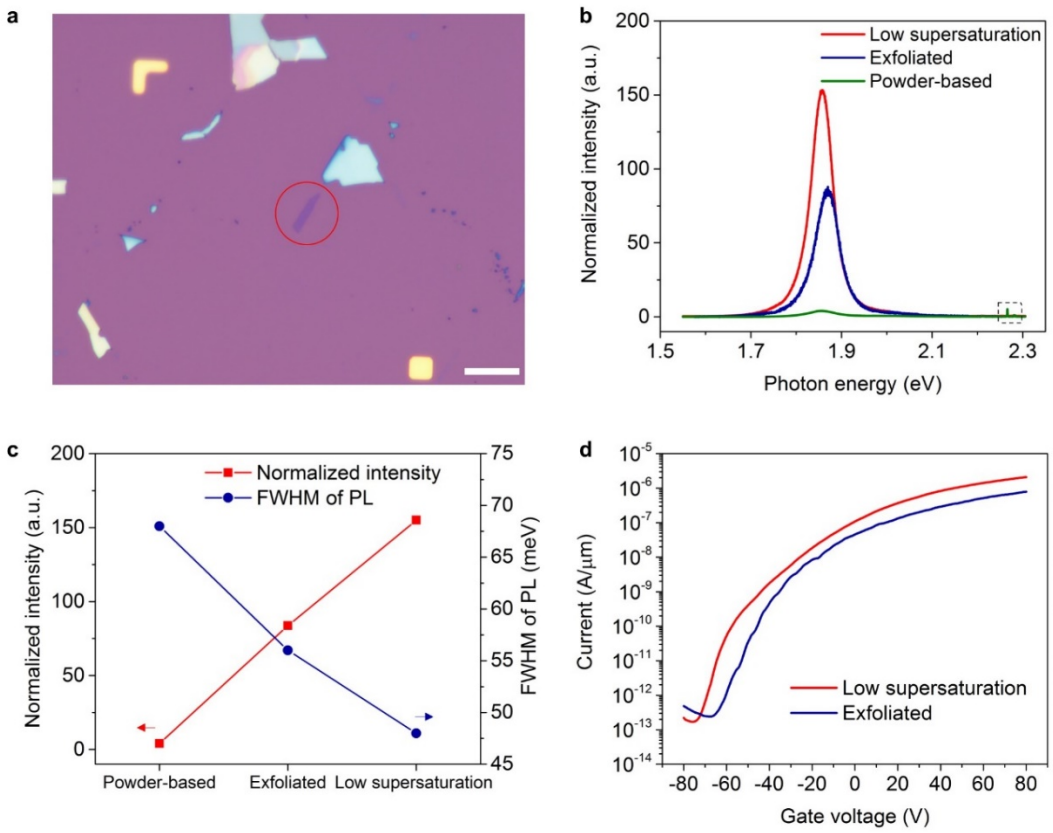

Figure 3-10. Comparison of the resultant crystal quality between the exfoliated crystal and the crystal grown under a low supersaturation level. a) Optical image of the exfoliated monolayer (in the red circle). Scale bar: 10 μm. b) PL spectra of the monolayer grown under low supersaturation conditions, the exfoliated monolayer and the powder-based CVD grown monolayer. The PL intensities were normalized to the intensity of the A_{1g} peak for comparison. The dashed box indicates the locations of the Raman peaks of MoS_2 and SiO_2. c) Comparison of the normalized PL intensity (primary axis) and the FWHM (secondary axis) of the PL peaks. d) Transfer curves of the field-effect transistors (FETs) fabricated from the exfoliated monolayer and the monolayer grown under low supersaturation conditions. The measurement was conducted in air inside a probe station.

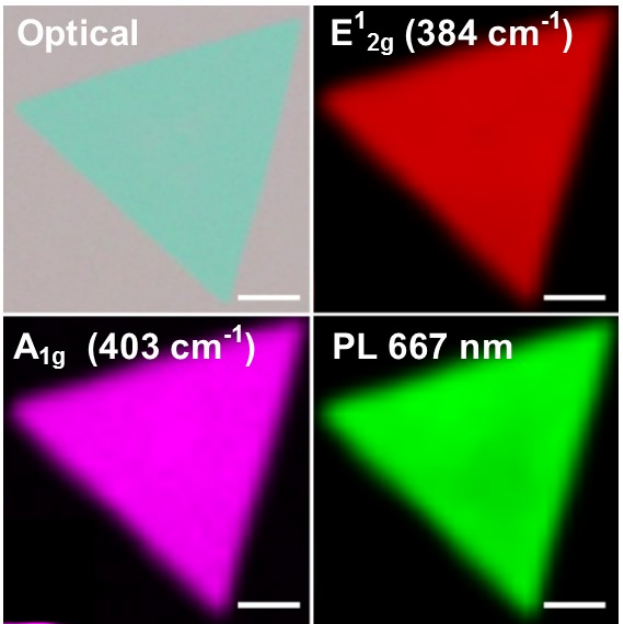

Figure 3-11. Optical image of a MoS_2 crystal and the corresponding Raman and PL mapping images. Scale bars: 20 μm.

3.3.2. Uniformity of MoS_2 monolayers

To assess the homogeneity of the MoS_2 monolayer film over the whole substrate, Raman spectra were also taken at 50 different locations on the substrate (inset of Figure 3-12a). The statistical values as a function of position are plotted in Figure 3-12a. The standard deviation in the difference in Raman frequencies between the E^1_{2g} and A_{1g} peaks was found to be significantly small (0.3 cm^{-1}) with an average value of 19.1 cm^{-1}. Likewise, the FWHM of the E^1_{2g} peak also showed a small variation of 0.16 cm^{-1} and an average value of 3.5 cm^{-1}. This trend was found to be even more striking for the PL spectra (Figure 3-12b). The position of the PL peak was found to be almost the same at 1.86 eV over the entire substrate with a small standard deviation of 1.1 meV; the FWHM also did not change and was found to be 50 meV with a standard deviation of 1.54 meV. In addition, the results of the Raman and PL

measurements taken from different growth substrates were also found to be comparably similar (Figure 3-13). The Raman frequency difference between the E^1_{2g} and A_{1g} peaks from 12 different samples was consistent at an average value of ~18.9 cm^{-1} with a standard deviation of 0.35 cm^{-1}. The FWHM of the E^1_{2g} peak showed an average value of 3.4 cm^{-1} with a standard deviation of 0.26 cm^{-1}. These average values were almost identical to those of the results shown in Figure 3-12a. Although the standard deviations across 12 different growth substrates were a little bit higher than those observed in Figure 3-12a, they were within a reasonable range. b) The position and FWHM of the PL peaks. The average values of the position of the PL peak (1.86 eV) and the FWHM of the PL spectra (52 meV) were similar to those presented in Figure 3-12b. The corresponding standard deviations (3.3 meV and 1.99 meV, respectively) increased slightly, compared to the values shown in Figure 3-12b. However, it is reasonable that the standard deviations from the different substrates in (a) and (b) were a little larger than those from the same substrate (Figure 3-12a,b). These results demonstrate the batch-to-batch reproducibility of the growth process. These results clearly highlight the uniformity and the reproducibility of the monolayer film grown using the method introduced in this work.

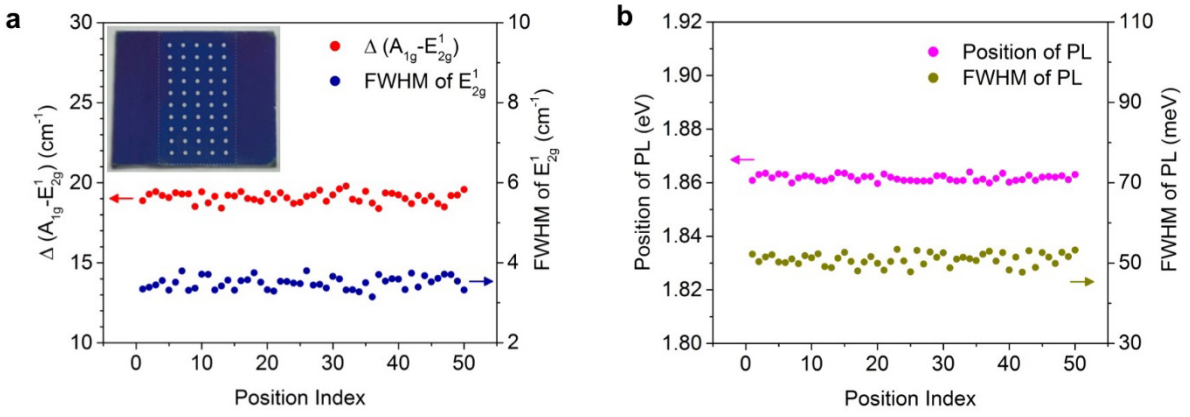

Figure 3-12. Uniformity of the MoS_2 monolayer growth over the substrate. a) The frequency difference between the E^1_{2g} and A_{1g} peaks, and the FWHM of the E^1_{2g} peak collected from 50 different locations across the substrate (inset shows the corresponding locations). b) The peak energy (eV, primary axis) and the FWHM (secondary axis) of the PL spectra measured from the same locations as shown in (a).

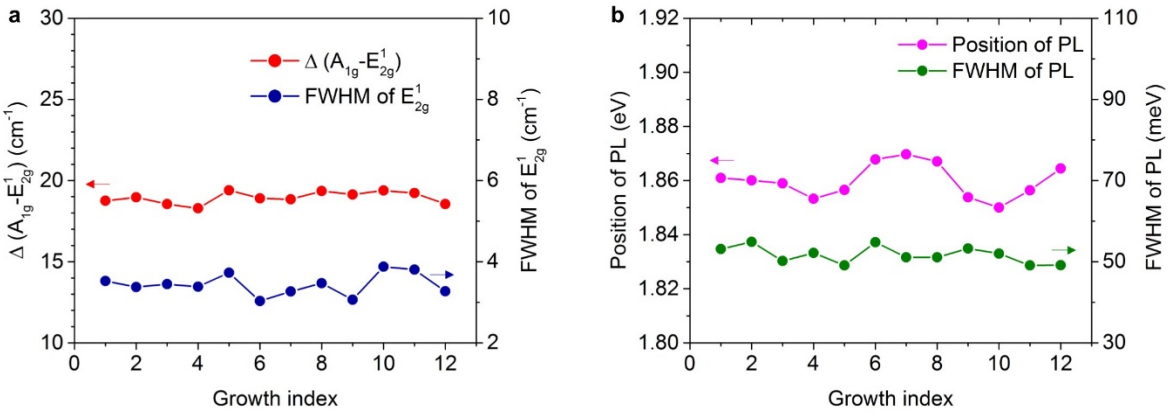

Figure 3-13. Raman and PL measurements from 12 different growth substrates. a) Raman frequency difference between the E^1_{2g} and the A_{1g} peak, and the FWHM of the E^1_{2g} peak. The primary and secondary y-axes in (a) and (b) were fixed to the same scale as that in Figure 3-12a,b for comparison.

3.3.3. TEM analysis of MoS_2 monolayers

The crystal structure of the MoS_2 monolayer was observed directly using high-resolution TEM, selected area electron diffraction (SAED), and annular dark-field scanning transmission electron microscopy (ADF-STEM). The MoS_2 crystals transferred onto a gold grid show a clear surface and well-organized honeycomb structure without any defect sites, and the corresponding hexagonal symmetrical SAED pattern confirms that the MoS_2 sample is indeed a single-crystal (Figure 3-14a). The ADF-STEM image also clearly shows the atomic model of MoS_2 along with the spatial distribution of the Mo and S atoms (Figure 3-14b). These findings suggest that the sample has been grown with a high crystalline quality.

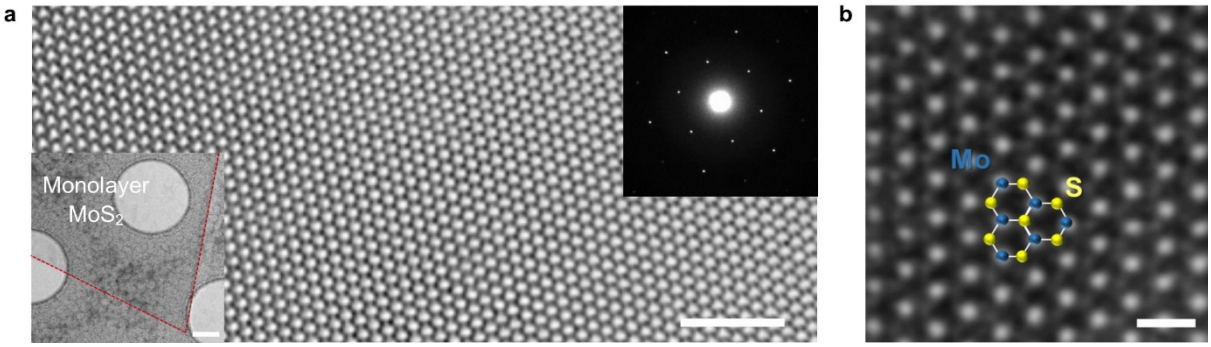

Figure 3-14. TEM images of a MoS_2 monolayer film. a) High-resolution TEM image of a MoS_2 monolayer. Scale bar: 2 nm. Left inset: crystal on the TEM grid. Scale bar: 500 μm. Top Right inset: SAED image confirming the hexagonal structure. b) ADF-STEM image representing the defect-free hexagonal structure of the monolayer. The bright spots are Mo atoms and the grey spots are two stacked S atoms. Scale bar: 0.5 nm.

3.4. Effects of the supersaturation level on the growth of a monolayer

To further investigate the effect of the supersaturation level on the growth of a monolayer, the synthesis was carried out with various solution-processed precursor films deposited using different concentrations of the MoO_3 solution. The growth process was performed using a similar method to that described previously, except that the growth time was reduced to 3 minutes in order to investigate the grain size more clearly before the crystals merge with each other. By controlling the precursor amount from 0.001 to 1 mg, the effects of the supersaturation level on the nucleation density and the grain size could be clearly observed.

Figure 3-15a-e shows optical images in the center of the substrate from each growth experiment. For a precursor amount of 0.001 mg, crystals with a size ranging from 10 to 30 μm were found to be distributed very sparsely over the substrate, and the nucleation density was found to be only 9 mm^{-2} (Figure 3-15f). As the precursor amount was increased to 0.01 mg, the

nucleation density and the average crystal size also rose gradually to ~32 mm^{-2} and ~300 μm, respectively. However, this growth trend was significantly altered above a precursor amount of 0.01 mg. The crystal size was reduced to 30 μm when the precursor amount was increased to 0.1 mg, yet the nucleation density was found to be very high, greater than 1200 mm^{-2}. Finally, when the precursor amount reached 1 mg, it was found that the center of the substrate was completely contaminated by a much higher nucleation density that resulted from the smaller MoS_2 particles that were less than 1 μm in size because of the large supply of precursor and the high reactant accumulation. It is worth noting that the average coverage and the nucleation density increased with the amount of MoO_3; however, the size of the crystal was found to be largest at a precursor amount of 0.01 mg.

From these results, it is proposed that there are two distinct growth regimes with a transition point around 0.01 mg. For an extremely low precursor concentration, the low supersaturation leads to a relatively low nucleation rate, which guarantees that thermodynamically stable reactions occur during the growth process.[33,51] In a thermodynamically favored process, reactive atoms have enough time to diffuse to energetically favorable locations, leading to the formation of a stable and high-crystalline structure, which is known to result in a triangular shape. It was confirmed that the shapes of all the crystals grown below a precursor amount of 0.01 mg were approximately equilateral triangles due to the thermodynamically stable condition being satisfied. On the other hand, a large amount of precursor above 0.01 mg causes a higher supersaturation level and a much faster nucleation process, resulting in an instability in the reaction. As a result, the crystal growth process is dominated mainly by a kinetic-controlled reaction process rather than a thermodynamically stable process.[33,51]

In the kinetic-controlled regime, it is not easy for Mo and S atoms to diffuse to the energetically favorable sites because of the high reaction rate. Therefore, the size of the crystals

became very small in this regime. In addition, the geometrical configuration of the crystals were less triangular in shape, and instead truncated triangles or round-shaped domains were formed. These findings suggest that large-scale and highly crystalline TMDC monolayers can be obtained under a thermodynamically-controlled regime by balancing the nucleation and growth rates during the synthesis process.

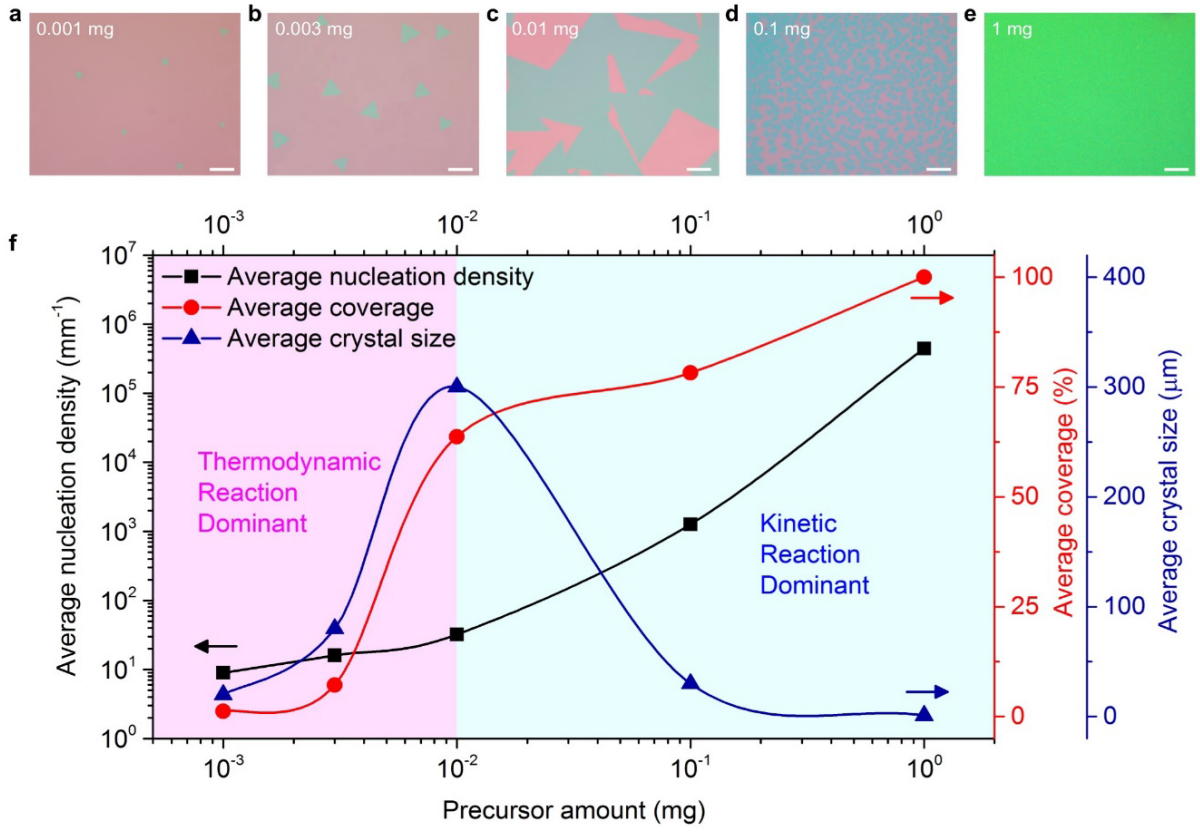

Figure 3-15. The effect of the supersaturation level on the growth of the monolayer. a-e) Optical images of the crystals grown with different amounts of MoO_3 ranging from 0.001 to 1 mg. The images were taken at the center of each substrate. Scale bars: 100 μm. f) Average nucleation density (primary axis), average coverage (secondary axis in red), and average crystal size (secondary axis in blue) as a function of the amount of MoO_3 precursor.

3.5. Extension to WS_2 monolayers

To investigate whether the strategy proposed here to reduce the nucleation density for large single crystals can be applied to other TMDC monolayers, the solution-processed precursor deposition was applied to the growth of WS_2. Unlike the MoO_3 powder, WO_3 powder does not dissolve in H_2O or NH_4OH at room temperature, showing an opaque yellowish colour (Figure 3-16a). However, it does dissolve completely in NH_4OH after sonicating and stirring for 120 minutes at $T \sim 90$°C on a hot-plate. The growth of the WS_2 monolayer was conducted using a similar process to that described for the MoS_2 monolayer except that the growth temperature was increased to $T = 950$°C and the distance between the source substrate and the target substrate was reduced to less than 5 mm. This is because the vapour pressure of WO_3 is much lower than that of MoO_3. In addition, the higher diffusivity of the precursor at higher temperatures could contribute to an increase in the crystal size.

Figure 3-16b shows that large-sized WS_2 monolayer crystals have been grown on the SiO_2 substrate, and the crystal size had increased up to 360 μm with a low nucleation density of 27 mm^{-2}. The Raman spectrum taken with a 532 nm excitation laser shows two peaks at 351 cm^{-1} and 417 cm^{-1}, and the intensity of the E^1_{2g} peak was found to be much larger than that of the A_{1g} peak, which clearly shows that the crystal was single-layered (Figure 3-16c). A strong PL peak at 630 nm was also found to be evidence for the direct band gap of the WS_2 monolayer (Figure 3-16d). The FWHM of the PL peak was only 38 meV. These results suggest that the WS_2 monolayer grown under a low supersaturation condition is highly crystalline. Raman and PL mapping data also confirm the uniform quality of the WS_2 monolayer (Figure 3-16e-g).

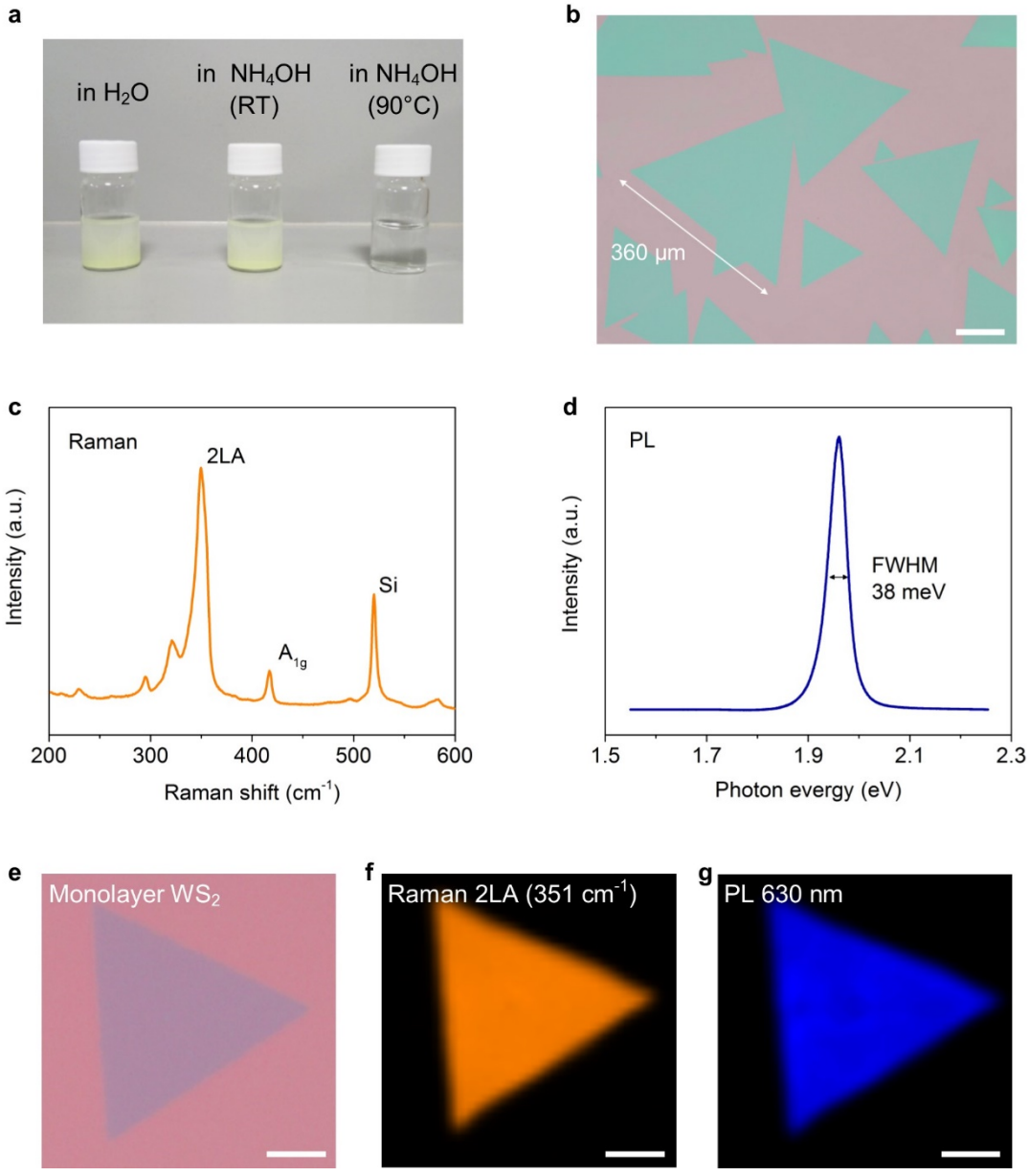

Figure 3-16. Low supersaturation synthesis of a WS_2 monolayer. a) WO_3 solution in H_2O and in NH_4OH at room temperature (RT), and in NH_4OH after sonicating and stirring at $T = 90°C$. b) Optical image of the WS_2 monolayer. Scale bar: 100 µm. c) Raman spectrum of a WS_2 crystal. d) PL spectrum of a WS_2 crystal. e-g) Optical image, Raman mapping (2LA), and PL mapping of the WS_2 monolayer. Scale bars: 20 µm.

3.6. TMDC n-n vertical heterostructured devices

The proposed strategy to control the nucleation density for large single crystals and promote crystal growth under a thermodynamically stable condition can be generalized to other TMDC monolayers such as WS_2 as described in Figure 3-16. As a result, this can facilitate the fabrication of not only homogeneous device arrays, but also robust heterostructure devices by virtue of the large-sized crystals. A few studies have been reported on p-n junction photodetectors that have focused on improving the slow response time of 2D monolayer photodetectors.[52-56] However, in each case, they have all sacrificed the high photosensitivity of the TMDC monolayer and exhibited a very low photoresponsivity much less than that of Si-based photodetectors ($< 1\ AW^{-1}$) because of the short carrier lifetimes caused by minority carrier transport. To avoid this issue, a unipolar n-n heterojunction based on majority carrier transport processes was developed so as to maintain the high photoresponsivity of the TMDC monolayer whilst at the same time improving the response time.

The MoS_2/WS_2 heterojunction devices were fabricated by transferring the WS_2 monolayer on top of the MoS_2 monolayer. The polymethyl methacrylate (PMMA) liquid was spin-coated onto the substrate with the WS_2 monolayers at 3000 rpm for 1 minute. The substrate was then annealed at $T = 120°C$ for 10 minutes and soaked in a 1M KOH solution. After the PMMA film attached to the WS_2 monolayer film was separated from the SiO_2 substrate, it was then floated on clean water to cleanse the film. Transferring the WS_2 monolayer to the top of the MoS_2 monolayer was done in ethanol as soaking TMDC monolayers in water can result in a breaking of the monolayer films. After the PMMA was

dissolved by the acetone and washed using ethanol, a stacked MoS_2/WS_2 heterojunction device was obtained. The electrodes were formed on each monolayer outside the overlapped region and were drawn parallel with the junction. For better contact, the heterojunction device was annealed before the measurements so as to completely remove water molecules that might exist at the junction or on the substrate. Figures 3-17a,b show the synthesized MoS_2/WS_2 heterostructured devices. The overlapped region can be clearly distinguished by the optical contrast in Figure 3-17b.

The Raman spectrum can be used to investigate the vertical stacked MoS_2/WS_2 region. As expected, the Raman spectrum at the junction shows the typical vibrational modes of both the MoS_2 and WS_2 monolayers together (Figure 3-17c). However, the out-of-plane A_{1g} peak of WS_2 on the overlapped layers became noticeably stronger than that observed for the WS_2 monolayer, and was a little blue-shifted by 1.7 cm^{-1} due to a stiffening of the vibrational mode, which is consistent with an increase in the number of layers.[57] In addition, the frequency difference of MoS_2 also became slightly larger, similar to that observed in a few-layered MoS_2 crystals. On the other hand, the intensity of each PL peak became noticeably weaker when the layers were combined into a heterostructure (Figure 3-17d). The reduction in PL intensity can be attributed to the transition towards an indirect band gap due to an increase in the thickness, similar to that found in single TMDC layers, or the efficient exciton dissociation at the junction because of the built-in potential of the type II heterostructure.[58-60] These findings demonstrate the vertically-stacked MoS_2/WS_2 heterostructure, fabricated by transferring one layer onto the other layer, was properly formed by interlayer Van der Walls force.

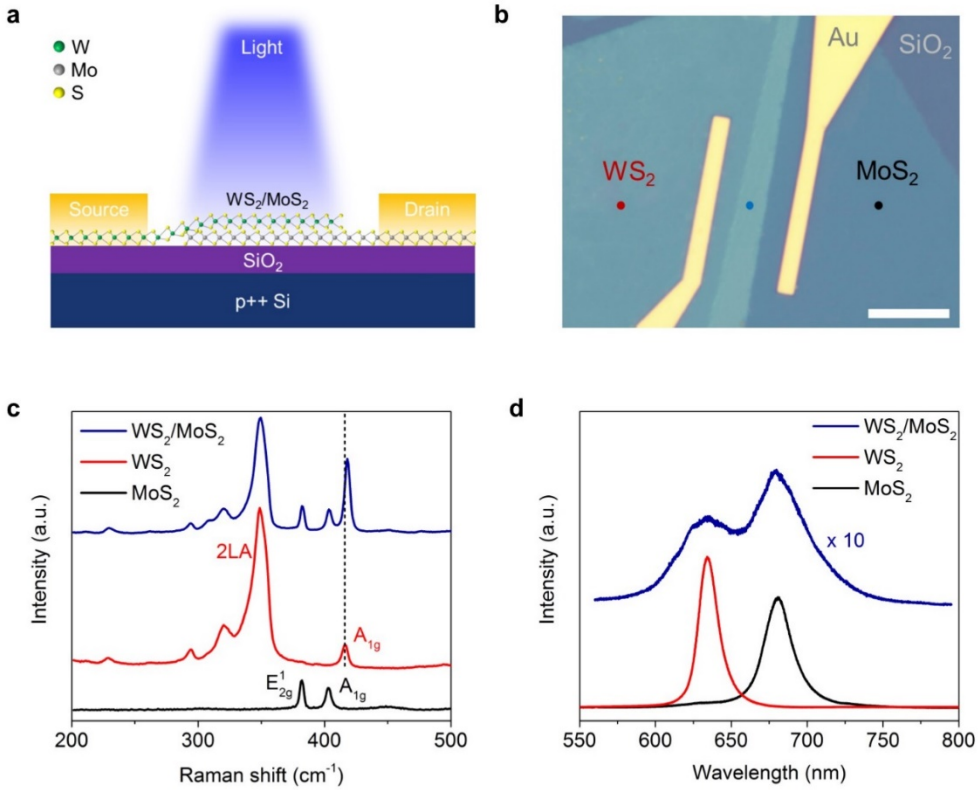

Figure 3-17. MoS_2/WS_2 vertical heterojunction devices. a) Illustration of the MoS_2/WS_2 heterojunction devices. b) Optical image of the MoS_2/WS_2 heterojunction device. Scale bar: 10 μm. c) Raman spectra measured at the junction (blue), on the WS_2 crystal (red), and on the MoS_2 crystal (black). d) PL spectra measured from the same spot in (c).

Figures 3-18a,b show that the I-V curves of the MoS_2/WS_2 heterostructure device exhibit rectifying behavior due to the type II junction. The on/off ratio could be controlled by the gate voltage and reached up to around 500 at a gate voltage of V_g = -10 V. However, the channel was found to be thoroughly depleted below a gate voltage of V_g = -30 V. When the heterojunction forms a type-II junction, some electrons are transferred from WS_2 to MoS_2 (Figure 3-18c). Unlike p-n junctions, the transfer of holes occurs relatively less frequently as both monolayers have n-type semiconducting properties. The transferred electrons leave behind an electron depletion region in WS_2, and develop an electron accumulation region in

MoS_2, resulting in the formation of a built-in potential between the junction (Figure 3-18d). When a positive bias is applied, both the electron depletion region and the electron accumulation region decrease, resulting in a concomitant decrease in the built-in potential across the junction, which makes it much easier for electrons to pass the junction. On the contrary, for a negative bias, the built-in potential increases and thus fewer electrons can then overcome the barrier.

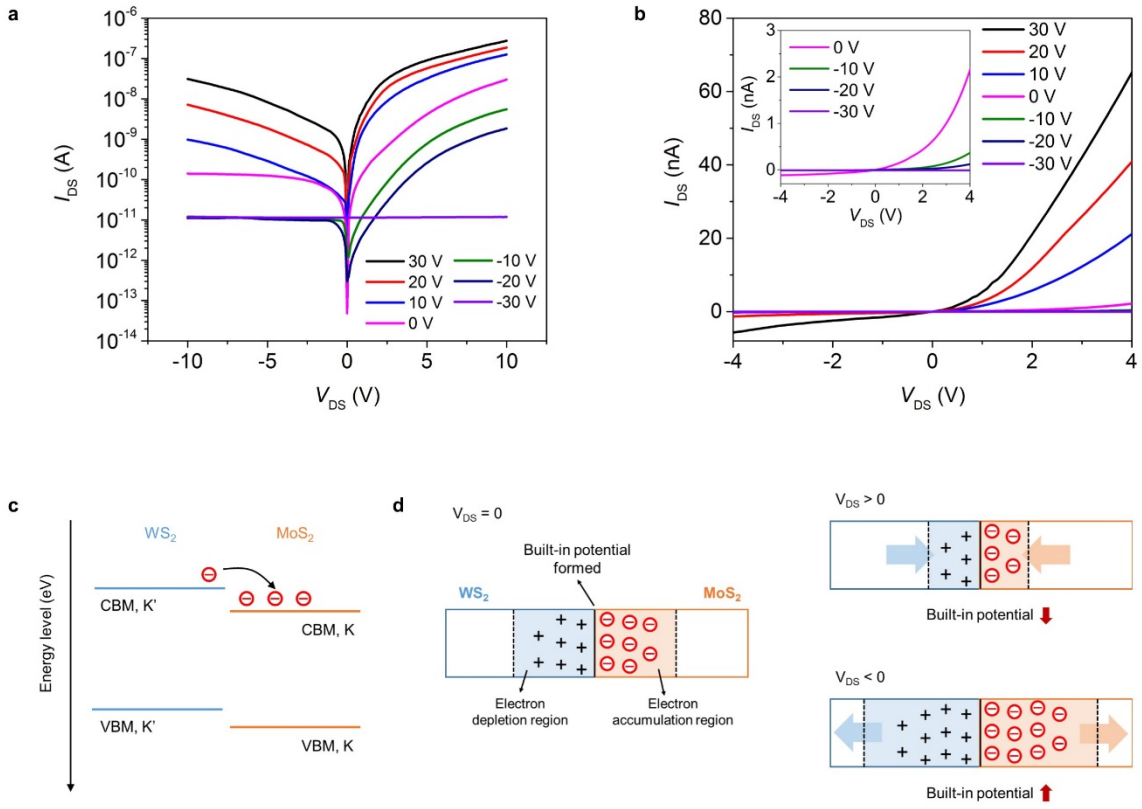

Figure 3-18. I-V curves and the operation principle of MoS_2/WS_2 vertical heterostructured devices. a) I-V curves of the heterojunction device at different gate voltages plotted on a logarithmic scale. b) I-V curves of the heterojunction device plotted on a linear scale. The inset shows an enlarged region of the plot for a gate voltage of below V_g = 0 V. c) Illustration of the band alignment of a MoS_2/WS_2 heterojunction. When the heterojunction forms, electrons on the WS_2 side are transferred to the MoS_2 side due to the difference in the energy levels. d) Schematic of the heterojunction at V_{DS} = 0, at V_{DS} > 0, and at V_{DS} < 0. The size of the built-in potential varies according to the bias.

Figure 3-19a shows the photoresponse of the device at forward bias (V_{DS} = 3 V) in the time domain when illuminated with blue laser light (λ = 450 nm). The photoresponsivity (R) of the device at forward bias, estimated by the equation $R = I_{ph}/P$, where I_{ph} is the photocurrent and P is the absorbed laser power, was found to be measurably high at ~178 A/W even at zero gate bias voltage. However, the response time was found to be extremely slow at τ_{rise} = 30 s, which is typically observed in single MoS_2 monolayer photodetectors.[5,61] It is known that the photoresponse dynamics of 2D materials are significantly affected by their surroundings, such as the underlying substrates and gas molecules from the environment.[5,62] These external factors induce trap states in the monolayer, which cause a slow response time in single TMDC monolayer photodetectors (Figure 3-20), yet at the same time contribute to a large photogain due to the prolonged recombination time.[61] As the small potential barrier in the device almost vanishes at forward bias, the carriers released from the trap sites by incident photons can flow through the channel even after the incident light is turned off. Therefore, the device at forward bias operates similar to that of single TMDC monolayer photodetectors with a long response time.

A different trend was observed in the photoresponse at reverse bias as shown in Figure 3-19b. The photoresponse became much faster with a rise time of 45 ms (Figure 3-19c). Even though the photoresponsivity decreased to ~40 AW^{-1}, it is still much higher than that of the p-n junction photodiodes that have been reported previously based upon TMDC monolayers.[52-56] The photogain (G), the ratio of collected electrons to photons absorbed per second, is calculated to be higher than 18, even when assuming that the absorption rate of the photons is 100%. The high photoresponsivity is thought to originate from the high photogain. A photogain greater than unity is not usually observed in p-n junction photodetectors because the minority

carrier transport dominates the device, which results in a short carrier lifetime. The results from the devices at reverse bias show that the n-n TMDC monolayer heterostructure photodetectors can significantly improve the response time, while maintaining the photoresponsivity at a considerably high level; this is because the operating principle of the device is based upon the majority carrier transport in the n-n heterojunction where the carrier lifetime is relative long compared to that of a conventional p-n junction.

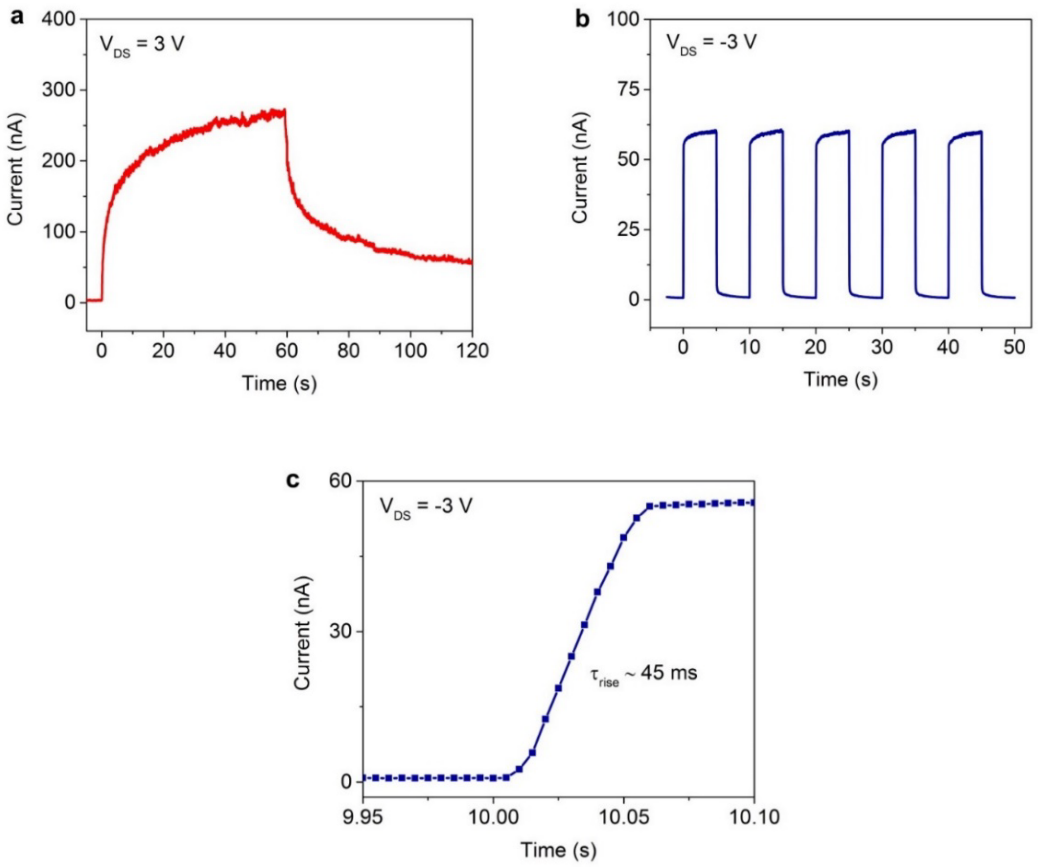

Figure 3-19. Photoresponse of MoS_2/WS_2 vertical heterojunction devices. a) Photoresponse of the heterojunction device at $V_{DS} > 0$. A blue laser (450 nm, 0.76 mW/cm^2) was incident on the junction for 60 s. b) Photoresponse at $V_{DS} < 0$. Light was illuminated for 5 s with a period of 10 s. c) The rise time was measured from the enlarged plot when the light was on.

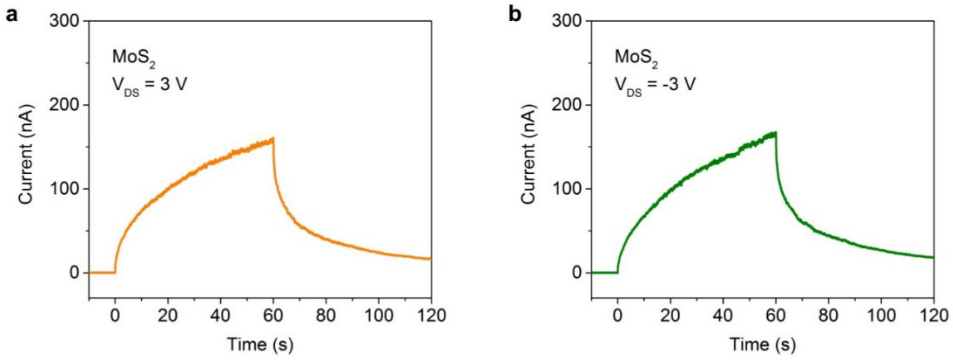

Figure 3-20. Photoresponse of MoS_2 monolayer photodetectors. a) Photoresponse at V_{DS} = 3 V. b) Photoresponse at V_{DS} = -3 V. Unlike the MoS_2/WS_2 heterostructure device, the MoS_2 photodetector did not show any noticeable difference between positive and negative bias.

3.7. Conclusions

In conclusion, large-scale and highly-crystalline MoS_2 monolayer films have been directly synthesized on a SiO_2 substrate using solution-processed precursor deposition. The relatively small amount of metal oxide precursor creates a low supersaturation level and thus reduces nucleation density, which in turn facilitates the growth of large-sized and highly-crystalline crystals under a thermodynamically stable reaction. This approach can produce a highly-crystalline monolayer film and can be much more easily implemented in the CVD equipment, compared to the other growth techniques reported. In addition, this strategy can be easily applied to other TMDC monolayers such as WS_2 and makes it possible to fabricate robust TMDC heterostructure devices due to the fact that the crystal sizes are large. Specifically, a unipolar n-n MoS_2/WS_2 heterojunction device is found to exhibit an improved response time, which is one of the drawbacks when using TMDC monolayer photodetectors, without losing the high photoresponsivity of the TMDC monolayer due to a majority carrier transport. The current findings, especially the synthesis process and strategy, can also be of significant importance in the growth of lateral TMDC heterostructured monolayers, which will be discussed in the next chapter.

3.8. References

[1] B. Radisavljevic, A. Radenovic, J. Brivio, V. Giacometti, A. Kis. Single-layer MoS_2 transistors. *Nature. Nanotechnology* 6, 147-150 (2011).

[2] B. Radisavljevic, A. Kis. Mobility engineering and a metal–insulator transition in monolayer MoS_2. *Nature Materials* 12, 815-820 (2013).

[3] J. Wang, Q. Yao, C. W. Huang, X. Zou, L. Liao, S. Chen, Z. Fan, K. Zhang, W. Wu, X. Xiao, C. Jiang, W. W. Wu. High mobility MoS_2 transistor with low Schottky barrier contact by using atomic thick h-BN as a tunneling layer. *Advanced Materials* 28, 8302-8308 (2016).

[4] X. Li, L. Yang, M. Si, S. Li, M. Huang, P. Ye, Y. Wu. Performance potential and limit of MoS_2 transistors. *Advanced Materials* 27, 1547-1552 (2015).

[5] O. Lopez-Sanchez, D. Lembke, M. Kayci, A. Radenovic, A. Kis. Ultrasensitive photodetectors based on monolayer MoS_2. *Nature Nanotechnology* 8, 497-501 (2013).

[6] W. Zhang, J. K. Huang, C. H. Chen, Y. H. Chang, Y. J. Cheng, L. J. Li. High-gain phototransistors based on a CVD MoS_2 monolayer. *Advanced Materials* 25, 3456-3461 (2013).

[7] X. Wang, P. Wang, J. Wang, W. Hu, X. Zhou, N. Guo, H. Huang, S. Sun, H. Shen, T. Lin, M. Tang, L. Liao, A. Jiang, J. Sun, X. Meng, X. Chen, W. Lu, J. Chu. Ultrasensitive and broadband MoS_2 photodetector driven by ferroelectrics. *Advanced Materials* 27, 6575-6581 (2015).

[8] Z. Yin, H. Li, H. Li, L. Jiang, Y. Shi, Y. Sun, G. Lu, Q. Zhang, X. Chen, H. Zhang. Single-layer MoS_2 phototransistors. *ACS Nano* 6, 74-80 (2012).

[9] D. Lee, E. Hwang, Y. Lee, Y. Choi, J. Kim, S. Lee, J. Cho. Multibit MoS_2 photoelectronic memory with ultrahigh sensitivity. *Advanced Materials* 28, 9196-9202 (2016).

[10] M. Chen, H. Nam, S. Wi, G. Priessnitz, I. Gunawan, X. Liang. Multibit data storage states formed in plasma-treated MoS_2 transistors. *ACS Nano* 8, 4023-4032 (2014).

[11] M. Choi, G.-H. Lee, Y.-J. Yu, D.-Y. Lee, S. Lee, P. Kim, J. Hone, W. Yoo. Controlled charge trapping by molybdenum disulphide and graphene in ultrathin heterostructured memory devices. *Nature Communications* 4, 1624 (2013).

[12] J. Lee, S. Pak, Y.-W. Lee, Y. Cho, J. Hong, P. Giraud, H. Shin, S. M. Morris, J. Sohn, S. Cha, J. Kim. Monolayer optical memory cells based on artificial trap-mediated charge storage and release. *Nature Communications* 8, 14734 (2017).

[13] K. F. Mak, C. Lee, J. Hone, J. Shan, T. F. Heinz. Atomically thin MoS_2: a new direct-gap semiconductor. *Physical Review Letters* 105, 136805 (2010).

[14] H. Lee, S.-W. Min, Y.-G. Chang, M. Park, T. Nam, H. Kim, J. Kim, S. Ryu, S. Im. MoS2 nanosheet phototransistors with thickness-modulated optical energy gap. *Nano Letters* 12, 3695-3700 (2012).

[15] S.-W. Min, H. Lee, H. Choi, M. Park, T. Nam, H. Kim, S. Ryu, S. Im. Nanosheet thickness-modulated MoS_2 dielectric property evidenced by field-effect transistor performance. *Nanoscale* 5, 548-551 (2012).

[16] A. M. van der Zande, P. Y. Huang, D. A. Chenet, T. C. Berkelbach, Y. You, G.-H. Lee, T. F. Heinz, D. R. Reichman, D. A. Muller, J. C. Hone. Grains and grain boundaries in highly crystalline monolayer molybdenum disulphide. *Nature Materials* 12, 554-561 (2013).

[17] K.-K. Liu, W. Zhang, Y.-H. Lee, Y.-C. Lin, M.-T. Chang, C.-Y. Su, C.-S. Chang, H. Li, Y. Shi, H. Zhang, C.-S. Lai, L.-J. Li. Growth of large-area and highly crystalline MoS_2 thin layers on insulating substrates. *Nano Letters* 12, 1538-1544 (2012).

[18] J. Yang, Y. Gu, E. Lee, H. Lee, S. Park, M.-H. Cho, Y. Kim, Y.-H. Kim, H. Kim. Wafer-scale synthesis of thickness-controllable MoS_2 films via solution-processing using a dimethylformamide/n -butylamine/2-aminoethanol solvent system. *Nanoscale* 7, 9311-9319 (2015).

[19] A. S. George, Z. Mutlu, R. Ionescu, R. J. Wu, J. S. Jeong, H. H. Bay, Y. Chai, A. K. Mkhoyan, M. Ozkan, C. S. Ozkan. Wafer scale synthesis and high resolution structural characterization of atomically thin MoS_2 Layers. *Advanced Functional Materials* 24, 7461-7466 (2014).

[20] M. I. Serna, S. H. Yoo, S. Moreno, Y. Xi, J. Oviedo, H. Choi, H. N. Alshareef, M. J. Kim, M. Minary-Jolandan, M. A. Quevedo-Lopez. Large-area deposition of MoS_2 by pulsed laser deposition with in-situ thickness control. *ACS Nano* 10, 6054-6061 (2016).

[21] J. D. Yao, Z. Q. Zheng, J. M. Shao, G. W. Yang. Stable, highly-responsive and broadband photodetection based on large-area multilayered WS_2 films grown by pulsed-laser deposition. *Nanoscale* 7, 14974-14981 (2015).

[22] T. A. J. Loh, D. H. C. Chua, A. T. S. Wee. One-step synthesis of few-layer WS_2 by pulsed laser deposition. *Scientific Reports* 5, 18116 (2015).

[23] G. Tai, T. Zeng, J. Yu, J. Zhou, Y. You, X. Wang, H. Wu, X. Sun, T. Hu, W. Guo. Fast and large-area growth of uniform MoS_2 monolayers on molybdenum foils. *Nanoscale* 8, 2234-2241 (2015).

[24] A. Tarasov, P. M. Campbell, M. Y. Tsai, Z. R. Hesabi, J. Feirer, S. Graham, J. W. Ready, E. M. Vogel. Highly uniform trilayer molybdenum disulfide for wafer-scale device fabrication. *Advanced Functional Materials* 24, 6389-6400 (2014).

[25] Y.-C. Lin, W. Zhang, J.-K. Huang, K.-K. Liu, Y.-H. Lee, C.-T. Liang, C.-W. Chu, L.-J. Li. Wafer-scale MoS_2 thin layers prepared by MoO_3 sulfurization. *Nanoscale* 4, 6637-6641 (2012).

[26] Y. H. Lee, X. Q. Zhang, W. Zhang, M. T. Chang, C. T. Lin, K. D. Chang, Y. C. Yu, J. Wang, C. S. Chang, L. J. Li, T. W. Lin. Synthesis of large-area MoS_2 atomic layers with chemical vapor deposition. *Advanced Materials* 24, 2320-2325 (2012).

[27] S. Najmaei, Z. Liu, W. Zhou, X. Zou, G. Shi, S. Lei, B. I. Yakobson, J.-C. Idrobo, P. M. Ajayan, J. Lou. Vapour phase growth and grain boundary structure of molybdenum disulphide atomic layers. *Nature Materials* 12, 754-759 (2013).

[28] D. Dumcenco, D. Ovchinnikov, K. Marinov, P. Lazić, M. Gibertini, N. Marzari, O. Sanchez, Y.-C. Kung, D. Krasnozhon, M.-W. Chen, S. Bertolazzi, P. Gillet, A. i Morral, A. Radenovic, A. Kis. Large-area epitaxial monolayer MoS_2. *ACS Nano* 9, 4611-4620 (2015).

[29] I. Bilgin, F. Liu, A. Vargas, A. Winchester, M. K. L. Man, M. Upmanyu, K. M. Dani, G. Gupta, S. Talapatra, A. D. Mohite, S. Kar. Chemical vapor deposition synthesized atomically thin molybdenum disulfide with optoelectronic-grade crystalline quality. *ACS Nano* 9, 8822-8832 (2015).

[30] X. Ling, Y.-H. H. Lee, Y. Lin, W. Fang, L. Yu, M. S. Dresselhaus, J. Kong. Role of the seeding promoter in MoS_2 growth by chemical vapor deposition. *Nano Letters* 14, 464-472 (2014).

[31] J. Chen, W. Tang, B. Tian, B. Liu, X. Zhao, Y. Liu, T. Ren, W. Liu, D. Geng, H. Jeong, H. Shin, W. Zhou, K. Loh. Chemical Vapor Deposition of High-quality large-sized MoS_2 crystals on silicon dioxide substrates. *Advanced Science* 3, 1500033 (2016).

[32] Y.-H. Lee, L. Yu, H. Wang, W. Fang, X. Ling, Y. Shi, C.-T. Lin, J.-K. Huang, M.-T. Chang, C.-S. Chang, M. Dresselhaus, T. Palacios, L.-J. Li, J. Kong. Synthesis and transfer of single-layer transition metal disulfides on diverse surfaces. *Nano Letters* 13, 1852-1857 (2013).

[33] S. Wang, Y. Rong, Y. Fan, M. Pacios, H. Bhaskaran, K. He, J. Warner. Shape evolution of monolayer MoS_2 crystals grown by chemical vapor deposition. *Chemistry of Materials* 26, 6371-6379 (2014).

[34] J. Wu, H. Schmidt, K. Amara, X. Xu, G. Eda, B. Özyilmaz. Large thermoelectricity via variable range hopping in chemical vapor deposition grown single-layer MoS_2. *Nano Letters* 14, 2730-2734 (2014).

[35] H. Schmidt, S. Wang, L. Chu, M. Toh, R. Kumar, W. Zhao, A. H. Neto, J. Martin, S. Adam, B. Özyilmaz, G. Eda. Transport properties of monolayer MoS_2 grown by chemical vapor deposition. *Nano Letters* 14, 1909-1913 (2014).

[36] J. Zhang, H. Yu, W. Chen, X. Tian, D. Liu, M. Cheng, G. Xie, W. Yang, R. Yang, X. Bai, D. Shi, G. Zhang. Scalable growth of high-quality polycrystalline MoS_2 monolayers on SiO_2 with tunable grain sizes. *ACS Nano* 8, 6024-6030 (2014).

[37] Y. Wan, H. Zhang, K. Zhang, Y. Wang, B. Sheng, X. Wang, L. Dai. Large-scale synthesis and systematic photoluminescence properties of monolayer MoS_2 on fused silica. *ACS Applied Materials Interfaces* 8, 18570-18576 (2016).

[38] H. Phan, Y. Kim, J. Lee, R. Liu, Y. Choi, J. Cho, C. Lee. Ultraclean and Direct Transfer of a Wafer-scale MoS_2 thin film onto a plastic substrate. *Advanced Materials* 29, 1603928 (2017).

[39] J. Jeon, S. Jang, S. Jeon, G. Yoo, Y. Jang, J.-H. Park, S. Lee. Layer-controlled CVD growth of large-area two-dimensional MoS_2 films. *Nanoscale* 7, 1688-1695 (2014).

[40] Z. Tu, G. Li, X. Ni, L. Meng, S. Bai, X. Chen, J. Lou, Y. Qin. Synthesis of large monolayer single crystal MoS_2 nanosheets with uniform size through a double-tube technology. *Applied Physical Letters* 109, 223101 (2016).

[41] W. Chen, J. Zhao, J. Zhang, L. Gu, Z. Yang, X. Li, H. Yu, X. Zhu, R. Yang, D. Shi, X. Lin, J. Guo, X. Bai, G. Zhang. Oxygen-assisted chemical vapor deposition growth of large single-crystal and high-quality monolayer MoS_2. *Journal of the American Chemical Society* 137, 15632-15635 (2015).

[42] Y. Gong, G. Ye, S. Lei, G. Shi, Y. He, J. Lin, X. Zhang, R. Vajtai, S. T. Pantelides, W. Zhou, B. Li, P. M. Ajayan. Synthesis of millimeter-scale transition metal dichalcogenides single crystals. *Advanced Functional Materials* 26, 2009-2015 (2016).

[43] S. Wang, M. Pacios, H. Bhaskaran, J. H. Warner. Substrate control for large area continuous films of monolayer MoS_2 by atmospheric pressure chemical vapor deposition. *Nanotechnology* 27, 085604 (2016).

[44] H. Zhou, C. Wang, J. C. Shaw, R. Cheng, Y. Chen, X. Huang, Y. Liu, N. O. Weiss, Z. Lin, Y. Huang, X. Duan. Large area growth and electrical properties of p-type WSe_2 atomic layers. *Nano Letters* 15, 709-713 (2015).

[45] Z. Yan, J. Lin, Z. Peng, Z. Sun, Y. Zhu, L. Li, C. Xiang, L. E. Samuel, C. Kittrell, J. M. Tour. Toward the synthesis of wafer-scale single-crystal graphene on copper foils. *ACS Nano* 6, 9110-9117 (2012).

[46] G. Lu, T. Wu, Q. Yuan, H. Wang, H. Wang, F. Ding, X. Xie, M. Jiang. Synthesis of large single-crystal hexagonal boron nitride grains on Cu-Ni alloy. *Nature Communications* 6, 6160 (2015).

[47] W. Park, J. Baik, T.-Y. Kim, K. Cho, W.-K. Hong, H.-J. Shin, T. Lee. Photoelectron spectroscopic imaging and device applications of large-area patternable single-layer MoS_2 synthesized by chemical vapor deposition. *ACS Nano* 8, 4961-4968 (2014).

[48] Q. Ji, Y. Zhang, T. Gao, Y. Zhang, D. Ma, M. Liu, Y. Chen, X. Qiao, P.-H. Tan, M. Kan, J. Feng, Q. Sun, Z. Liu. Epitaxial monolayer MoS_2 on mica with novel photoluminescence. *Nano Letters* 13, 3870-3877 (2013).

[49] D. Sercombe, S. Schwarz, D. O. Pozo-Zamudio, F. Liu, B. J. Robinson, E. A. Chekhovich, Tartakovskii, II, O. Kolosov, A. I. Tartakovskii. Optical investigation of the natural electron doping in thin MoS_2 films deposited on dielectric substrates. *Scientific Reports* 3, 3489 (2013).

[50] Y. Yoo, Z. P. Degregorio, J. E. Johns. Seed crystal homogeneity controls lateral and vertical heteroepitaxy of monolayer MoS_2 and WS_2. *Journal of the American Chemical Society* 137, 14281-14287 (2015).

[51] S. Xie, M. Xu, T. Liang, G. Huang, S. Wang, G. Xue, N. Meng, Y. Xu, H. Chen, X. Ma, D. Yang. A high-quality round-shaped monolayer MoS_2 domain and its transformation. *Nanoscale* 8, 219-225 (2015).

[52] M. M. Furchi, A. Pospischil, F. Libisch, J. Burgdörfer, T. Mueller. Photovoltaic effect in an electrically tunable van der Waals heterojunction. *Nano Letters* 14, 4785-4791 (2014).

[53] A. Pezeshki, S. Shokouh, T. Nazari, K. Oh, S. Im. Electric and photovoltaic behavior of a few-layer α-$MoTe_2$/MoS_2 dichalcogenide heterojunction. *Advanced Materials.* 28, 3216-3222 (2016).

[54] P. Jeon, S.-W. Min, J. Kim, S. Raza, K. Choi, H. Lee, Y. Lee, D. Hwang, H. Choi, S. Im. Enhanced device performances of WSe_2-MoS_2 van der Waals junction p–n diode by fluoropolymer encapsulation. *Journal of Materials Chemistry C* 3, 2751-2758 (2015).

[55] Y. Deng, Z. Luo, N. J. Conrad, H. Liu, Y. Gong, S. Najmaei, P. M. Ajayan, J. Lou, X. Xu, P. D. Ye. Black phosphorus-monolayer MoS_2 van der Waals heterojunction p-n diode. *ACS Nano* 8 (2014).

[56] C.-H. Lee, G.-H. Lee, A. M. van der Zande, W. Chen, Y. Li, M. Han, X. Cui, G. Arefe, C. Nuckolls, T. F. Heinz, J. Guo, J. Hone, P. Kim. Atomically thin p-n junctions with van der Waals heterointerfaces. *Nature Nanotechnology* 9, 676-681 (2014).

[57] J. Zhang, J. Wang, P. Chen, Y. Sun, S. Wu, Z. Jia, X. Lu, H. Yu, W. Chen, J. Zhu, G. Xie, R. Yang, D. Shi, X. Xu, J. Xiang, K. Liu, G. Zhang. Observation of strong interlayer coupling in MoS_2/WS_2 heterostructures. *Advanced Materials* 28, 1950-1956 (2016).

[58] K. Kośmider, J. Fernández-Rossier. Electronic properties of the MoS_2-WS_2 heterojunction. *Physical Review B* 87, 75451 (2013).

[59] X. Hong, J. Kim, S.-F. Shi, Y. Zhang, C. Jin, Y. Sun, S. Tongay, J. Wu, Y. Zhang, F. Wang. Ultrafast charge transfer in atomically thin MoS_2/WS_2 heterostructures. *Nature Nanotechnology* 9, 682-686 (2014).

[60] Y. Yu, S. Hu, L. Su, L. Huang, Y. Liu, Z. Jin, A. A. Purezky, D. B. Geohegan, K. Kim, Y. Zhang, L. Cao. Equally efficient interlayer exciton relaxation and improved absorption in epitaxial and nonepitaxial MoS_2/WS_2 heterostructures. *Nano Letters* 15, 486-491 (2015).

[61] M. M. Furchi, D. K. Polyushkin, A. Pospischil, T. Mueller. Mechanisms of photoconductivity in atomically thin MoS_2. *Nano Letters* 14, 6165-6170 (2014).

[62] D. J. Late, B. Liu, R. Matte, V. P. Dravid, C. N. R. Rao. Hysteresis in single-layer MoS_2 field effect transistors. *ACS Nano* 6, 5635-5641 (2012).

4. Synthesis of MoS_2/WS_2 lateral heterostructures and alloys

4.1. Introduction

Recent developments in TMDC heterostructures as well as homostructures of TMDC monolayers have led to important advances in our understanding of the physical properties, including efficient exciton dissociation and ultrafast charge transfer.[1-3] Many research groups have attempted to construct a variety of vertically-stacked TMDC heterostructures so as to fabricate next-generation devices by tapping into their unique properties.[4-9] However, as most vertical TMDC heterostructures have been commonly employed by stacking different monolayers via transfer techniques, the mismatch in the stacking angle between the monolayers[10] and contaminants at the interface[11-12] are thus unavoidable. Although epitaxial growth of a vertical heterostructure has been reported,[13-15] highly complicated fabrication techniques are still required to deposit the electrodes on both the top and bottom monolayers because of the insufficient space available on the monolayers themselves, thus limiting the wide applicability of vertical TMDC heterostructures.

Besides vertical TMDC heterostructures, a few different strategies for the epitaxial growth of lateral TMDC heterostructures with a one-dimensional (1D) interface have recently been proposed on the basis of one-step[15-17] and two-step[1,18-22] CVD synthesis procedures. Conceptually, two-step growth processes offer a more convenient approach to achieving controlled lateral heterostructures because each TMDC monolayer can be grown individually and sequentially under similar synthetic conditions. However, in the two-step growth process, the crystal edges (growth front) of the core layer can easily be contaminated because of the exposure to ambient conditions after the first growth process, which can induce a large number of defects near the interface.[18] Consequently, these defect sites can be energetically

reactivated and play a significant role in nucleating the precursors during the second growth step thus resulting in a change in the kinetics of the epitaxial growth process. As a result, the two-step growth procedure of lateral TMDC heterostructures usually results in a composition transition region at the interface[18], thicker outer-shell layers[18,22], and/or the nucleation on the top of the inner core crystal[1]. These phenomena have been observed much more prominently when the shell layer was synthesized at a higher temperature than the core layer because the defect sites become nucleation centers at high temperatures.[1]

In contrast, the one-step growth approach, which does not need to involve the exposure of the activated edges of the core layer to ambient conditions, is more favourable in creating lateral TMDC monolayer heterostructures with an atomically sharp interface. However, the complexity of simultaneously controlling the various precursors and growth parameters in the one-step synthesis makes it difficult to achieve the uniformity and reproducibility. In addition, the one-step growth process can suffer from precursor mixing during the growth steps and hence the formation of undesirable alloyed structures at the interface.[23-24] Even though some strategies, such as loading precursors into quartz boats facing down[17] and adding a metal catalyst to lower the growth temperature,[15] have been suggested to avoid the interference of two vaporized precursors, it still remains a challenge to synthesize lateral TMDC heterostructures with a clear interface and a large crystal size.

In this chapter, I demonstrate a facile one-step CVD process for the compositionally-controlled monolayer growth of lateral core/shell (MoS_2/WS_2, MoS_2/alloy, and alloy/WS_2) heterostructures and $Mo_{1-x}W_xS_2$ alloys using a solution-processed precursor deposition technique so as to precisely control the introduction timing and the supersaturation level of all the precursors. With this growth strategy, the metal oxide precursors can be vaporized separately or simultaneously in order to synthesize various types of heterostructures and alloys. Furthermore, the crystal size for the heterostructures is found to increase up to 160 μm, which

is the largest amongst the reported lateral TMDC heterostructured crystals. The lateral heterostructures are clearly verified by Raman and PL spectra as well as transmission electron microscopy (TEM). Compared to the two-step growth, the MoS_2/WS_2 heterostructures grown by the one-step procedure have a relatively clear interface. In addition, alloyed structures are intentionally obtained in the core or the shell regions of the lateral heterostructures or over the entire region of the monolayer by controlling the relative vaporized amounts of precursors and growth temperatures. Finally, it is found that bound excitons are observed in the alloyed regions at low temperatures because of trapped sites caused by randomly distributed Mo and W atoms. The growth strategies presented herein can be applied to other TMDC heterostructures and can provide a number of opportunities for the development of new kinds of electronic and optoelectronic devices.

4.2. Controlled growth of TMDC monolayer heterostructures and alloys

Figure 4-1a,b illustrates the growth procedure of the TMDC heterostructured or alloyed monolayers. As previously discussed in earlier chapters, the solution-processed approach makes it possible to deposit an extremely small amount of transition metal oxide precursor onto the SiO_2 substrates to induce a low supersaturation level during the growth process, which in turn leads to the growth of large-sized and highly crystalline TMDC monolayers and the fast and complete consummation of the precursors within a short time frame. This is a crucial point for the successful production of lateral heterostructured or alloyed monolayers without any additional undesirable nucleation and growth. To apply this strategy to the growth of the TMDC monolayer heterostructures and alloys, a MoO_3 solution in ammonium hydroxide (NH_4OH) was spincoated or dropped onto the bottom SiO_2 substrate. The weight of the deposited MoO_3 film was found to be significantly small at around ~0.01 mg. For the sufficient

supply of tungsten, tungsten trioxide (WO_3) precursors were scattered directly onto the growth substrate using a solution made from dissolving WO_3 and sodium cholate together in NH_4OH. This is because the vapour concentration of the WO_3 powder is much lower than that of MoO_3 even at a high temperature of more than T = 950 °C. The heavy weight of the sodium cholate could make it possible to deposit the WO_3 in the form of particles, and its carbon ring structure plays an important role in nucleating TMDC monolayers rather easily.[25] After the deposition of the precursor, the substrates that consist of a MoO_3 film and WO_3 particles were loaded onto the bottom and the top of the crucible in a furnace, respectively, as shown in Figure 4-1b.

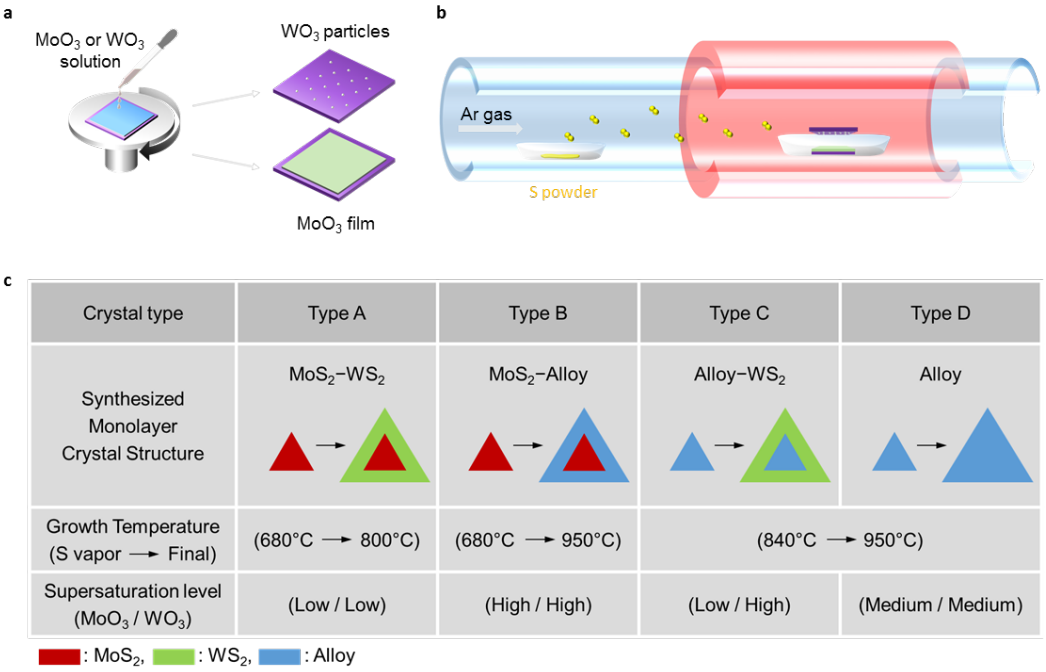

Figure 4-1. Schematic of the lateral growth process of MoS_2/WS_2 heterostructures and alloys. a) Solution-processed precursor deposition. The MoO_3 film was deposited by a MoO_3 solution in NH_4OH while the WO_3 particles were scattered by using a WO_3/sodium cholate solution in NH_4OH. b) Illustration of the synthesis process for the heterostructures and alloys. c) Conditions for each monolayer structures. To induce low, medium and high supersaturation levels of MoO_3, 20, 50 and 100 mg/ml MoO_3 solutions were used, respectively. To induce low, medium and high supersaturation levels of WO_3, 16, 40 and 80 mg/ml WO_3 solutions were used, respectively.

The one-step CVD growth procedure at atmospheric pressure employs three main parameters to synthesize the various TMDC monolayer heterostructures and alloys by decoupling and coupling the MoS_2 and the WS_2 growth processes: (1) the sulfur vaporization temperature, (2) the subsequent growth temperature, and (3) the relative supersaturation level of MoO_3 and WO_3 during the synthesis. The four main types of monolayer structures laterally grown using the approach developed in this work are summarized in Figure 4-1c: MoS_2/WS_2 heterostructures (Type A), MoS_2/alloy heterostructures (Type B), alloy/WS_2 heterostructures (Type C), and alloy monolayer structures (Type D). The effect of different parameters on the growth behaviour were carefully studied and compared as shown in Figure 4-2. From these results, the role of each parameter can be determined as follows, which will also be explained in further detail later in this chapter:

(1) The sulfur vapour introduction temperature determines whether the core structure will be grown as a single MoS_2 monolayer or a $Mo_{1-x}W_xS_2$ alloy. At a relatively low temperature (T ~ 680 °C), a single MoS_2 monolayer is formed inside (Type A & B) because the vaporization and sulfurization of WO_3 rarely occurs at such comparatively low temperatures due to the relatively high vaporization temperature of WO_3. However, if the sulfur vaporization begins at a high temperature (T ~ 840 °C), then MoO_3 and WO_3 will be vaporized and reacted with the vapour-phase sulfur simultaneously to yield an alloy-type monolayer in the core (Type C & D);

(2) The subsequent growth for lateral epitaxial growth continuously over the existing core crystal edges is mainly implemented at a relatively high temperature (T~950 °C) so as to facilitate the vaporization of WO_3 from the middle to the final growth phase (Type B, C & D). It is worth noting that the final growth temperature was kept as low as possible when synthesizing a clear MoS_2/WS_2 heterostructure (Type A). If the final growth temperature is increased, a narrow MoS_2/WS_2 alloy band is frequently found at the interface of the

heterostructure because MoO_3 can be vaporized violently at a high temperature and coexist with WO_3 precursors in the vapour phases until it is completely consumed (Structure no. 5 & 6 in Figure 4-2, and Figure 4-3).

(3) The supersaturation level associated with the vapour concentration and pressure of the precursors is the determining factor in producing the desired heterostructure. The low supersaturation level of MoO_3 was used to grow the second WS_2 material at the edge of the first core crystal by avoiding the undesired alloyed formation at the interface or in the shell layer of the heterostructure (Type A & C). The high supersaturation level of WO_3 was usually employed to promote the formation of an alloy in the shell layer by maintaining a high vapour concentration of WO_3 (Type B & C). Also, note that the low supersaturation level of WO_3 was used to grow in-plane lateral MoS_2/WS_2 heterostructures, whereas vertical heterostructures were frequently found together with lateral heterostructures when applying a high supersaturation level of WO_3 (Structure no. 1 in Figure 4-2, and Figure 4-4). Finally, it has shown that the stoichiometry in the $Mo_{1-x}W_xS_2$ alloy monolayers (Type D) can be easily controlled by adjusting the supersaturation level of MoO_3 and WO_3.

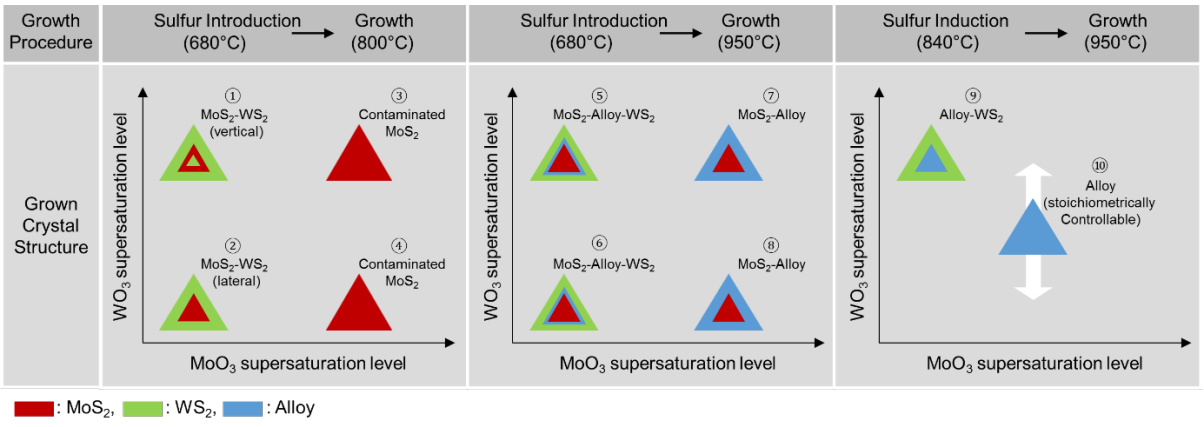

Figure 4-2. Synthesized heterostructured and alloyed monolayers with various growth parameters. The results were obtained by controlling the four growth parameters: (1) sulfur introduction temperature, (2) final growth temperature, (3) supersaturation level of MoO_3, and (4) supersaturation level of WO_3.

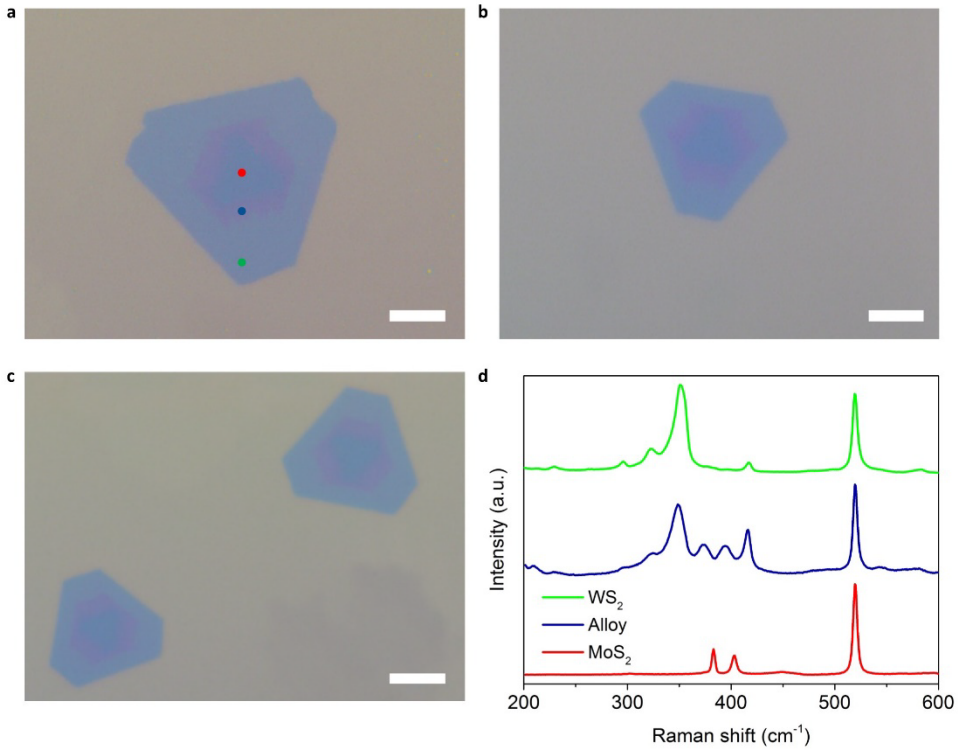

Figure 4-3. MoS_2/alloy/WS_2 lateral heterostructures grown at a high growth temperature. a-c) When the final growth temperature is increased, compared to the MoS_2/WS_2 heterostructures, the alloyed region between the MoS_2 and the WS_2 monolayers is clearly observed. All scale bars: 20 μm. d) Raman spectra collected from the points marked in (a).

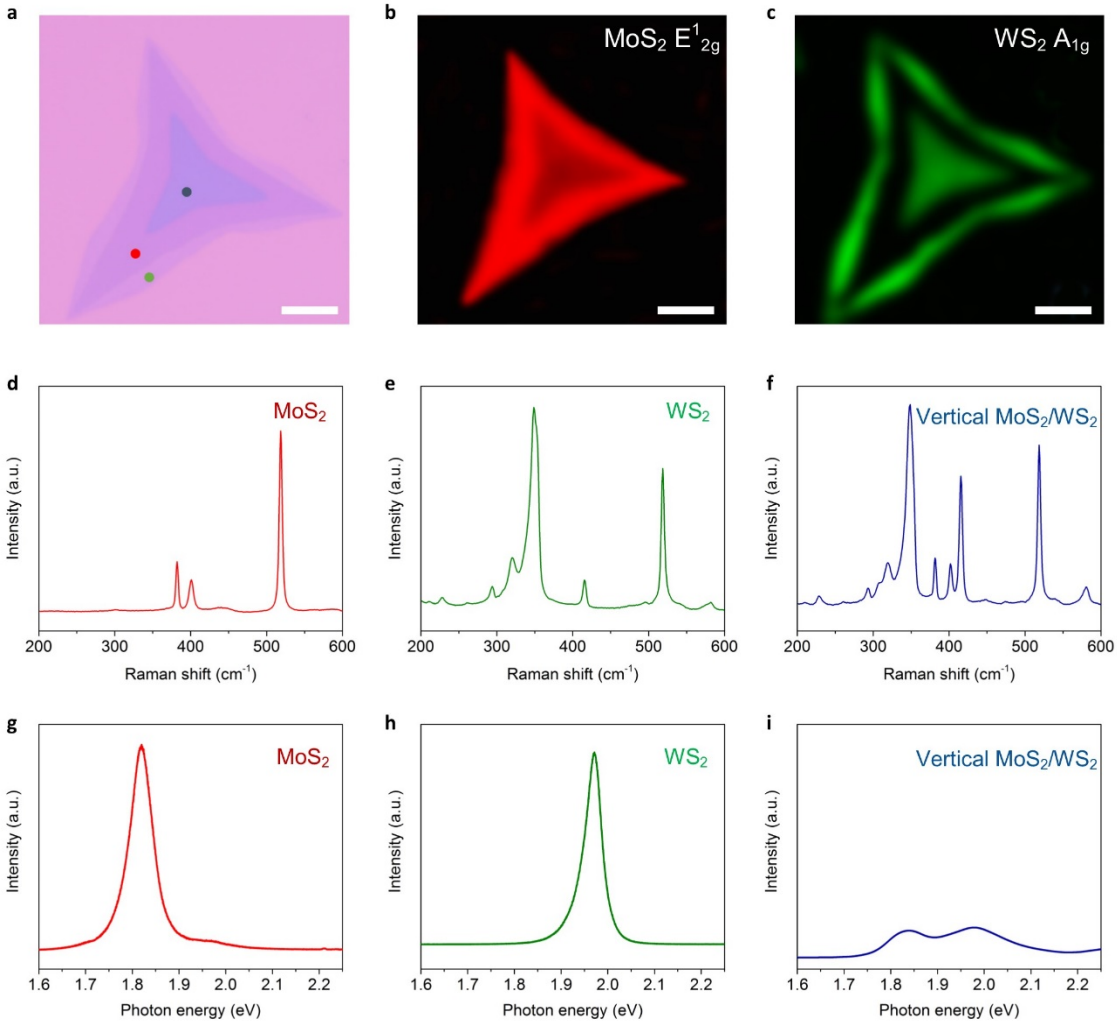

Figure 4-4. MoS_2/WS_2 vertical heterostructures. a) Optical image of the vertical MoS_2/WS_2 heterostructure. When the amount of WS_2 was increased, vertical heterostructures were grown along with lateral heterostructures. b-c) Raman mapping of the E^1_{2g} peak of MoS_2 and the A_{1g} peak of WS_2. All scale bars: 20 μm. d-f) Raman spectrum collected from the points marked in (a). g-i) PL spectrum collected from the points marked in (a).

4.3. MoS_2/WS_2 monolayer heterostructures

4.3.1. Heterostructures with a clear interface

Figure 4-5a shows that large MoS_2/WS_2 lateral heterostructured crystals were grown on the SiO_2 substrates. It was confirmed that the MoS_2 monolayer was grown first at a relatively low temperature and then the WS_2 monolayers started to grow laterally from the edge of the MoS_2 monolayers. The shape of the synthesized WS_2 monolayers tended to follow that of the MoS_2 monolayer, which is very similar to that found on other parts of the growth substrate (Figure 4-6). The sizes of the heterostructures were much larger than that of previously reported heterostructures and the size of the triangular crystals reached up to 160 μm (Figure 4-5b). The MoS_2 and WS_2 regions could be clearly discerned in a single triangular domain due to the optical contrast difference between them (Figure 4-5c). The MoS_2/WS_2 heterostructures were further examined by Raman and PL spectra (Figure 4-5d,e). The Raman and PL spectra of the MoS_2 and WS_2 monolayers were obtained from the points marked as red and green dots in Figure 4-5c, respectively. The 2LA(M) resonance peak and the A_{1g} peak of the WS_2 monolayer were clearly seen at around 349 cm^{-1} and 417 cm^{-1} in the shell region, respectively, while the MoS_2 monolayer in the core region exhibited two characteristic Raman peaks at around 382 cm^{-1} and 401 cm^{-1}, corresponding to the E^1_{2g} mode and the A_{1g} mode, respectively. Similarly, two distinctive peaks at 1.83 eV and 1.97 eV were found in the PL spectra, which corresponds to the emission from the MoS_2 and WS_2 monolayers, respectively.

To further verify the spatial distributions of the lateral heterostructures, the Raman and PL mapping images (Figure 4-5f-i) were taken from the crystal in Figure 4-5b. These mapping images clearly show that the MoS_2 monolayer in the core region interconnected seamlessly with the WS_2 domain in the outer region. The transition graph of the PL spectra collected at the interface of the heterostructure (marked as a white dotted line in Figure 4-5c) also demonstrates that the MoS_2 and WS_2 regions were clearly separated, and the intermediate state peak, which might have originated from alloyed structures at the interface, was not observed at the interface as shown in Figure 4-5j. The formation of the clear interface was further confirmed using an atomic resolution Z-contrast scanning transmission electron microscope (STEM) image (Figure 4-5k).

The clear interface and the large sizes of the heterostructures that have been obtained, especially for Type A in Figure 4-1c, can be explained by considering in more depth the growth strategy. In the growth procedure outlined herein, an extremely small amount of MoO_3 was deposited using a solution-processed precursor deposition technique. As a result, the supersaturation level of MoO_3 becomes rather low during the growth of the first inner MoS_2 crystal causing the nucleation density to decrease dramatically, which in turn increases the size of the synthesized crystal as shown in Chapter 3. In addition, the interference from vaporized MoO_3 molecules was dramatically suppressed during the subsequent growth of the WS_2 monolayer because the growth of the MoS_2 monolayers can usually be completed within a short timescale (< 5 minutes) at the early stages of the growth process due to the extremely small amount of MoO_3 precursor (~0.01 mg), resulting in a MoS_2/WS_2 lateral heterostructure with a sharp 1D interface.

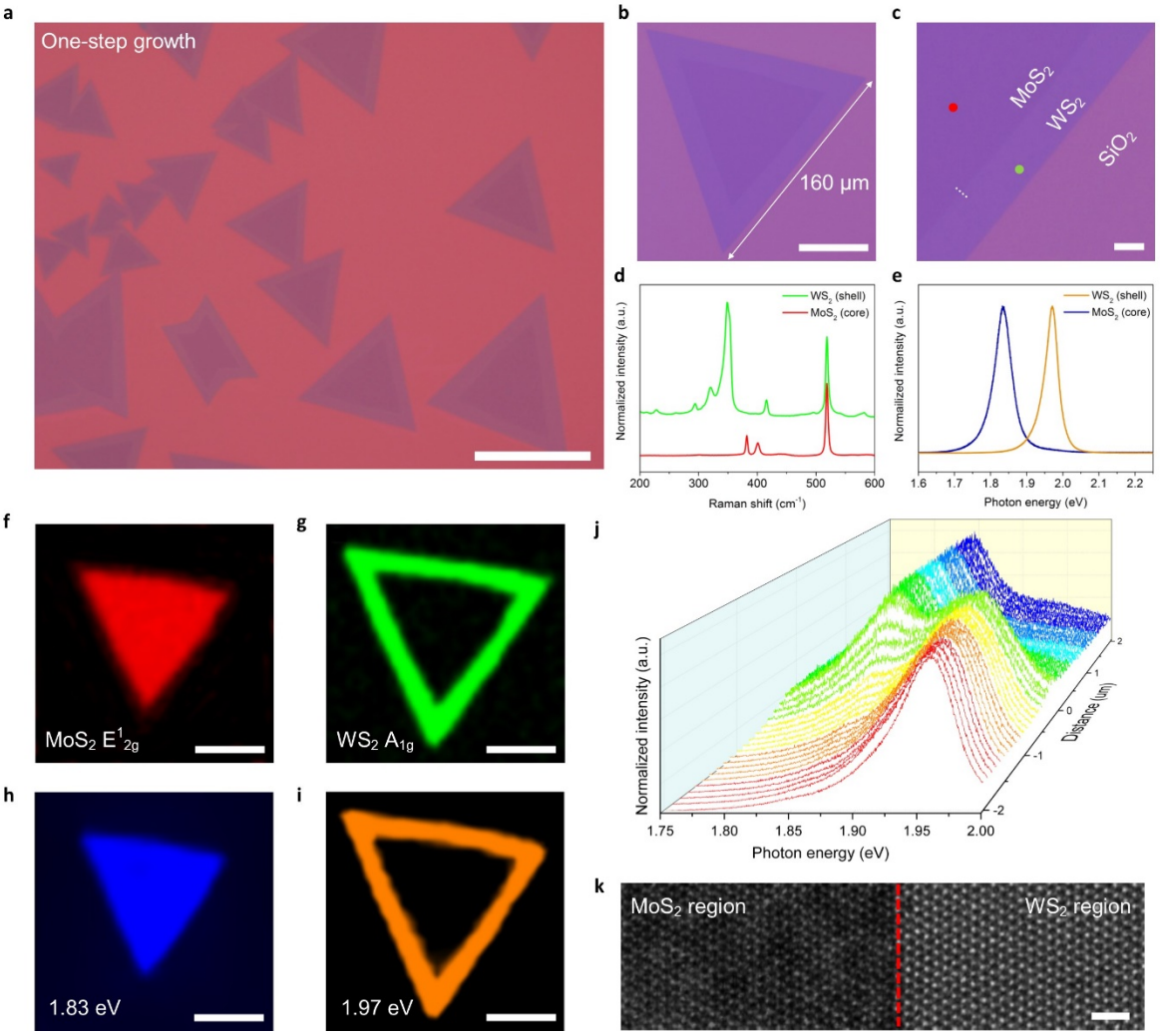

Figure 4-5. MoS_2/WS_2 lateral heterostructures grown by a one-step process. a) Optical image of the MoS_2/WS_2 heterostructure. Scale bar: 100 μm. b) Optical image of a large-sized MoS_2/WS_2 heterostructure. Scale bar: 50 μm. c) Enlarged optical image of the interface between the MoS_2 and the WS_2 monolayers. Scale bar: 10 μm. d-e) Raman and PL spectrum collected from the core and the shell regions. f-g) Raman mapping images of the E^1_{2g} peak of MoS_2 and the A_{1g} peak of WS_2. h-i) PL mapping images of the MoS_2 and the WS_2 emission energy. Scale bar: 50 μm. j) PL transition at the interface of the heterostructure marked with white dots in (c). k) STEM image of the interface of the heterostructure. Scale bar: 1 nm.

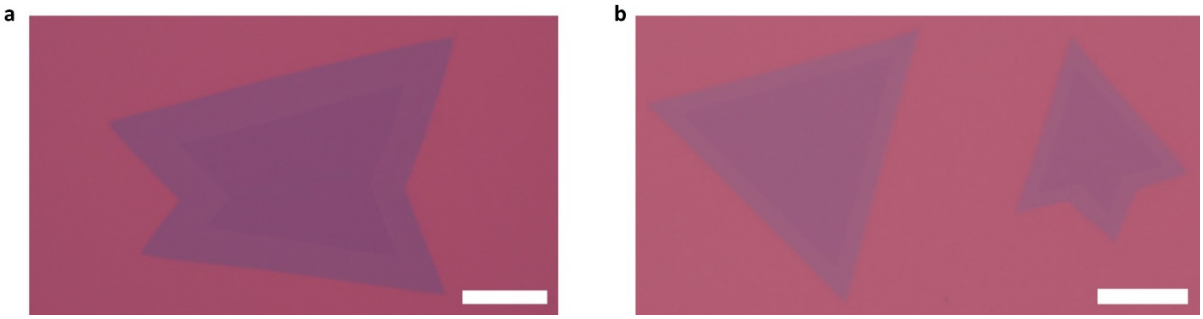

Figure 4-6. Shape of the lateral MoS_2/WS_2 heterostructures. a-b) The shape of the outer WS_2 monolayer follows that of the MoS_2 monolayer in the core region. All scale bars: 20 μm.

4.3.2. Comparison with other growth strategies

Some strategies based on a one-step growth process have already been reported in previous studies. For example, K. Chen *et al*[17] suggested to load precursors in quartz boats facing down to avoid the interference of two vaporized precursors ($(NH_4)_6Mo_7O_{24}$, $(NH_4)_{10}W_{12}O_{41}$) at a high temperature. Although MoS_2/WS_2 monolayers were grown on the substrates, a large number of particles or additional nucleation sites were found on the monolayers because vaporized precursors at high temperatures could not be eliminated completely during the growth stage. Y. Gong *et al*[15] also introduced a metal catalyst (tellurium) to lower the growth temperature down to 650 °C to vaporize MoO_3 and W powders sequentially. However, it seemed that the alloyed regions were also found at the interface between the MoS_2 and WS_2 monolayers because the mixture of two vaporized precursors is unavoidable. The solution-processed precursor deposition introduced in Chapter 4.2 can remove these issues clearly as deposited MoO_3 is completely vaporized before WO_3 becomes involved in the growth process.

In addition, to provide further insight into the direct one-step growth process in the formation of high-quality in-plane heterostructures, a two-step growth procedure of lateral MoS_2/WS_2 heterostructures was conducted (Figure 4-7). The growth of the MoS_2 monolayer was followed by the growth of the WS_2 monolayer sequentially under similar synthetic conditions. Interestingly, unlike a one-step growth process, the intermediate state peak was clearly observed in the PL spectrum in the crystal grown using the two-step growth procedure. PL mapping and spectra show that the intermediate peak was located at 1.91 eV at the interface between the MoS_2 and the WS_2 monolayers (Figure 4-7d). This compositional transition region at the interface might be attributed to defect sites generated at the edge of the inner layer when the layer was exposed to the ambient environment before the growth of the shell layer, as reported in previous studies[18]. As a result, a large number of defect sites could result in the change in the nucleation and lateral growth kinetics for the subsequent epitaxial heterostructure growth process. The possibility of the presence of MoO_3 precursors during the second step for WS_2 was excluded because different quartz tubes were used for each of the MoS_2 and WS_2 monolayer growth processes. In addition, the diffusion-mediated synthesis at relatively high temperatures might be another factor causing the formation of the transition region.[21]

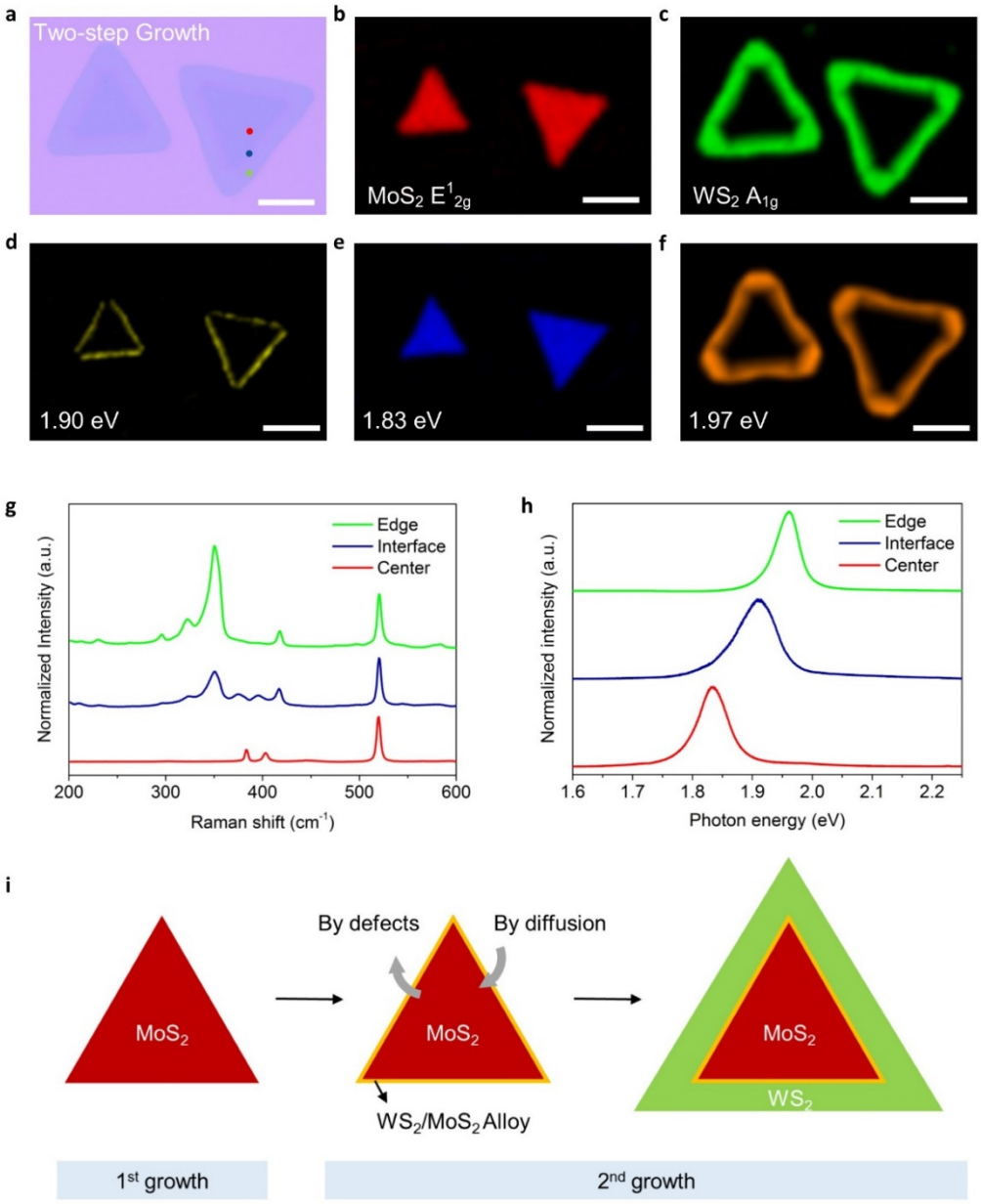

Figure 4-7. MoS_2/WS_2 lateral heterostructures grown by a two-step process. a) Optical image. b-c) Raman mapping images. d-f) PL mapping images. All scale bars: 20 μm. g-h) The individual Raman and PL spectra also show that an alloyed intermediate region was formed. i) It is suggested that defect sites at the edge of the inner layer or the diffusion of WS_2 into MoS_2 during the second growth step might cause the formation of an alloyed structure at the interface.

4.4. MoS_2/Alloy monolayer heterostructures

As shown in Figure 4-1, the composition of the core and the shell layers in the heterostructures can be adjusted by controlling the growth parameters. For the MoS_2/alloy lateral heterostructure, the final growth temperature and the amount of MoO_3 deposited were increased to T = 950 °C and 0.1 mg, respectively, to keep the vapour concentration of MoO_3 high throughout until the outer shell layer had formed. As a result, a $Mo_{1-x}W_xS_2$ alloyed monolayer was formed in the outer shell (Figure 4-8a,b). Although the optical contrast is weaker than that observed for the MoS_2/WS_2 heterostructured monolayer, the alloyed region in the shell could be distinguished from the MoS_2 monolayer area in the core. The Raman spectra of the MoS_2/alloy heterostructure show that the corresponding peaks of the MoS_2 and the WS_2 monolayers were observed simultaneously at the outer shell, indicating the formation of an alloyed layer, while only MoS_2 monolayer peaks were found in the core region (Figure 4-8c). One of the interesting features in the Raman spectra is that the E^1_{2g} and the A_{1g} peaks of MoS_2 in the alloyed region are shifted towards lower wavenumbers. This phenomenon has already been observed in the MoS_2/WS_2 lateral heterostructures grown by a two-step process (Figure 4-7g). It is known that either the downshift or the upshift of both Raman modes are associated with either tensile or compressive strains, respectively.[26-28] Therefore, this behaviour is likely to result from localized strain and disorder in an alloy of two domains with different lattice constants. It is further observed that the E^1_{2g} and the A_{1g} peaks of MoS_2 and the 2LA(M) peak of WS_2 in the alloyed outer shell became much weaker and broader than those typically observed for WS_2 monolayers because of less organized structures in the alloy.

The PL spectra in Figure 4-8d also demonstrate that the emission energy level of the outer shell (1.87 eV) was found to be within the range between those of the MoS_2 and the WS_2 monolayers, revealing the formation of an alloy heterostructure. The uniformity of the core and the outer shell was confirmed by Raman and PL mapping images (Figure 4-8e). The stoichiometric composition ratio of the outer shell was calculated using the equation,

$$E_{Mo_{1-x}W_xS_2} = (1-x)E_{MoS_2} + xE_{WS_2} - bx(1-x) \quad (4.1)$$

where $E_{Mo_{1-x}W_xS_2}$, E_{MoS_2}, and E_{WS_2} are the band gaps of the alloy, MoS_2, and WS_2 monolayer, respectively, and b is the bowing constant. A bowing constant, b, is introduced because the band gap of an alloy sometimes does not lies between the band gaps of MoS_2 and WS_2 at certain composition ratios (x). This bowing effect has already been observed in other reports on $Mo_{1-x}W_xS_2$ alloys[29] as well as many bulk semiconductor alloys.[30-31] Before identifying the stoichiometric composition ratio (x), it is needed to find the bowing constant (b) for the alloy. As a bowing parameter for $Mo_{1-x}W_xS_2$ alloys has already been estimated from the reported study,[29] which was performed for alloyed structures with a variety of different stoichiometric compositions, the same value for b (0.25) is used here to approximately determine the stoichiometric composition ratio in this case with the assumption that the alloyed region is uniform. Finally, the stoichiometric composition ratio for the alloyed region in Figure 4-8 is found to be $x = 0.3$, which shows that an $Mo_{0.7}W_{0.3}S_2$ monolayer was formed in the shell layer.

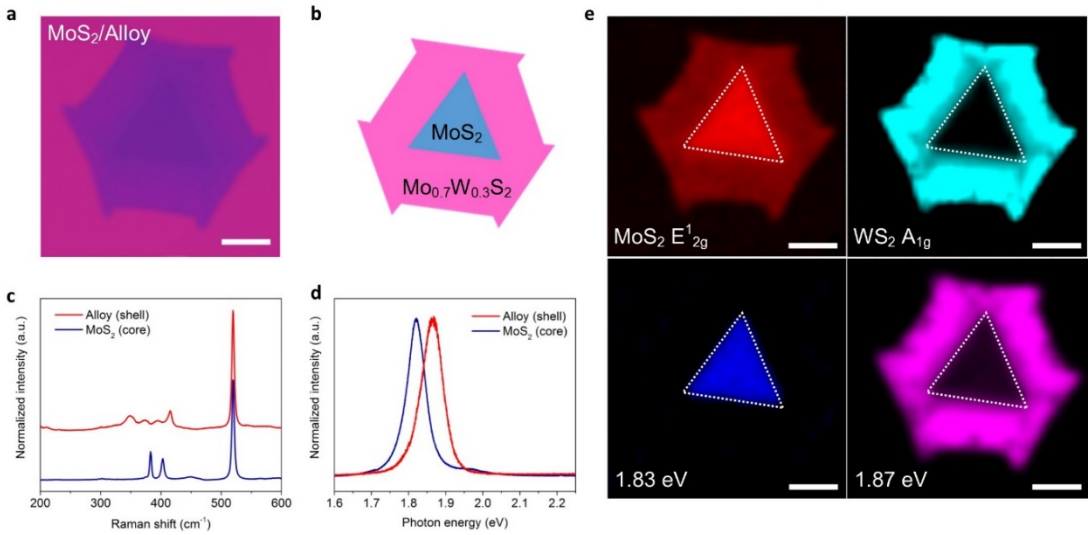

Figure 4-8. MoS_2/Alloy lateral heterostructures. a) Optical image of the MoS_2/Alloy heterostructure monolayer. The contrast of the image was adjusted to show the core and the outer region clearly. b) Schematic of the synthesized MoS_2/Alloy heterostructure monolayer. c-d) Raman and PL spectrum collected from the core and the shell layers. e) Raman and PL mapping images. All scale bars: 20 μm.

4.5. Alloy/WS_2 monolayer heterostructures

Using the lateral epitaxial growth strategy, the growth parameters can be tailored so as to synthesize an in-plane heterostructure consisting of an alloyed structure in the core and a WS_2-only monolayer in the outer shell as shown in Figure 4-9a,b. To first form an alloyed layer as the core of the lateral heterostructure, the sulfur vaporization was started at a much higher temperature (T = 840 °C) than that used for the growth of the MoS_2/WS_2 heterostructure in Figure 4-5. In addition, the relatively large amount of WO_3 was loaded while the small amount of MoO_3, similar to that used for the MoS_2/WS_2 heterostructure growth process, was loaded in order to avoid any unwanted alloy reaction during the subsequent epitaxial growth of the outer WS_2 shell. The growth temperature was increased to 950 °C to facilitate the vaporization of WO_3 for the shell region.

The Raman spectrum showed that both the MoS_2 and the WS_2 monolayer peaks were found in the core region, and only the WS_2 monolayer peaks were observed in the shell area (Figure 4-9c), confirming that alloy/WS_2 lateral heterostructures were formed. It was found that the PL spectrum of the alloyed structure in the core region was red-shifted slightly from 1.97 eV to 1.94 eV and was much broader compared to that of the WS_2 monolayer in the shell region (Figure 4-9d). Here, the stoichiometric composition ratio was found to be x = 0.9, according to Equation (4.1). The Raman and PL mapping images clearly show that the alloy core region and the pure WS_2 shell region are separated (Figure 4-9e). These findings demonstrate that sulfurization at a relatively high temperature (> 840 °C) can provide a way to synthesize an alloyed structure in the core region due to the vaporization of two precursors at the same time.

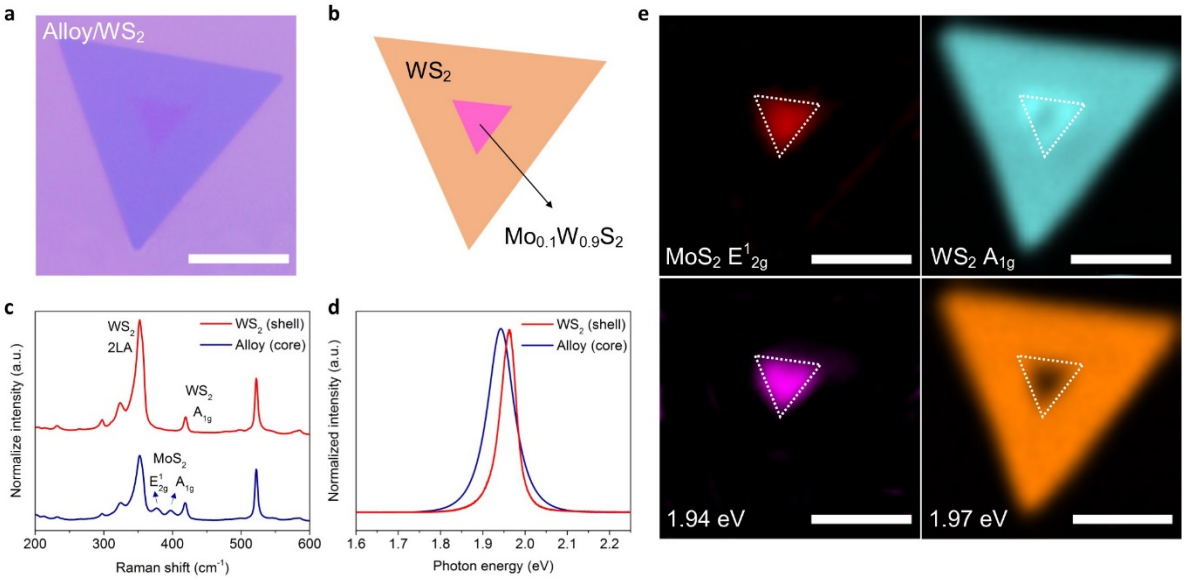

Figure 4-9. Alloy/WS_2 lateral heterostructures. a) Optical image of the Alloy/WS_2 heterostructure monolayer. The contrast of the image was adjusted to show the core and the outer regions clearly. b) Schematic of the synthesized Alloy/WS_2 heterostructure monolayer. c-d) Raman and PL spectrum collected from the core and the shell layers. e) Raman and PL mapping images. All scale bars: 50 μm.

4.6. $Mo_{1-x}W_xS_2$ monolayer alloys

Finally, results are presented that demonstrate that it is possible to produce well-organized alloyed monolayers by controlling the relative amount of MoO_3 and WO_3 and using a high sulfur vaporization temperature (T ~ 840 °C) and a high growth temperature (T = 950 °C). Figure 4-10a shows the resulting $Mo_{1-x}W_xS_2$ alloy monolayer grown laterally on the SiO_2 substrate. The PL intensity and position mapping images in Figure 4-10b,c demonstrate that the chemical composition and structural characteristics are uniform over the monolayer crystal. The emission energy of the alloy monolayer was 1.90 eV, which is located almost at the centre of those of the MoS_2 and the WS_2 monolayers. The individual Raman spectra collected from the different areas of the alloy structure in Figure 4-10a exhibited almost the same profile,

indicating the uniformity of the alloyed monolayer structure (Figure 4-10d). In addition, there was no significant difference in the position and the intensity of PL spectrum (Figure 4-10e). The composition ratio of the alloy monolayer could be easily controlled by adjusting the relative ratio of the amount of the MoO_3 and WO_3, thus it was possible to obtain alloy monolayers with controlled energy band gaps. The emission energy level was close to that of the MoS_2 monolayer when the relative amount of MoO_3 was large, and vice-versa (Figure 4-10f).

To investigate the excitonic properties of the $Mo_{1-x}W_xS_2$ alloy monolayer, the temperature-dependent PL measurements were carried out as shown in Figure 4-10g. At a temperature below T = 100 K, an additional emission peak at around 1.85 eV was noticeable, and this peak became strongly dominant at 4.4 K. As the position of the newly emerged peak was stable with various excitation powers at 4.4 K and has a broad width, it was thought to be related to bound excitons, compared to free excitons located at a higher energy level (Figure 4-11). This shows that there are a number of binding sites in the alloy monolayer because the Mo and W atoms are randomly distributed and mixed together in the crystal, which may be the reason why the bound excitons were observed only at low temperatures. The Varshni equation[32], $E_g(T) = E_g(0) - aT^2/(T + b)$, was used to describe the band gap reduction with temperature. The transition of the free exciton was in good agreement with the Varshni equation, with $E_g(0)$ = 1.943 eV, a = 4.1 x 10^{-4} eV K^{-1}, and b = 406 K. However, the bound exciton exhibited a transition point at around 75 K. When the temperature increased above 4.4 K, the bound excitons can be thermally activated into the free state, thus the peak position is expected to be red-shifted. With a further increase of the temperature above 75 K, non-radiative decay can have a significant effect on the emission process and can decrease the decay time. These carriers recombine before they reach the lowest energy level in the conduction band, which leads to a blue-shift in the PL spectrum.[33] A dramatic increase in the full-width-half-

maximum (FWHM) of the bound exciton at around 75 K was also observed, while it remained almost constant below 50 K. In contrast, the FWHM of the free exciton increased gradually with increasing temperature, similar to those of typical semiconductors. These findings indicate that the emission behaviour of the alloy monolayer structure can be significantly affected by the inhomogeneities and the binding sites in the crystal.

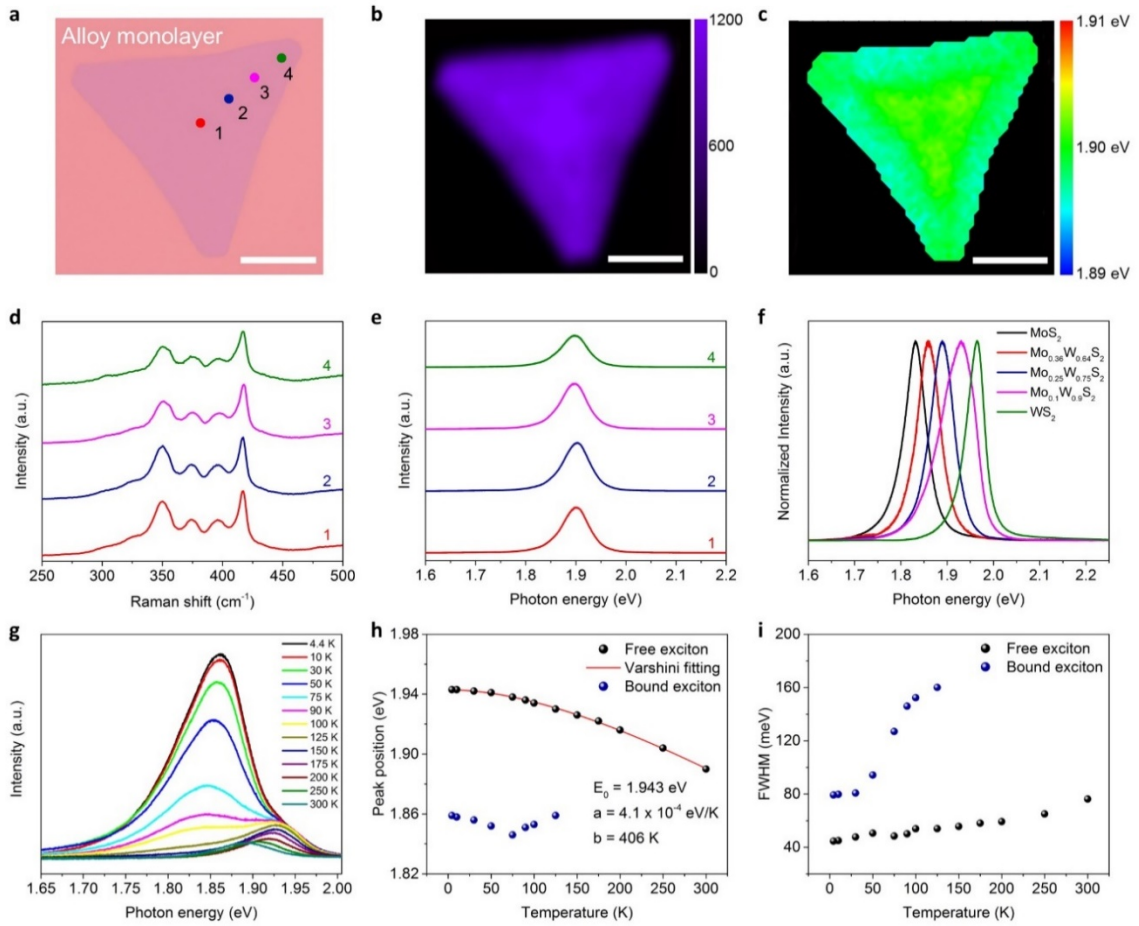

Figure 4-10. $Mo_{1-x}W_xS_2$ alloy monolayers. a) Optical image of the $Mo_{1-x}W_xS_2$ alloy monolayer. b) PL intensity mapping image at 1.90 eV. c) PL position mapping image. All scale bars: 20 μm. d-e) Raman and PL spectrum collected from the marked points in (a). f) PL spectrum of the composition ratio-controlled alloy monolayers. g) Temperature-dependent PL spectrum of the alloy monolayer. h) Peak position of the free excitons and the bound excitons as a function of temperature. i) FWHM of the free excitons and the bound excitons as a function of temperature.

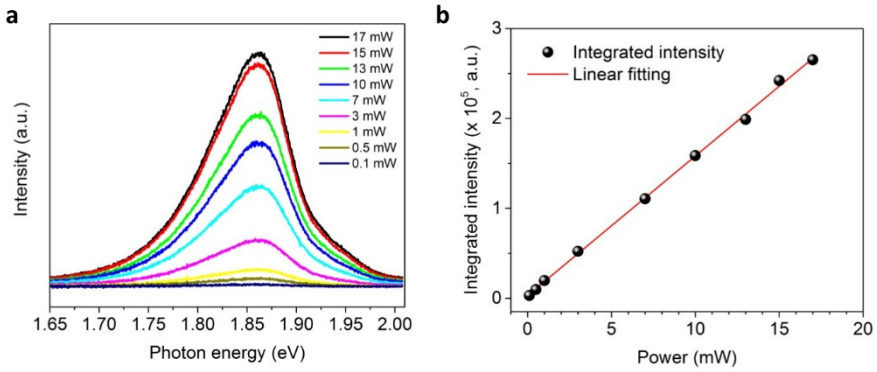

Figure 4-11. Dependence of the PL spectrum of the $Mo_{1-x}W_xS_2$ alloyed monolayer on the light intensity. a) PL spectrum increases with light intensity. b) The integrated PL intensity increases linearly with the light source.

4.7. Conclusions

In conclusion, large-sized lateral MoS_2/WS_2 heterostructured monolayers with a clear interface have been synthesized directly on SiO_2 substrates by controlling the amount of metal oxide precursors via a solution-processed precursor deposition technique. The extremely small amount of precursor can reduce its effect during the growth process of the shell layer, which makes it possible to synthesize MoS_2/WS_2 heterostructures with a large size up to 160 μm. In addition, lateral MoS_2/alloy and alloy/WS_2 heterostructures have been readily obtained by controlling parameters such as the temperature at which sulfur is introduced, the final growth temperature, and the supersaturation level of MoO_3 and WO_3. Finally, uniform $Mo_{1-x}W_xS_2$ alloy monolayers could also be synthesized with moderate amounts of precursors, and bound excitons have been found to emerge at a low temperature and become strongly dominant below 50 K due to trapped sites that arise from the random mixture of different transition metals. The current findings discussed in Chapter 3 and 4 can be of significant importance in the utilization of TMDC monolayers for new innovations in electronic and optoelectronic devices.

4.8. References

[1] H. Heo, J. Sung, G. Jin, J. H. Ahn, K. Kim, M. J. Lee, S. Cha, H. Choi, M. H. Jo. Rotation-misfit-free heteroepitaxial stacking and stitching growth of hexagonal transition-metal dichalcogenide monolayers by nucleation kinetics controls. *Advanced Materials* 27, 3803-3810 (2015).

[2] J. Shi, R. Tong, X. Zhou, Y. Gong, Z. Zhang, Q. Ji, Y. Zhang, Q. Fang, L. Gu, X. Wang, Z. Liu, Y. Zhang. Temperature-mediated selective growth of MoS_2/WS_2 and WS_2/MoS_2 vertical stacks on au foils for direct photocatalytic applications. *Advanced Materials* 28, 10664-10672 (2016).

[3] H. Chen, X. Wen, J. Zhang, T. Wu, Y. Gong, X. Zhang, J. Yuan, C. Yi, J. Lou, P. M. Ajayan, W. Zhuang, G. Zhang, J. Zheng. Ultrafast formation of interlayer hot excitons in atomically thin MoS_2/WS_2 heterostructures. *Nature Communications* 7, 12512 (2016).

[4] R. Cheng, D. Li, H. Zhou, C. Wang, A. Yin, S. Jiang, Y. Liu, Y. Chen, Y. Huang, X. Duan. Electroluminescence and photocurrent generation from atomically sharp WSe_2/MoS_2 heterojunction p-n diodes. *Nano Letters* 14, 5590-5597 (2014).

[5] C.-H. Lee, G.-H. Lee, A. M. van der Zande, W. Chen, Y. Li, M. Han, X. Cui, G. Arefe, C. Nuckolls, T. F. Heinz, J. Guo, J. Hone, P. Kim. Atomically thin p-n junctions with van der Waals heterointerfaces. *Nature Nanotechnology* 9, 676-681 (2014).

[6] M. M. Furchi, A. Pospischil, F. Libisch, J. Burgdörfer, T. Mueller. Photovoltaic effect in an electrically tunable van der Waals heterojunction. *Nano Letters* 14, 4785-4791 (2014).

[7] N. Choudhary, J. Park, J. Hwang, H.-S. Chung, K. H. Dumas, S. I. Khondaker, W. Choi, Y. Jung. Centimeter scale patterned growth of vertically stacked few layer only 2D MoS_2/WS_2 van der Waals heterostructure. *Scientific Reports* 6, 25456 (2016).

[8] Y. Xue, Y. Zhang, Y. Liu, H. Liu, J. Song, J. Sophia, J. Liu, Z. Xu, Q. Xu, Z. Wang, J. Zheng, Y. Liu, S. Li, Q. Bao. Scalable production of a few-layer MoS_2/WS_2 vertical heterojunction array and its application for photodetectors. *ACS Nano* 10, 573-580 (2015).

[9] J. M. Woods, Y. Jung, Y. Xie, W. Liu, Y. Liu, H. Wang, J. J. Cha. One-step synthesis of MoS_2/WS_2 layered heterostructures and catalytic activity of defective transition metal dichalcogenide films. *ACS Nano* 10, 2004-2009 (2016).

[10] P. K. Nayak, Y. Horbatenko, S. Ahn, G. Kim, J.-U. Lee, K. Y. Ma, A. R. Jang, H. Lim, D. Kim, S. Ryu, H. Cheong, N. Park, H. S. Shin. Probing evolution of twist-angle-dependent interlayer excitons in $MoSe_2/WSe_2$ van der Waals heterostructures. *ACS Nano* 11 (2017).

[11] X. Zhu, N. R. Monahan, Z. Gong, H. Zhu, K. W. Williams, C. A. Nelson. Charge transfer excitons at van der Waals interfaces. *Journal of the American Chemical Society* 137, 8313-8320 (2015).

[12] H. Li, J. Wu, X. Huang, Z. Yin, J. Liu, H. Zhang. A universal, rapid method for clean transfer of nanostructures onto various substrates. *ACS Nano* 8, 6563-6570 (2014).

[13] Y. Yu, S. Hu, L. Su, L. Huang, Y. Liu, Z. Jin, A. A. Purezky, D. B. Geohegan, K. Kim, Y. Zhang, L. Cao. Equally efficient interlayer exciton relaxation and improved absorption in epitaxial and nonepitaxial MoS_2/WS_2 heterostructures. *Nano Letters* 15, 486-491 (2015).

[14] Q. Zhang, X. Xiao, R. Zhao, D. Lv, G. Xu, Z. Lu, L. Sun, S. Lin, X. Gao, J. Zhou, C. Jin, F. Ding, L. Jiao. Two-dimensional layered heterostructures synthesized from core-shell nanowires. *Angewandte Chemie International Edition* 54, 8957-8960 (2015).

[15] Y. Gong, J. Lin, X. Wang, G. Shi, S. Lei, Z. Lin, X. Zou, G. Ye, R. Vajtai, B. I. Yakobson, H. Terrones, M. Terrones, B. Tay, J. Lou, S. T. Pantelides, Z. Liu, W. Zhou, P. M. Ajayan. Vertical and in-plane heterostructures from WS_2/MoS_2 monolayers. *Nature Materials* 13, 1135-1142 (2014).

[16] X.-Q. Zhang, C.-H. Lin, Y.-W. Tseng, K.-H. Huang, Y.-H. Lee. Synthesis of lateral heterostructures of semiconducting atomic layers. *Nano Letters* 15, 410-415 (2015).

[17] K. Chen, X. Wan, W. Xie, J. Wen, Z. Kang, X. Zeng, H. Chen, J. Xu. Lateral built-in potential of monolayer MoS_2-WS_2 in-plane heterostructures by a shortcut growth strategy. *Advanced Materials* 27, 6431-6437 (2015).

[18] K. Chen, X. Wan, J. Wen, W. Xie, Z. Kang, X. Zeng, H. Chen, J.-B. B. Xu. Electronic properties of MoS_2-WS_2 heterostructures synthesized with two-step lateral epitaxial strategy. *ACS Nano* 9, 9868-9876 (2015).

[19] Y. Yoo, Z. P. Degregorio, J. E. Johns. Seed crystal homogeneity controls lateral and vertical heteroepitaxy of monolayer MoS_2 and WS_2. *Journal of the American Chemical Society* 137, 14281-14287 (2015).

[20] X. Ling, Y. Lin, Q. Ma, Z. Wang, Y. Song, L. Yu, S. Huang, W. Fang, X. Zhang, A. L. Hsu, Y. Bie, Y. H. Lee, Y. Zhu, L. Wu, J. Li, P. Jarillo-Herrero, M. Dresselhaus, T. Palacios, J. Kong. Parallel stitching of 2D materials. *Advanced Materials* 28, 2322-2329 (2016).

[21] K. Bogaert, S. Liu, J. Chesin, D. Titow, S. Gradečak, S. Garaj. Diffusion-mediated synthesis of MoS_2/WS_2 lateral heterostructures. *Nano Letters* 16, 5129-5134 (2016).

[22] Y. Gong, S. Lei, G. Ye, B. Li, Y. He, K. Keyshar, X. Zhang, Q. Wang, J. Lou, Z. Liu, R. Vajtai, W. Zhou, P. M. Ajayan. Two-step growth of two-dimensional $WSe_2/MoSe_2$ heterostructures. *Nano Letters* 15, 6135-6141 (2015).

[23] C. Huang, S. Wu, A. M. Sanchez, J. J. P. Peters, R. Beanland, J. S. Ross, P. Rivera, W. Yao, D. H. Cobden, X. Xu. Lateral heterojunctions within monolayer $MoSe_2$-WSe2 semiconductors. *Nature Materials* 13, 1096-1101 (2014).

[24] X. Duan, C. Wang, J. C. Shaw, R. Cheng, Y. Chen, H. Li, X. Wu, Y. Tang, Q. Zhang, A. Pan, J. Jiang, R. Yu, Y. Huang, X. Duan. Lateral epitaxial growth of two-dimensional layered semiconductor heterojunctions. *Nature Nanotechnology* 9, 1024-1030 (2014).

[25] G. Han, N. J. Kybert, C. H. Naylor, B. Lee, J. Ping, J. Park, J. Kang, S. Lee, Y. Lee, R. Agarwal, C. A. T. Johnson. Seeded growth of highly crystalline molybdenum disulphide monolayers at controlled locations. *Nature Communications* 6, 6128 (2015).

[26] Y. Hui *et al.* Exceptional tunability of band energy in a compressively strained trilayer MoS_2 sheet. *ACS Nano* 7**,** 7126-7131 (2013).

[27] Y. Kobayashi, S. Mori, Y. Maniwa, Y. Miyata. Bandgap-tunable lateral and vertical heterostructures based on monolayer $Mo_{1-x}W_xS_2$ alloys. *Nano Research* 8, 3261-3271 (2015).

[28] M.-Y. Li *et al*. Epitaxial growth of a monolayer WSe_2-MoS_2 lateral p-n junction with an atomically sharp interface. Science 349, 524-528 (2015).

[29] Y. Chen, J. Xi, D. O. Dumcenco, Z. Liu, K. Suenaga, D. Wang, Z. Shuai, Y.-S. S. Huang, L. Xie. Tunable band gap photoluminescence from atomically thin transition-metal dichalcogenide alloys. *ACS Nano* 7, 4610-4616 (2013).

[30] S. Adachi. Properties of semiconductor alloys: Group-IV, III-V and II-VI semiconductors. Wiley: Chichester, U.K. (2009).

[31] W.-J. Yin, X.-G. Gong & S.-H. Wei. Origin of the unusually large band-gap bowing and the breakdown of the band-edge distribution rule in the Sn_xGe_{1-x} alloys. *Physical Review B* 78, 161203 (2008).

[32] Y. P. Varshni. Temperature dependence of the energy gap in semiconductors. *Physica* 34, 149-154 (1967).

[33] Y.-H. Cho, G. H. Gainer, A. J. Fischer, J. J. Song, S. Keller, U. K. Mishra, S. P. DenBaars. "S-shaped" temperature-dependent emission shift and carrier dynamics in InGaN/GaN multiple quantum wells. *Applied Physics Letters* 73, 1370-1372 (1998).

5. MoS_2 monolayer optical memory devices

5.1. Introduction

The attractive features of monolayer TMDCs, as investigated in previous chapters, make them a promising material for flexible and wearable electronic[1-4] and optoelectronic[5-7] devices. Various monolayer MoS_2-based photodetectors have been recently shown to exhibit outstanding optical properties with a high photoresponsivity.[8-13] However, the very large surface-to-volume ratio of the MoS_2 monolayer makes it particularly sensitive to the surrounding environment such as defects on the underlying substrates or physisorbed gas molecules, leading to electron trap sites that occur due to local potential fluctuations.[14-17] Consequently, charge trapping in photodetectors can play an important role in determining both the response times and the light intensity-dependent photoresponse.[8-9] Recent studies on electrical memory devices[18-21] have provided useful information about the modulation of the charge trapping density.

Compared with studies on photodetectors, relatively little research has been done to investigate the optoelectronic memory capability of devices using TMDC materials. Optoelectronic memory devices can provide a simpler approach in terms of device integration in image sensor circuitry compared with that of conventional image sensors containing a combination of photodetectors and electronic memory devices. Recently, several concepts for optoelectronic memory devices using an atomically thin film have been reported.[22-23] Along these lines, a hybrid structure with graphene on a multilayer MoS_2 flake showed considerable photoresponsive properties.[22] However, the dark current level was extremely high at around a few hundred μA due to the high electrical conductivity of graphene and hence the ON/OFF

current ratio was less than 2, which makes it difficult to clearly discern currents arising from dark and light conditions.

Mechanically exfoliated few-layered $CuIn_7Se_{11}$ optoelectronic memory structures, similar to a charge-coupled device (CCD), have also been reported[23]. In this case, the retention time was relatively short, on the order of 50 s, and the ON/OFF ratio was found to be less than 10 as a result of the relatively low photosensitivity of the material, making it unsuitable for high-quality image sensing devices. Monolayer photonic memory devices with acceptable performance for practical image sensing applications have not yet been demonstrated. This chapter presents MoS_2 monolayer optoelectronic memory devices based on charge trapping at the MoS_2/SiO_2 dielectric interface along with the subsequent optically-induced charge release, which allows for not only a high ON/OFF ratio with a linear response to the optical dose, but also a long retention time.

5.2. Surface treatment and device fabrication

Before the fabrication of the devices, the surface functionalization was conducted as follows. Silicon substrates with 300 nm of SiO_2 were used as the growth substrates. After cleaning the substrates, they were functionalized using an oxygen plasma treatment. These target substrates for growth were loaded upside down above a crucible in the 50-mm quartz tube of the CVD growth system, and the source substrates with an ultra-thin and homogeneous MoO_3 precursor film, which were prepared using diluted precursor solutions by spin-coating, were placed under the target substrates. Another crucible containing 200 mg of sulfur powder (Sigma Aldrich) was placed upstream at the edge of the tube. The CVD growth was conducted at atmospheric pressure with a continuous flow of pure argon gas, and the detailed growth recipe was: anneal at $T = 200°C$ for 20 minutes under 1,000 sccm flow of argon gas to remove oxygen and water

in the tube, ramp to T = 650 °C at a rate of 16.25 °C/min with 100 sccm of argon (as the temperature of the furnace approaches T = 650 °C, the temperature around the sulfur powder, placed upstream at a lower temperature near the edge of the furnace, increases to above the melting point (T ~ 115 °C), then the sulfur starts to melt), maintain at T = 650 °C for 5 minutes and cool to room temperature.

In addition, the device fabrication and the measurement in this chapter were carried out as follows. Electrode contacts were drawn by a standard photolithography and lift-off process. The Au (50 nm) source and drain electrodes were deposited by thermal evaporation. To minimize the effects of physisorbed gas molecules, such as oxygen and water on the MoS_2 surface, all measurements were performed at room temperature after thermal annealing at around T = 200 °C for more than 2 hours in a vacuum. Either a 450 nm or 650 nm laser with transistor-transistor logic (TTL) modulation was focused onto the devices. Finally, characterization of the electrical properties were carried out using a Keithley 4200-SCS Parameter Analyzer, Lecroy HD4000 high definition oscilloscopes, Stanford Research Systems SR570 current preamplifiers, and a Cascade Microtech probe station.

5.3. Charge trapping on MoS_2 monolayers

Figure 5-1 shows the schematic of the proposed optoelectronic memory device based on a field-effect transistor (FET) structure. A large-scale monolayer of MoS_2 with single crystalline structures was synthesized by vapour phase transport coupled with a surface functionalization process.[24-26] Figure 5-2 shows that large-sized MoS_2 crystals with well-defined side facets are grown on the SiO_2 substrate with a size of around 100 μm, and the crystals are merged to form a continuous layered MoS_2 film. The difference in Raman peaks between the E^1_{2g} and A_{1g} mode

(18.8 cm^{-1}) in Figure 5-3a, the height profile (~0.7 nm) of the AFM image in Figure 5-3b confirm that the as-grown MoS_2 is indeed a monolayer.

Because of the high surface-to-volume ratio, charge trapping originating from defects at the inherently imperfect MoS_2/SiO_2 interface is an inevitable phenomenon that can cause electrical hysteresis.[14,27] Thus, in order to rule out any unintended defect issues and successfully exploit the charge trapping characteristics at the interface, oxygen plasma treatment was intensively carried out on the SiO_2 substrates before the growth of the monolayer. Note that such treatment not only removes any contaminants that act as interfacial defect sites, but also induces a chemically and structurally-tailored surface layer on the SiO_2 with functional silanol groups (Si-OH) that exhibit strong polar interaction[16,28-29], hence causing a direct modulation of the energy band structure in monolayer MoS_2. Explicitly, this results in uniformly distributed local potential fluctuations that are able to trap electrons energetically[16,29] as shown in Figure 5-1b.

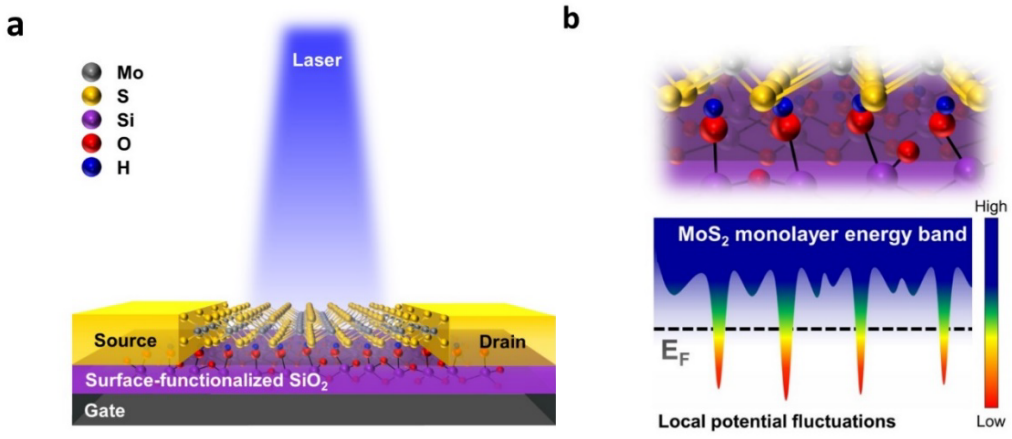

Figure 5-1. Optical memory device structure. a) Schematic of the fabricated memory device where the MoS_2/SiO_2 interface is functionalized with silanol groups. b) Schematic of the enlarged MoS_2 atomic structure with functional groups and a simplified energy band structure showing the local potential fluctuations induced by intentionally-generated artificial trap sites.

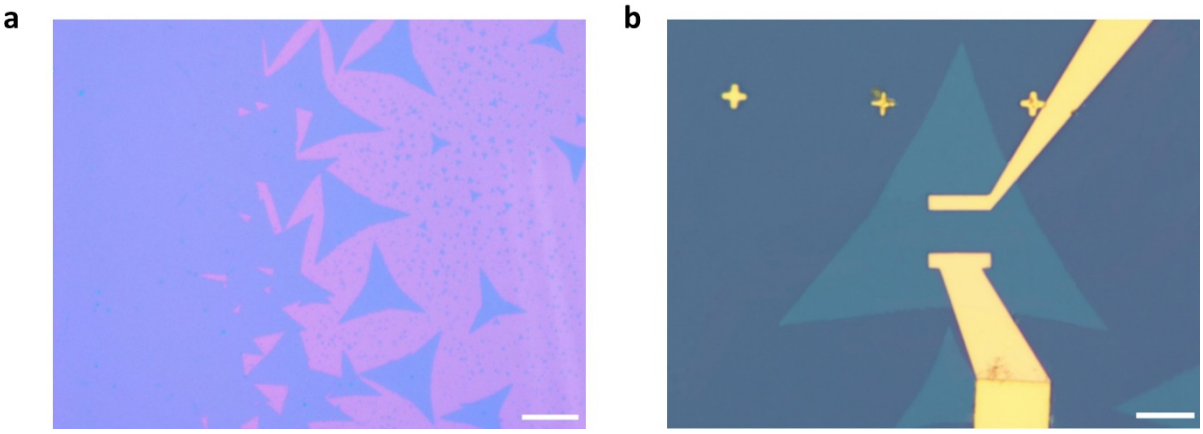

Figure 5-2. Optical images of monolayer MoS_2 grown on SiO_2. a) Optical image at the edge of the substrate. Magenta and violet indicate the SiO_2 substrate and the MoS_2 monolayer, respectively. Scale bar: 50 μm. b) Optical image of the typical layered MoS_2 FET with a back-gate structure. Scale bar: 5 μm.

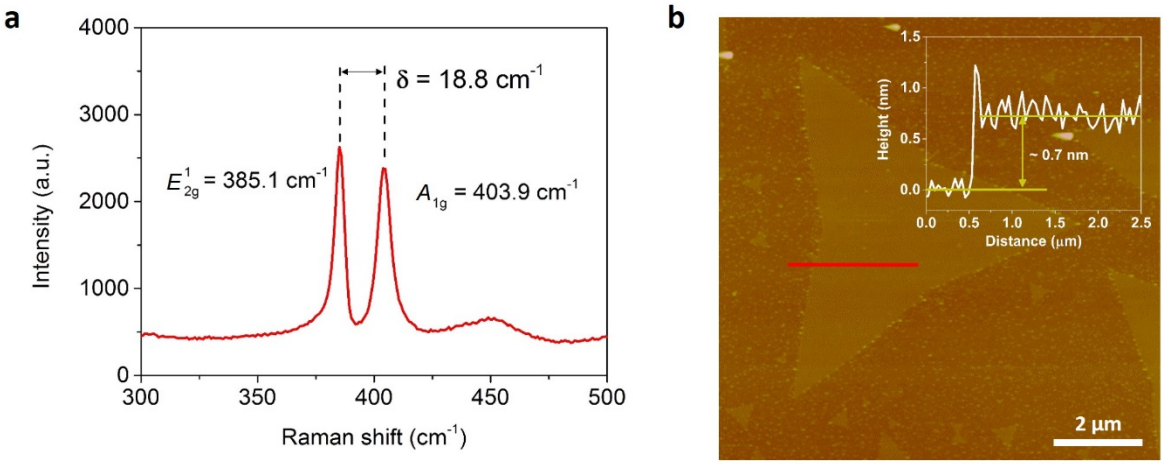

Figure 5-3. Structural properties of the MoS_2 monolayer. a) Raman spectrum obtained from monolayer MoS_2 crystals grown on SiO_2. b) The AFM topography image of an isolated monolayer of MoS_2 and the corresponding height profile extracted from the red line (inset).

Figure 5-4 shows that the water contact angle on the pristine substrate was 48°, which means that the substrate was hydrophobic because of the presence of organic contaminants on the surface. However, the water contact angle approached almost 0° after treating the surface for 5 minutes, which indicates that the surface becomes hydrophilic due to the elimination of the organic contaminants and the introduction of Si-OH functional groups on the surface due to the treatment process. Furthermore, it is observed that the surface can also maintain its hydrophilic property after annealing the substrate at the same conditions as the growth process (T = 650°C for 5 minutes in Ar atmosphere), but without precursors so as to rule out the possibility that the value of the water contact angles on the surface-treated substrate can be affected by the precursors adsorbed on the surface.

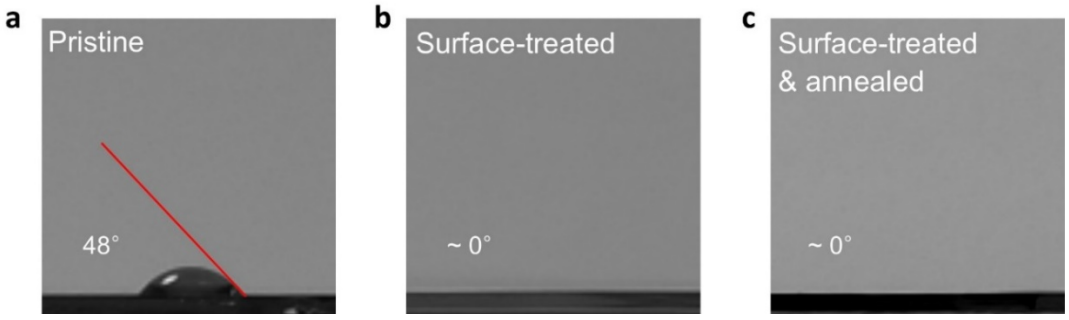

Figure 5-4. Images of water contact angles on SiO_2 substrates. a) Pristine substrate, b) Surface-treated substrate, and c) Surface-treated and then annealed substrate.

The Fourier-transform infrared spectroscopy (FTIR) analysis was conducted in Figure 5-5. Only a negligibly small amount of –OH groups, indicated by a peak ranging from 3000 cm^{-1} to 4000 cm^{-1}, was found before the surface treatment, while the intensity of the peak related to the Si-OH stretching mode significantly increased after the treatment. This clearly shows that the surface treatment introduces Si-OH groups on the surface. In addition, similar to the results for the water contact angle, most of the –OH groups remain on the surface after annealing at T = 650 °C for 5 minutes, even though the total amount of –OH groups decreases slightly.

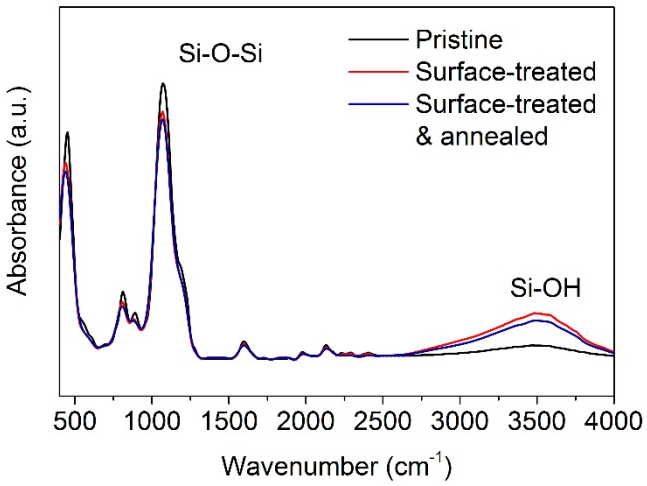

Figure 5-5. FTIR analysis of the SiO_2 substrate. Before the surface treatment (black), after the treatment (red), and after annealing at T = 650°C following the treatment (blue).

Figure 5-6 shows the effect of surface treatment on the I-V transfer curves. The device on the pristine substrate without functional groups exhibited a mobility of 5 cm^2 V^{-1} s^{-1} for a voltage sweeping direction from -60 V to 60 V and an ON/OFF ratio of ~10^7. Even though the measurement was done after thermal annealing in a vacuum, the typical hysteretic behaviour of an n-type MoS_2 FET on the pristine substrate was found to exhibit a relatively small hysteresis window compared to devices on the surface-treated substrates as shown in Figure 5-6. The hysteresis window is defined as the maximum voltage shift at I_{SD} = 1 nA, which is related to the transition voltage in the transfer curves. It should be noted that it is believed that the hysteresis observed for the monolayer MoS_2 on the pristine substrate is not significantly affected by air or oxygen, but is caused by natural defects on the underlying SiO_2 substrate. This is because the relatively small hysteresis appears to be unchanged after both thermal annealing and vacuum treatment as well as surface passivation.[27,30] On the other hand, the

device on the surface-functionalized substrate showed a relatively reduced conductance and a larger hysteresis window of 43 V (3 minutes), and 60 V (5 minutes) due to the artificially-introduced trap sites. The device on the substrate treated for 10 minutes showed a similar hysteretic behaviour, which means that the charge trap sites are almost saturated after treating the surface for more than 5 minutes.

The trapped carrier density (N_{trap}) can be approximately calculated using a static parallel-plate capacitor model,[18] with $N_{trap} = (C_{total} \Delta V_{th})/e$, where C_{total} is the capacitance per unit area of the device, ΔV_{th} is the difference in the threshold voltages, and $e = 1.602 \times 10^{-19}$ C is the elementary charge. Although C_{total} is calculated according to the formula, $1/C_{total} = 1/C_{SiO_2} + 1/C_{MoS_2}$, where C_{SiO_2} and C_{MoS_2} are the capacitances per unit area of the 300-nm-thick SiO_2 and 0.7-nm-thick MoS_2, respectively, C_{MoS_2} can be considered to be negligible because C_{MoS_2} is much larger than C_{SiO_2} due to the relatively thin thickness (the relative permittivities of MoS_2 (4.26) and SiO_2 (3.9) are similar). In addition, for a simple calculation, it is assumed that the contribution of trapped charges to the change in C_{total} is also negligible. Thus, C_{total} is assumed to be constant and equal to C_{SiO2} (~ 11.5 nF cm^{-2}). The device on the pristine substrate showed ΔV_{th} = 6 V, corresponding to a trapped carrier density (N_{trap}) of 4.3 x 10^{11} cm^{-2}, while 20 V, 1.44 x 10^{12} cm^{-2} (3 min) and 30 V, 2.2 x 10^{12} cm^{-2} (5 min), and 31 V, 2.23 x 10^{12} cm^{-2} (10 min) were extracted from the device on the surface-treated substrates, respectively. The trapped carrier density was found to increase as the surface treatment time became longer. These results indicate that the surface treatment introduces a number of silanol groups (Si-OH) on the SiO_2 substrate so as to trap more electrons at a high positive gate voltage.

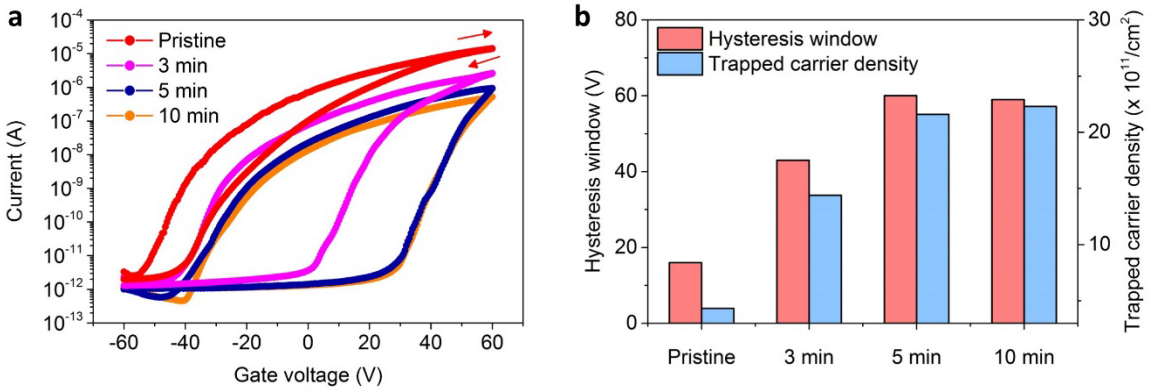

Figure 5-6. Effects of surface treatment on the transfer curves. a) Hysteretic behaviour of the devices on the pristine substrate without surface treatment (red) and on the substrates treated for 3 minutes (magenta), 5 minutes (blue), and 10 minutes (orange) at V_{SD} = 3 V. The arrows indicate the direction of the gate bias sweep. b) Hysteresis windows and trapped carrier densities for the devices on the pristine substrate and on the surface-treated substrates based on the results in (a).

The PL position and intensity have been also investigated as the surface treatment time increases (Figure 5-7). Each PL measurement was conducted after applying a positive gate pulse for 1 s (0 V → 80 V → 0 V) in order to investigate in detail how the PL spectra behaviour is affected by the modulation in the electron density through the artificial trap sites that are induced by the surface treatment. It was observed that the PL peak became more intense and shifted to blue wavelengths with an increase in the surface treatment time. However, the PL peak showed a saturated trend after treating the surface for more than 5 minutes. Figure 5-7c also shows that the intensity of the A exciton gradually increases with the plasma treatment time and then becomes almost saturated after 5 minutes of treatment, while the intensity of the negatively charged A^- exciton (trions) remains almost the same. This suggests that the A exciton recombination is dominant on the surface-treated substrates due to a lowering of the Fermi energy level resulting from the induced trap states, causing a decrease in the number of excess electrons in the monolayer MoS_2. Note that it has been reported that in general, trion recombination mainly occurs for heavy electron doping.[31]

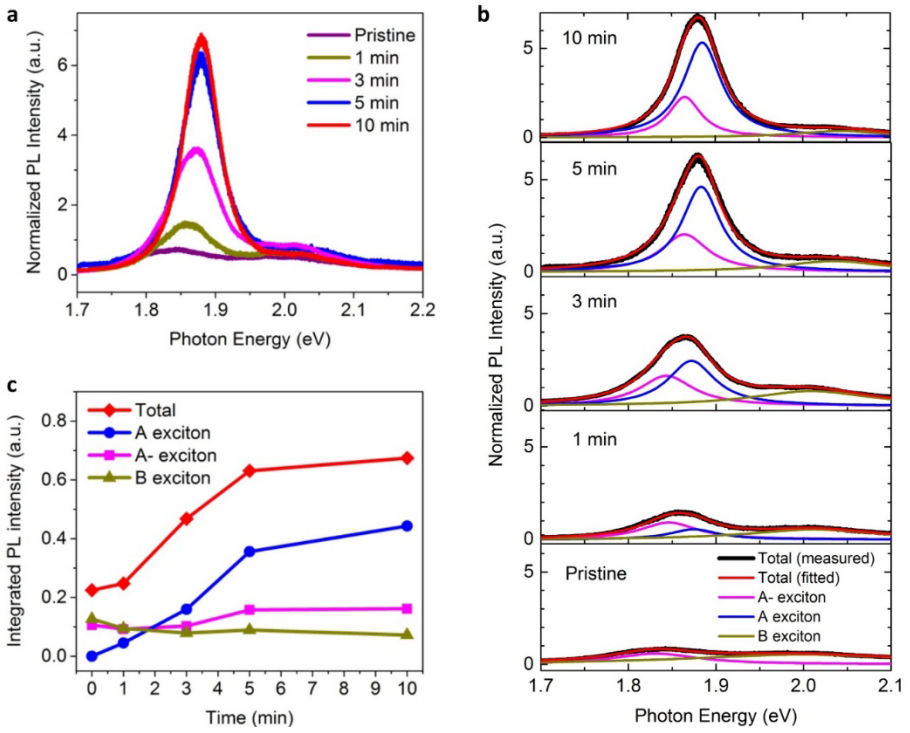

Figure 5-7. Evolution of the PL spectrum with surface treatment times. a) Normalized PL spectra obtained at each plasma treatment time (pristine, 1 , 3 , 5 , and 10 minutes). b) Analysis of the profiles of the PL spectra was performed by deconvoluting each PL plot, which has been fitted with Lorentzian curves to calculate the intensities of the A^- exciton (trion), the A exciton, and the B exciton peaks. c) Integrated PL intensities of each exciton with surface treatment times.

On the basis of the hysteretic behaviour in the electrical transport[14,18] (Figure 5-6) as well as the more intense and blue-shifted PL spectra[31] that was observed with an increase in the treatment time (Figure 5-7), it was confirmed that after treating the surface for more than 5 minutes, charge trapping at artificially-generated trap sites leads to a complete depletion of the electrons from the channel when sweeping the gate voltage back from a large gate voltage above 60 V to below 20 V. In contrast, the devices on a pristine substrate without surface functionalization were found to exhibit weaker charge trapping and depletion characteristics. In addition, it was observed in Figure 5-8 that the photoresponsivity of the surface-treated device consisting of a basic phototransistor structure was still high enough to be used as an

optical memory cell, even though the photoresponsivity decreases slightly compared to that of the device on the pristine substrate The device on the pristine substrate exhibits a photoresponsivity of around 1740 A W^{-1} at a gate voltage of V_g = 60 V and an optical power per unit area of 7.6 pWcm^{-2}, which is superior or comparable to previously reported results for phototransistor applications.[9,32] On the other hand, the device on the surface-treated substrate shows a photoresponsivity of 415 A W^{-1} under the same conditions. Even though the photoresponsivity decreases after surface treatment, it is still much higher when compared to that of other 2D materials.[33-35] The high photoresponsivity, even on the surface-treated substrate, originates from the strong light-matter interaction on the monolayer MoS_2, and makes the material suitable for memory device applications.

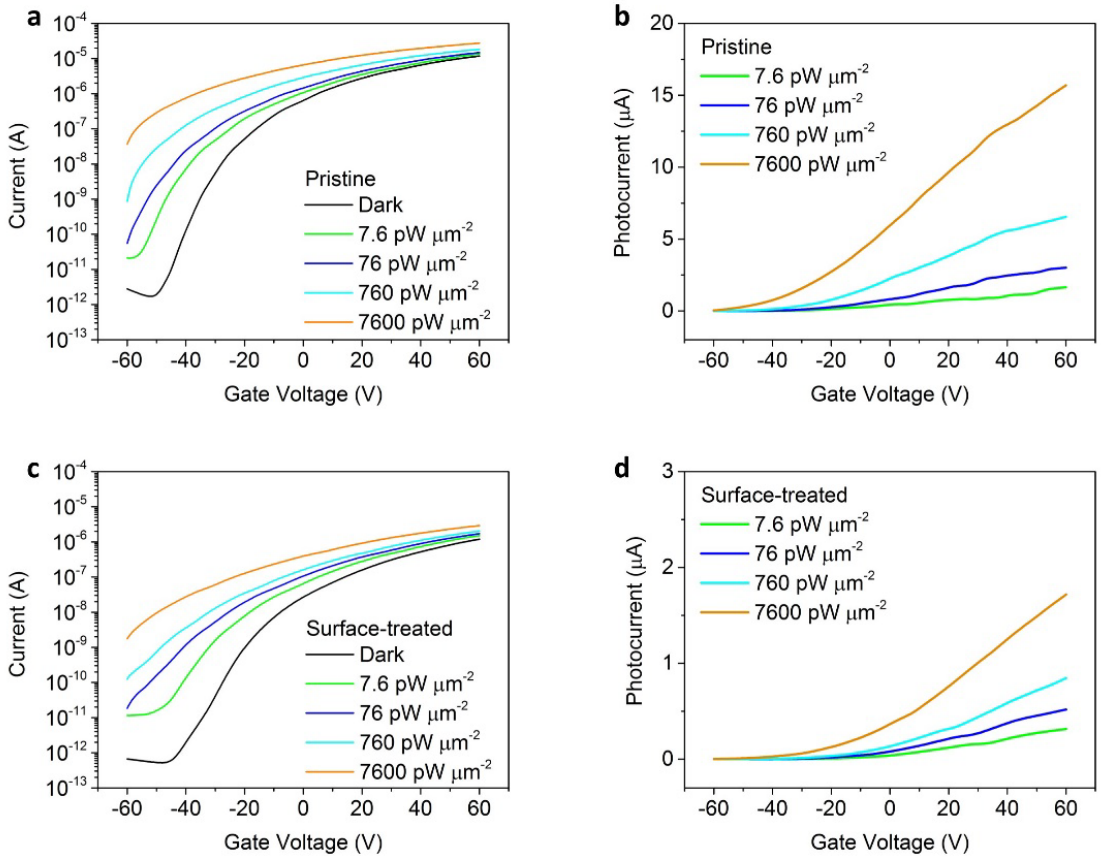

Figure 5-8. Photoresponse and photocurrent of monolayer MoS_2 photodetectors. On pristine substrates (a, b) and surface-treated substrates (c, d). The photocurrent was obtained by subtracting the dark current from each curve in (a) and (c).

5.4. Optical memory operating principle

Figure 5-9 shows the experimental results for the basic memory functions and the operating principle of the optical memory cell. Since the MoS_2 channel exhibits n-type properties, a positive gate voltage (V_G = 20 V) is applied without a source-drain bias to form the potential well with a bending of the energy band between two electrodes that act as Schottky barriers. When a 1 second gate pulse (80 V) is applied (Reset operation), a considerable number of electrons in the channel will be filled into the artificial trap sites due to the increase in the Fermi level[36]. Therefore, as the applied gate voltage returns to V_g = 20 V, the electron concentration in the conduction band will dramatically decrease (Initial state) because of the large number of trapped electrons, which can screen and attenuate the gate electric field across the channel (a gate screening effect).[18,37] Consequently, when a source-drain bias (V_{SD} = 3 V) was applied without illumination (Readout for OFF-state), the current level dropped to below 4 pA, and the readout charge integrated over 1 second was found to be less than 2 pC (left inset of Figure 5-9a). Note that before the reset operation, a much larger current can flow with the application of a source-drain bias on the order of tens of nAs as shown in Figure 5-10.

In order to address an optical memory storage capability, the device channel was illuminated with a 450 nm laser pulse for 1 second (Light exposure), which in turn, generates electron-hole pairs in the MoS_2 monolayer. Photo-generated holes can easily escape from the channel through a bending upwards of the energy band and these can also release trapped electrons through surface electron-hole recombination,[9] thus leaving behind the accumulation of photo-generated electrons in the conduction band. Additionally, the removal of trapped electrons on the MoS_2/SiO_2 interface alleviates the gate screening effect, resulting in more

electrons in the conduction band. As a result, substantially more electrons can be stored in the potential well with a longer lifetime. During the waiting time after the removal of the light source, the device is kept in dark conditions under the same gate voltage, but still without a source-drain bias voltage.

Finally, when the readout bias was applied to extract the accumulated charge carriers from the potential well after a duration of 500 ms (Readout for ON-state), the readout current was found to increase to 7.7 nA. Because the current level has a tendency to return to the original current level that normally flows through the channel at the applied gate and source-drain bias by releasing the additionally stored charge, some relaxation was observed. In this case, the integrated readout charge was found to reach 4.6 nC. With these values, the ON/OFF ratio of the readout charge was calculated to be around 3100, which enables us to effectively detect and discern a wide range of exposure dosages. It is important to note that a similar amount of readout charge was obtained from ten other devices under the same light exposure conditions, which demonstrates the reproducibility of the device performance (Figure 5-11). On the other hand, the ON/OFF ratio for the readout charge was found to be significantly reduced in comparison to below 2 for the pristine substrate, which is consistent with previously reported devices[23], because the relatively high readout current obtained for the OFF-state could not be easily suppressed without the artificial trap sites (Figure 5-12). It was further demonstrated that the device could be operated sequentially using the reset operation after each readout for the ON-state (right inset of Figure 5-9a). This operating principle can give the device a critical advantage regarding optoelectronic memory, which will be discussed in more detail later in this chapter.

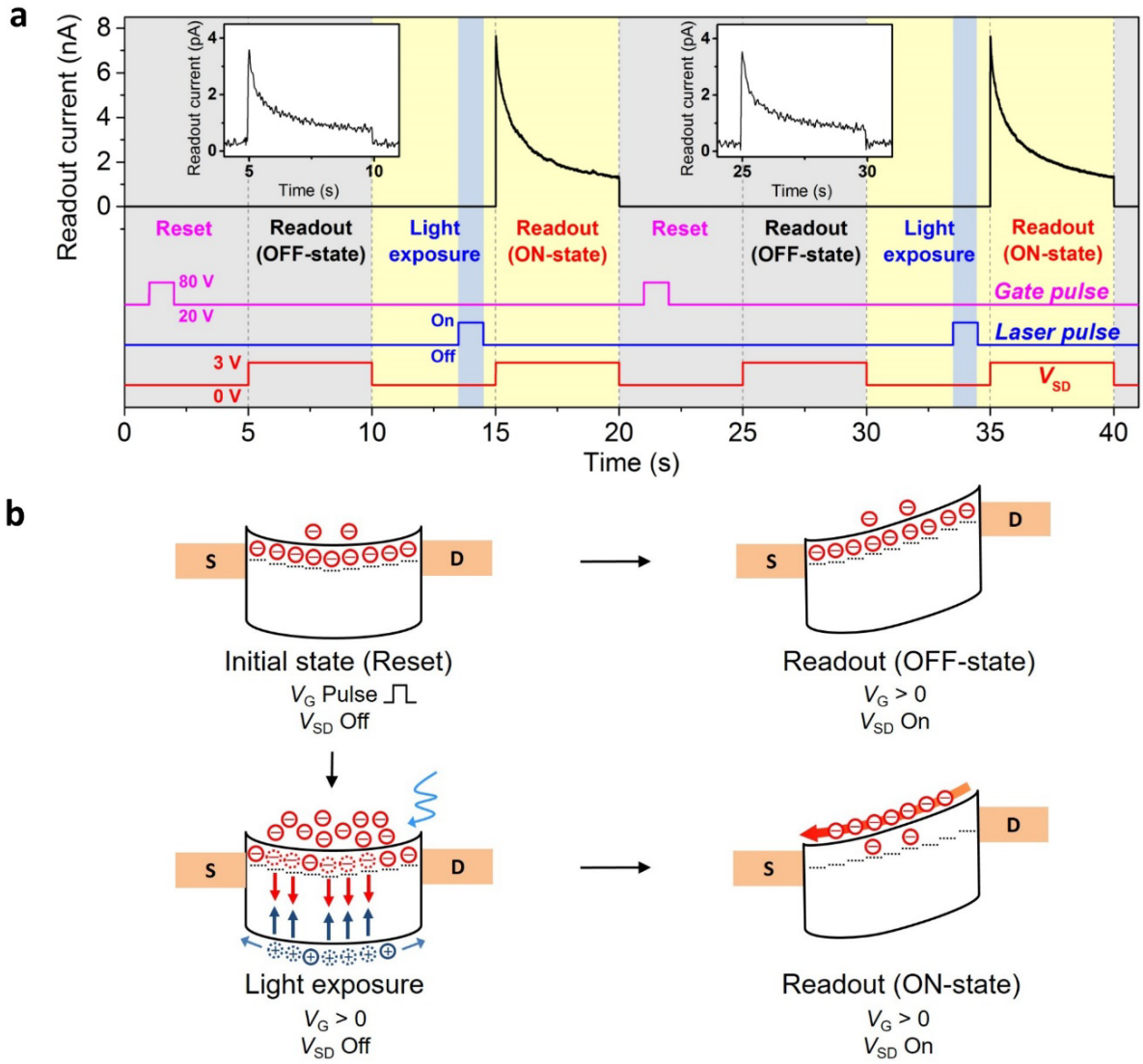

Figure 5-9. Basic functions of the optical memory device. a) Operating sequence and readout current obtained from the optoelectronic device. The blue vertical shaded column indicates the period of time when the device was illuminated with a 450 nm laser with a power of 19 nW (P_{LED}). A gate pulse (V_G = 80 V) and a source-drain readout bias (V_{SD} = 3 V) were applied for the reset and readout operations, respectively. b) Energy band diagram of the optoelectronic device for the basic operations, depicting the initial state (reset operation), light exposure, and readout for ON- and OFF-states. The dotted lines under the conduction band represent the artificially-introduced electron trap sites at the interface between the channel and the underlying SiO_2 substrate.

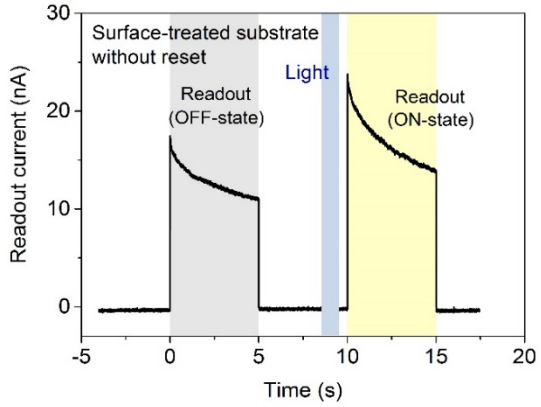

Figure 5-10. Optical memory operation without a reset function. The readout current for the OFF-state was around tens of nA without the reset operation, although the readout current for the ON-state increased after light was illuminated on the device. The ON/OFF ratio of the readout charge was found to be less than 2, which made it difficult to clearly distinguish between the ON/OFF state conditions.

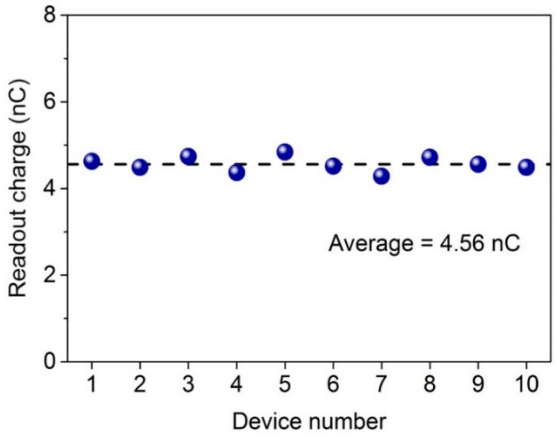

Figure 5-11. Uniformity of the readout charge for different memory cells. Ten different devices were tested to statistically examine the uniformity and reproducibility of the readout charge. The readout charge obtained from the ten devices was found to be within a similar range. The average value was 4.56 nC (dashed line). The light exposure time, the waiting time, and the integration time were 1 s, 0.5 s, and 1 s, respectively, for all the devices. The uniformity of the readout charge indicates that the surface treatment induces a uniform surrounding environment at the interface between the MoS_2 and the substrate.

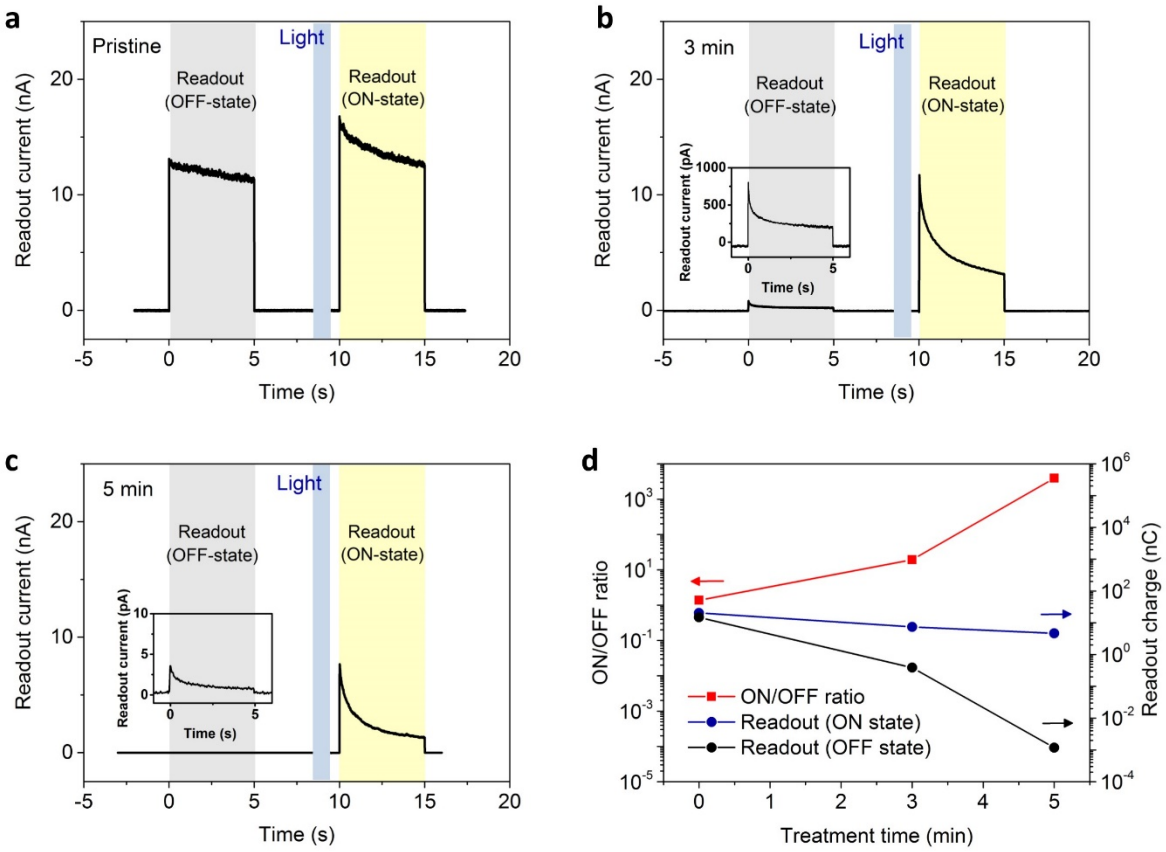

Figure 5-12. Surface treatment effect on the optical memory behaviour. a) The readout current for the OFF-state after the reset operation was found to be significantly higher for the pristine substrate. The reset effect is relatively weak because the trapped carrier density is much lower than that of the device based on the surface-treated substrate. It shows no significant difference between the OFF- and ON-state readout for a 1 s light exposure time and a 0.5 s waiting time. b, c) The readout current for the OFF-state dramatically decreases as the surface treatment time increases to 3 minutes (panel b) and 5 minutes (panel c) due to the artificially-induced trap sites, while the readout current for the ON-state drops only slightly. d) As a result, the ON/OFF ratio of the readout charge sharply increases from 1.37 (for the pristine substrate) to 3930 (5 min-surface-treated substrate).

5.5. Linearity of the optical memory device

One of the most important parameters for practical applications, especially image sensing, is a linear response with respect to the light exposure dosage so as to be able to detect the contrast of images accurately. If the photo-response deviates from linearity or saturates for a small amount of exposure, it is then difficult to quantify the exact dosage. Figure 5-14a shows the readout current measured after illumination as a function of light exposure times from 1 to 3000 ms. Photo-responsive memory features were observed even in a short light exposure time of 1 ms, corresponding to an optical energy smaller than 17 pJ (inset of Figure 5-13a). The readout charge was also extracted by integrating the readout current for 1 second after a waiting time of 0.5 s without a source-drain bias voltage (Figure 5-13b). The fitted result shows that the readout charge (Q_{ro}) was linearly dependent on the light exposure time (t_{ph}) up to 1500 ms ($Q_{ro} \approx t_{ph}^{\alpha}$, $\alpha = 0.99$) and was directly proportional to the dosage or the number of incident photons. However, when the exposure time increased above 2000 ms, the readout charge started to deviate from a linear relationship and then saturated at around 7.1 nC (inset of Figure 5-13b). This saturated charge level was almost the same as that obtained when irradiated with a 650 nm red laser, which shows that the device had a specific full-well charge capacity regardless of the wavelength of light (inset of Figure 5-13b). In addition, Figure 5-14 shows that the collected readout charge at various integration times from 50 to 5000 ms also depended linearly on the exposure time, which means that the integration time can be selected according to the device requirements. It was also confirmed in Figure 5-15 that the readout charge was linearly proportional to light intensity from 19 pW to 19 nW. As a result, 8 different states could be identified with a sufficiently large separation between any two consecutive states.

Based on the ON/OFF ratio of the readout charge as shown in Figure 5-13c, it was found that the linear dynamic range (LDR), which represents the ratio of the full-well charge

capacity to the dark readout charge within the linear region, was found to be 4700 (73.4 dB) after a 1500 ms exposure time. This LDR is larger or comparable to consumer grade Si-based CCDs (60~70 dB)[38], providing the possibility of multi-level detections with a 12-bit analog-digital converter. The results indicate that a high sensitivity was achieved and maintained over a wide exposure timescale because the charge quantity is directly associated with the dosage.

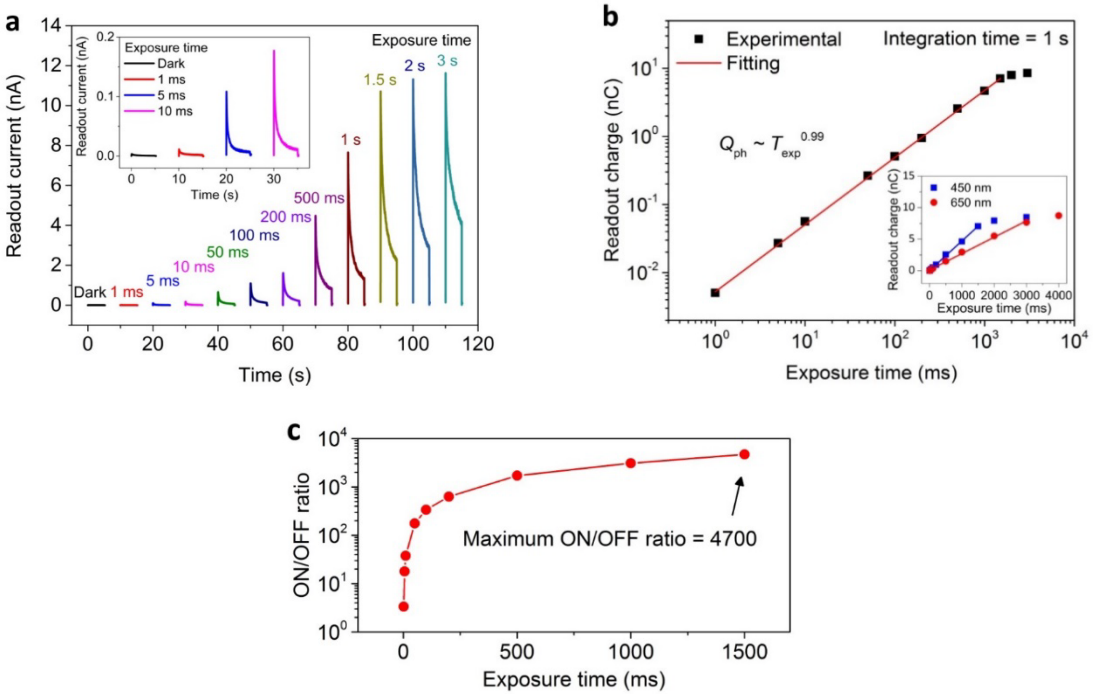

Figure 5-13. Photoresponse characteristics of the MoS_2 optoelectronic memory device for different exposure times. a) Readout current as a function of light exposure times up to 3000 ms. The plots were separated with an interval of 10 second, regardless of the time that was measured initially. The readout bias voltage was applied after a 500 ms waiting time. The inset represents an enlarged view of the readout current for different exposure times from dark conditions up to 10 ms. b) The extracted readout charge (in log scale) obtained by integrating the readout current for 1 second with increasing exposure time. The fitted line (red), using the power-law function, indicates that the readout charge was linearly proportional to the exposure time or dose for the range below 1500 ms. The inset shows the readout charge (on a linear scale) as a function of exposure times for a different excitation wavelength (λ = 650 nm) showing a similar linear dependence and almost the same saturated charge value. c) The ON/OFF readout charge ratio as a function of exposure time.

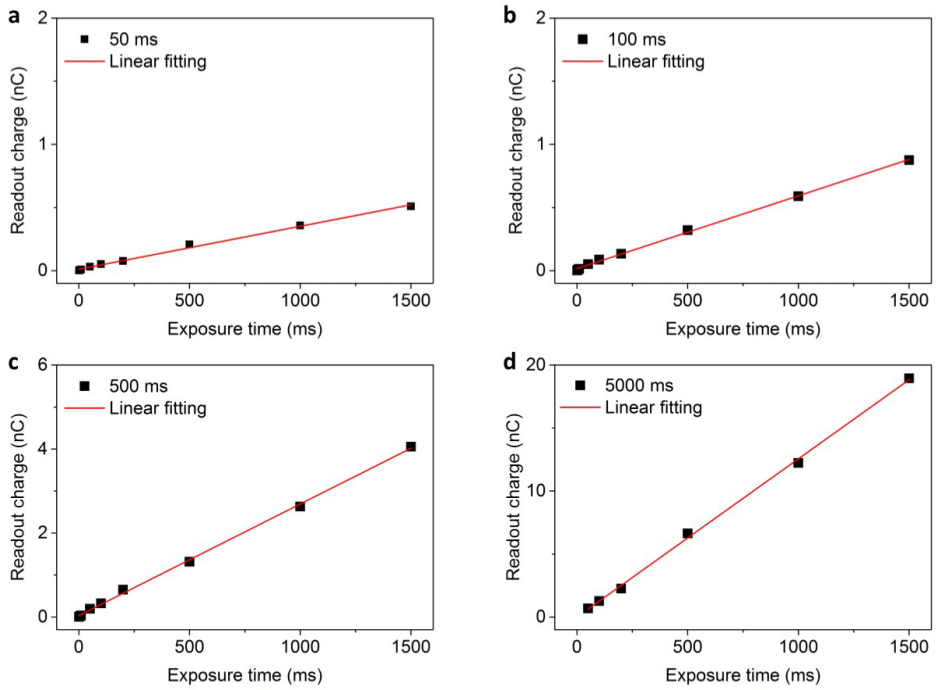

Figure 5-14. Readout charge collected from different integration times. a) Readout charge integrated for 50 ms, b) 100 ms, c) 500 ms, and d) 5000 ms. The light exposure time and the waiting time of the 450 nm laser were 1 s and 0.5 s, respectively.

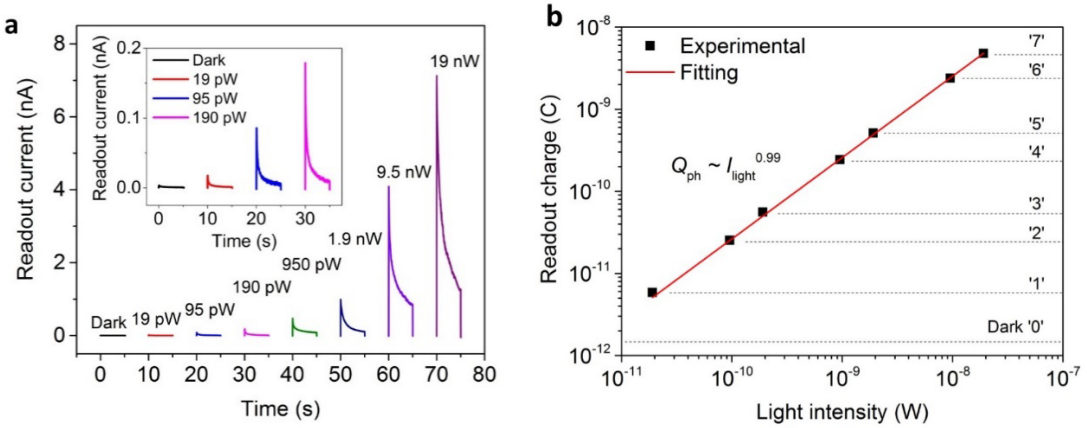

Figure 5-15. Characterization of the optical memory with varying light intensity. a) The readout current as a function of light intensity. The plots were separated with an interval of 10 s, regardless of the time that was measured initially. The light exposure time was 1 s, and the readout bias was applied after a 500 ms waiting time. The inset represents an enlarged view of the readout current for different light intensity from dark conditions up to 190 pW. b) The extracted readout charge (log scale) obtained by integrating the readout current for 1 s with increasing light intensity. The fitted line (red), using a power-law function, indicates that the readout charge is linearly dependent on the light intensity.

5.6. Charge storage time

Another important parameter for image sensing and memory devices is the charge storage lifetime. Figure 5-16a shows the readout current in the ON-state as a function of the waiting time before readout. The light exposure duration was fixed at 1 second, and the readout was also conducted for 1 second, which is identical to that of the exposure time-dependent experiment described previously. To examine the progressive time-evolution of electrons stored in the potential well, the integrated readout charge as shown in Figure 5-16b was plotted. The resulting amount of the readout charge was adequately fitted by two exponential functions expressed as

$$Q_{ro}(t) = A_1 \, exp\,(-t/\tau_1) + A_2 \, exp\,(-t/\tau_2) + Q_{ss} \qquad (5.1)$$

where τ_1, τ_2 are the time constants of the decay process, A_1, A_2 are the constants determined by the light intensity and other device parameters, and Q_{ss} is the readout charge at steady-state. The two characteristic decay time constants were estimated to be 12.0 s and 1309.7 s. These results clearly indicate that there are two different types of decay process occurring in the device. The first decay process predominantly arises from the photo-generated electrons that have an extended lifetime through the surface recombination of the photo-generated holes with the electrons trapped at the interface. This effect mainly lasts up until 100 s and then disappears completely after that time. It is believed that the photo-generated electrons stored in the potential well might escape through the source and drain electrodes during the first decay period, overcoming the Schottky barrier due to thermal fluctuations as can be seen in Figure 5-9b.[23,39]

The subsequent decay process, which is found to have an extremely slow time constant, is believed to originate from a weakened gate screening effect. The gate screening effect occurs after the Reset operation as explained in Chapter 5.4. A large amount of the trapped charges at

the interface between the monolayer and the silicon oxide significantly alleviate the effect of the gate voltage. As a result, the electron concentration in the conduction band in the MoS_2 monolayer decreases dramatically after the Reset operation. However, when light is illuminated on the device, the effect of the original gate biasing is recovered upon the removal of trapped electrons at the interface through recombination with photo-generated holes; this helps to not only maximize the induction of electrons in the conduction band in the MoS_2 monolayer, but also to store more electrons in the potential well as a result of the enhanced gate field effect. It is expected that such a constructive gate field effect will last for a long time because it is not easy to return the channel to the reset state at a gate voltage of 20 V without the application of the reset gate pulse, as discussed earlier (Figure 5-9a). In other words, the effect of the gate bias voltage (20 V) after illumination with light is considerably stronger due to the decreased amount of trapped charges, and the second decay process occurs very slowly with a relatively long decay time constant (1309.7 s) if no further action is taken on the device. Only a very small amount of electrons might be recaptured at trap sites during the waiting time (Figure 5-16b). Consequently, information can be stored and retrieved while maintaining a high ON/OFF ratio greater than 500 even after waiting for a period of 10^4 s, consuming only a very limited amount of power without a source-drain bias (Figure 5-16c). Finally, the readout charge of the device converges to the steady-state value ($Q_{ss} \sim 0.75$ nC).

In most commercial image sensor applications, such as CCD and CMOS technologies, the main elements consist of a combination of photodetector and non-volatile memories. The information collected from the photodetector is usually transferred to the non-volatile memory so that it can be stored for a long time. However, the results in this chapter indicate that the optical memory device, which has a long storage lifetime could have, fundamentally, great potential in the development of much simpler image-sensing chip architecture without the addition of non-volatile memory arrays typically required for charge storage.

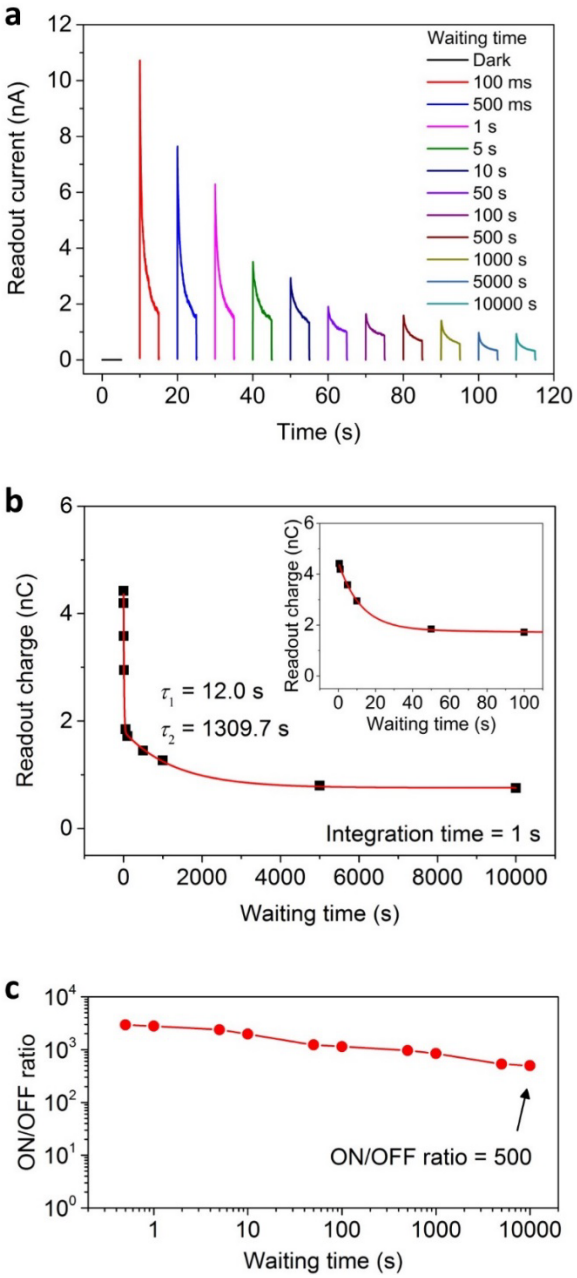

Figure 5-16. Photoresponse characteristics of the MoS_2 optoelectronic memory device for different exposure and waiting times. a) Readout current in the ON-state as a function of the waiting time up to 10^4 s. The graphs were separated evenly with an interval of 10 s, regardless of the time measured initially. b) The extracted readout charge obtained by integrating the readout current over 1 second with increasing waiting time. Two decay time constants, 12.0 s and 1309.7 s, were estimated by using the double exponential fitted line (red). The enlarged graph of the readout charge extracted for a waiting time of up to 100 s is shown in the inset. c) The ON/OFF ratio for different waiting times. The ON/OFF ratio was found to be maintained above 500 even after waiting for 10^4 s.

5.7. Stability of dark current and the effects of gate voltage

Since a low dark current is essential in obtaining a high ON/OFF ratio in optical devices, the stability of the dark (OFF-state) readout current in the devices was further investigated. Even in the absence of light exposure, thermally excited electrons can be collected in the potential well and contribute to the readout signal, thus decreasing the device performance. In Figure 5-17a, the temperature-dependent dark readout was performed for 500 s with a period of 10 s at various temperatures ranging from T = 293K to T = 333K. When the device was kept at near room temperature (T = 293K), the peak in the dark current showed no significant change at about 4 pA for 500 s. Similarly, the readout charge, which was integrated over the dark current for 1 s, remained at almost the same value of less than 2 pC for the whole process time. When the operation was carried out at T = 313K, the peak in the current and the readout charge increased to 17 pA and 13 pC, respectively, however, the peak value in the dark current remained stable. This trend was also observed at an even higher temperature of T = 333K, where a stable peak current (50 pA) and readout charge (40 pC) were obtained. These results indicate that the dark current remains stable at a given temperature. The increase of the dark current with temperature is believed to originate from electrons that are released from trap sites by thermal excitation, similar to the phenomena reported in CCD image sensors.[40] This thermal noise can cause the dark current to rise significantly, which leads directly to the deterioration of the readout ON/OFF ratio from 2340 at T = 293K to 161 at T = 333K (Figure 5-17b). Therefore, it is needed to keep the temperature lower to obtain a higher ON/OFF ratio.

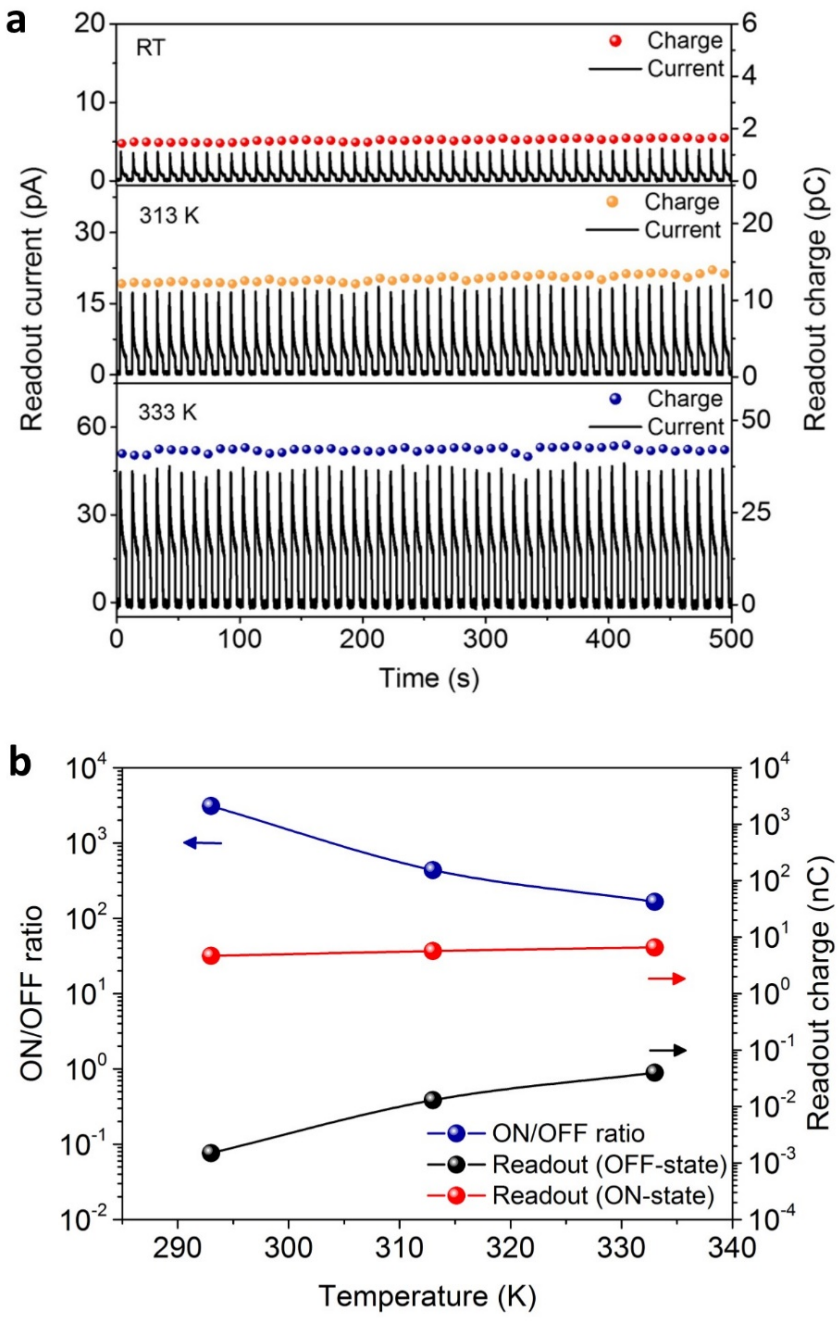

Figure 5-17. Dark readout stability and dependence on temperature. a) Dark readout operations for 500 s at T = 293K, T = 313K, and T = 333K. Dark readout current was stable at three different temperatures; however, it was found to gradually increase at higher temperatures because of electrons being thermally excited out of the trap sites. b) Readout charge for the ON/OFF-states and ON/OFF ratio as a function of temperature.

To address how much the initial gate bias can affect the readout current, the device characteristics as a function of initial gate voltages under the same conditions as that shown in Figure 5-9a were also investigated. Figure 5-18 shows that in the range of initial voltages from 0 to 20 V the dark readout charge stayed at almost the same value of ~1.5 pC, while it increased gradually above 20 V and reached a value of 27.3 pC at 50 V, causing a significant decrease in the ON/OFF ratio. This is primarily due to the increase in the channel carrier density induced by a high gate voltage. On the other hand, the accumulated charge from the light increased rapidly from 0 V to 20 V and then showed a saturated response above 20 V. These results show that only a gate voltage more than 20 V can guarantee a robust potential well to store the electrons sufficiently. Consequently, the ON/OFF ratio reached its highest value at around 3100 when the device was operated with a gate voltage of 20 V, but it dropped sharply to 590 at 50 V, and to 160 at 0 V. From these results it was confirmed that a gate voltage of around 20 V was optimal for operating the memory cells.

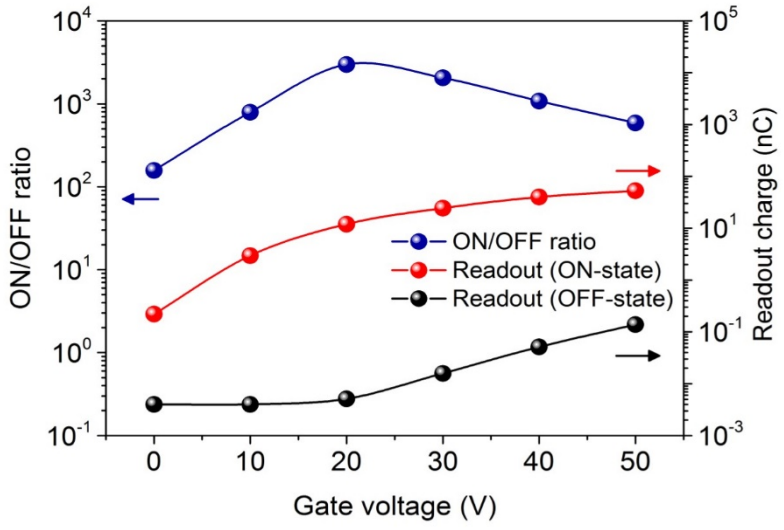

Figure 5-18. Dependence of the device performance on gate voltage. Readout charge for the ON/OFF-states and ON/OFF ratio as a function of gate voltage. The readout charge ON/OFF ratio was found to be the highest at a gate voltage of 20 V.

5.8. Multi-bit operations

The attractive optoelectronic features of the devices – large LDR, low dark current, and relatively long retention time – could potentially open up avenues for other optoelectronic applications. Figure 5-19 shows the multi-bit optical data storage capacity of a single MoS_2 memory cell exhibiting eight different states defined as '0', '1', and so on. Each optical state was written into the MoS_2 monolayer channel with a 100 ms laser pulse, and the time gap between each laser pulse was also 100 ms (Figure 5-19a). As the number of applied laser pulses increased, the ON-state readout current also gradually increased (Figure 5-19b), and the integrated readout charge had a linear relationship with the number of applied laser pulses as shown in Figure 5-19c. The readout charge consistently increased by around 300 pC for each applied laser pulse. It was also confirmed that the multi-bit detection was reliable and reproducible with repeated switching (Figure 5-20 and Table 5-1). In addition, if the noise level of the states could be minimized further, it would make it possible to implement many more states.[41] It is further noted that, even though multi-bit operation could be easily realized by using a single optical pulse with different light intensities during the same exposure time as that shown in Figure 5-15, I have instead demonstrated multi-bit operation by controlling the number of optical pulses at the same intensity. This is because it is much more practical to use a single-intensity light source so as to simplify the system configuration and ensure cost saving, without the need for any additional components to control the light intensity. Although it still remains a challenging task for the device to exhibit permanent optical storage, these findings suggest that it has the potential for optoelectronic multi-level modulation.

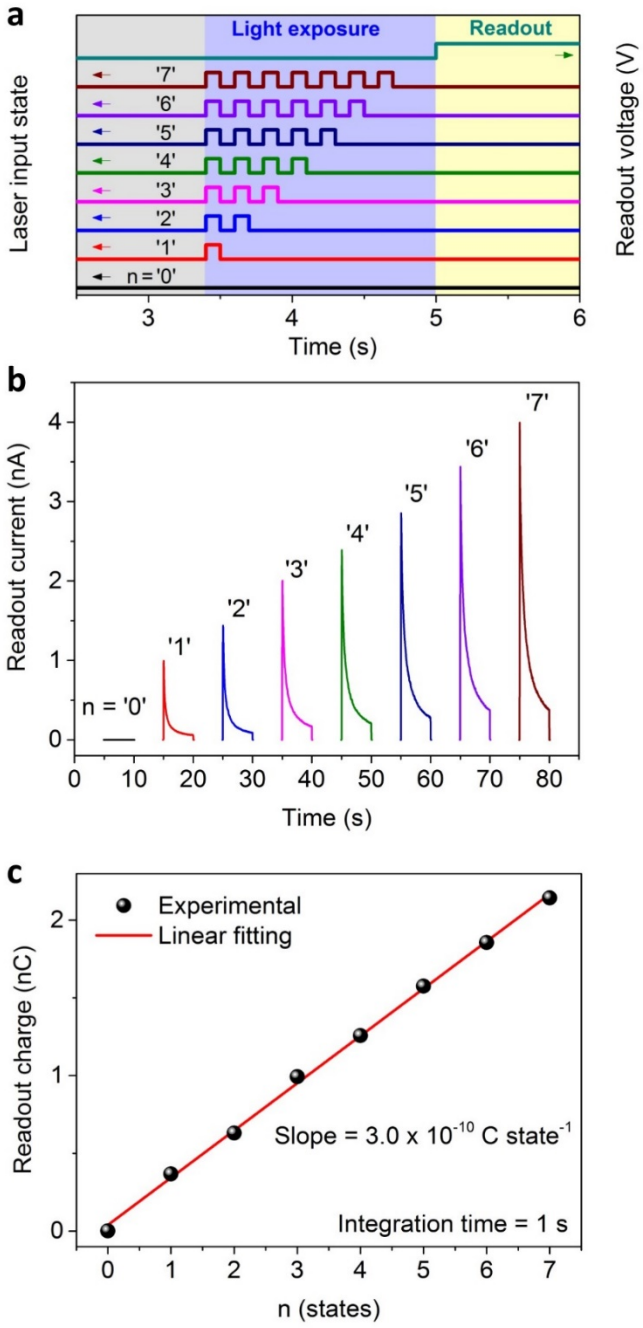

Figure 5-19. Multi-bit response of the MoS_2 optical memory device with different input signals. a) The input of optical laser pulses (blue shade) and the readout stage (yellow shade). Each optical state was written into the MoS_2 device with a 100 ms duration, and the interval between bits was also 100 ms. b) Readout current as a function of the number of applied laser pulses, leading to 8 different optical states (3 bits). The plots were separated with an interval of 10 s, regardless of the time that was measured initially. c) The collected readout charge in the ON-state recorded for 1 s. The line of best fit (red) indicates that the charge increases by 300 pC for each optical laser pulse.

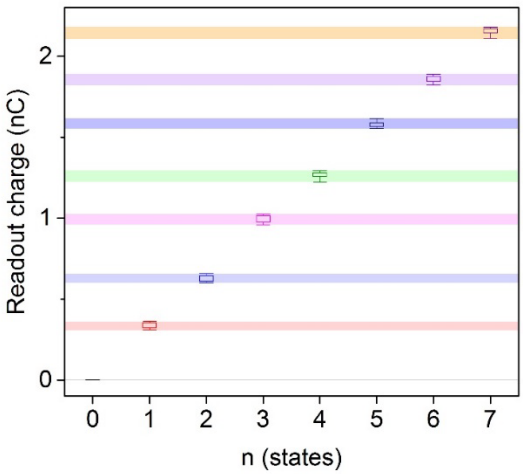

Figure 5-20. Reproducibility of Multi-bit response. Box chart of the readout charge for a multi-bit response of the optoelectronic memory device. The readout of each state is demonstrated over 10 cycles, and the confidence interval for each state is colour-shaded. The significant differences between the readout charges of any two consecutive states are much larger than the confidence interval of each state (Table 5-1), which shows the possibility of multi-bit operation.

State	Average readout charge (nC)	Standard deviation (nC)	Standard deviation (%)
7	2.1550	0.02030	6.87%
6	1.8597	0.01905	6.73%
5	1.5766	0.01827	5.89%
4	1.2664	0.01885	6.96%
3	0.9957	0.02095	5.72%
2	0.6295	0.01855	6.35%
1	0.3374	0.01656	4.92%
0	0.0012	5.90×10^{-5}	–

Table 5-1. Readout charge accuracy for the multi-bit operation of the MoS_2 monolayer optical memory device. Standard deviation for each state calculated in nC and percentage from Figure 5-20. Standard deviation (%) was calculated by dividing the standard deviation (nC) by the gap in the readout charge between each measured state and the state below.

5.9. Comparison with other optical memory devices

The TMDC optical memory devices in this chapter are designed to respond to light dosages, as presented in Figure 5-9, and show a linear response to exposure dose with a wide LDR and a long retention time. The operating principle of the TMDC monolayer optical memory devices explained in Chapter 5.4 is similar to that of conventional Si-based CCD image sensors. In conventional CCD image sensors, a potential well is created in each pixel by applying a gate voltage. When an image is projected onto the pixel array, each pixel can accumulate electric charge carriers in a potential well and transfer those carriers through a shift register. Similarly, in the TMDC optical memory a potential well is formed by applying a positive voltage pulse devices (Reset operation in Figure 5-9b). Without applying a source-drain bias voltage, the potential well can collect electron charges when light is illuminated on the device and then release these trapped electrons when the source-drain bias is asserted.

Unlike CCD image sensors, a shift register is not needed for the TMDC monolayer optical memory devices because the collection of information is done directly through the source-drain electrodes. Although the LDR of the TMDC monolayer optical memory device (73.4 dB) with a size of 5 x 5 μm^2, obtained in Chapter 5.5, is found to be smaller than that of state-of-the-art CCDs (~90 dB) with a size of 26 x 26 μm^2, it is larger or comparable to consumer grade Si-based CCDs (60~70 dB) with a size of 8 x 8 μm^2[38]. In addition, the dark current can be decreased at a low temperature because it can prevent electrons from being released from trap sites by thermal excitation (Figure 5-17), similar to the phenomena reported in CCD image sensors.[40] In this chapter, only a memory cell has been presented and investigated. However, if a cell array based on TMDC monolayer optical memory devices can

be fabricated in a similar manner to commercial image sensors, it can provide the possibility of producing flexible image sensors combined with other 2D-based electronic devices.

Differences in the operating principle are also found when the TMDC optical monolayer is compared to other optical memory devices such as thin-film phototransistor memories and Schottky barrier-based photoactive memories. The device structure of a TMDC monolayer optical memory is almost the same as that of general thin-film phototransistors. Thus, the TMDC monolayer optical memory devices can also be used as phototransistors, as explained in Figure 5-8. However, while the TMDC monolayer optical devices introduced in this chapter operate without a source-drain bias during the illumination stage, conventional phototransistors and phototransistor memory devices are continuously connected to a constant source-drain voltage bias during the whole operation stage, similar to general photodetectors, in order to maximize the photoresponsivity or photosensitivity. In this case, the ON/OFF ratio and the retention time are much more important than the linear response to light dosage.

Reports on optical memory devices that are designed to respond linearly to light dosage without the application of a source-drain bias during the light illumination have been rarely reported, except for Si-based image sensors. Therefore, it is difficult to directly compare the TMDC monolayer optical memory devices with other comparable optical memory technologies. Although optical memory devices with a much higher ON/OFF ratio over 10^7 and a longer retention time than that of the TMDC monolayer optical memory devices have been already reported[36], they have not shown a linear response to light exposure dose. In this chapter, emphasis has been placed on that the CCD-like operating principle has been applied to non-Si-based 2D phototransistors with a surface treatment to implement a memory cell for image sensors which have a linear response to exposure dosage. Furthermore, it is thought that thin-film phototransistor memory devices based on other channel materials could be designed

according to the operating principle introduced in this chapter if the same structure, specifically, that with a potential well created by a Schottky barrier between the electrodes and surface conditions similar to that explained in Chapter 5.2 and 5.3, can be constructed. This suggests that the operating principle of the TMDC monolayer optical memory devices can be expanded to other thin-film-based optoelectronic memory devices.

5.10. Conclusions

In this chapter, an optical memory device has been proposed and demonstrated based on single-layered MoS_2 through a combination of artificial charge trapping into local potential fluctuations and optically-induced charge generation. By optimizing the potential well structure through a modification of the interface using functional groups that are capable of localizing charge carriers, it was shown that the optical device structure could controllably trap and release electric charges that were stored in trap states, allowing programmable functions for optical memory devices. The OFF-state readout current was found to be of the order of pA while the ON/OFF ratio of the readout charge, which exhibited a linear response, was found to exceed 4700. These combined features make it possible to detect the contrast of an image with 12-bit levels. In addition, it was demonstrated that the device could store an optical signal for more than 10^4 s without applying a source-drain bias, thereby consuming extremely low power before the readout. Furthermore, it was shown that the device could store up to 8 optical states whilst maintaining a linear response. This work enables new opportunities to increase the utilization of TMDC materials with multiple benefits for future optoelectronic applications.

5.11. References

[1] S. B. Desai, S. R. Madhvapathy, A. B. Sachid, J. Llinas, Q. Wang, G. Ahn, G. Pitner, M. J. Kim, J. Bokor, C. Hu, H. S. Wong, A. Javey. MoS2 transistors with 1-nanometer gate lengths. *Science* 354, 99-102 (2016).

[2] J. Wang, Q. Yao, C. W. Huang, X. Zou, L. Liao, S. Chen, Z. Fan, K. Zhang, W. Wu, X. Xiao, C. Jiang, W. W. Wu. High mobility MoS_2 transistor with low Schottky barrier contact by using atomic thick h-BN as a tunneling layer. *Advanced Materials* 28, 8302-8308 (2016).

[3] S. Lei, F. Wen, L. Ge, S. Najmaei, A. George, Y. Gong, W. Gao, Z. Jin, B. Li, J. Lou, J. Kono, R. Vajtai, P. Ajayan, N. J. Halas. An atomically layered InSe avalanche photodetector. *Nano Letters* 15, 3048-3055 (2015).

[4] Y. Xue, Y. Zhang, Y. Liu, H. Liu, J. Song, J. Sophia, J. Liu, Z. Xu, Q. Xu, Z. Wang, J. Zheng, Y. Liu, S. Li, Q. Bao. Scalable production of a few-layer MoS_2/WS_2 vertical heterojunction array and its application for photodetectors. *ACS Nano* 10, 573-580 (2015).

[5] J. Yoon, W. Park, G. Y. Bae, Y. Kim, H. Jang, Y. Hyun, S. Lim, Y. Kahng, W. K. Hong, B. Lee, H. Ko. Highly flexible and transparent multilayer MoS_2 transistors with graphene electrodes. *Small* 9, 3295-3300 (2013).

[6] J. Pu, Y. Yomogida, K.-K. Liu, L.-J. Li, Y. Iwasa, T. Takenobu. Highly flexible MoS_2 thin-film transistors with ion gel dielectrics. *Nano Letters* 12, 4013-4017 (2012).

[7] J. Pu, L.-J. Li, T. Takenobu. Flexible and stretchable thin-film transistors based on molybdenum disulphide. *Physical Chemistry Chemical Physics* 16, 14996-15006 (2014).

[8] O. Lopez-Sanchez, D. Lembke, M. Kayci, A. Radenovic, A. Kis. Ultrasensitive photodetectors based on monolayer MoS_2. *Nature Nanotechnology* 8, 497-501 (2013).

[9] W. Zhang, J. K. Huang, C. H. Chen, Y. H. Chang, Y. J. Cheng, L. J. Li. High-gain phototransistors based on a CVD MoS_2 monolayer. *Advanced Materials* 25, 3456-3461 (2013).

[10] Z. Yin, H. Li, H. Li, L. Jiang, Y. Shi, Y. Sun, G. Lu, Q. Zhang, X. Chen, H. Zhang. Single-layer MoS_2 phototransistors. *ACS Nano* 6, 74-80 (2012).

[11] H. S. Lee, S.-W. W. Min, Y.-G. G. Chang, M. K. Park, T. Nam, H. Kim, J. H. Kim, S. Ryu, S. Im. MoS_2 nanosheet phototransistors with thickness-modulated optical energy gap. *Nano Letters* 12, 3695-3700 (2012).

[12] X. Gong, M. Tong, Y. Xia, W. Cai, J. Moon, Y. Cao, G. Yu, C.-L. Shieh, B. Nilsson, A. J. Heeger. High-detectivity polymer photodetectors with spectral response from 300 nm to 1450 nm. *Science* 325, 1665-1667 (2009).

[13] Y. Wen, L. Yin, P. He, Z. Wang, X. Zhang, Q. Wang, T. Shifa, K. Xu, F. Wang, X. Zhan, F. Wang, C. Jiang, J. He. Integrated high-performance infrared phototransistor arrays composed of nonlayered PbS–MoS_2 heterostructures with edge contacts. *Nano Letters* (2016).

[14] D. J. Late, B. Liu, R. H. S. S. Matte, V. P. Dravid, C. N. R. Rao. Hysteresis in single-layer MoS_2 field effect transistors. *ACS Nano* 6, 5635-5641 (2012).

[15] T. Li, G. Du, B. Zhang, Z. Zeng. Scaling behavior of hysteresis in multilayer MoS_2 field effect transistors. *Applied Physics Letters* 105, 93107 (2014).

[16] S. Najmaei, X. Zou, D. Er, J. Li, Z. Jin, W. Gao, Q. Zhang, S. Park, L. Ge, S. Lei, J. Kono, V. B. Shenoy, B. I. Yakobson, A. George, P. M. Ajayan, J. Lou. Tailoring the physical properties of molybdenum disulfide monolayers by control of interfacial chemistry. *Nano Letters* 14, 1354-1361 (2014).

[17] X. Wang, P. Wang, J. Wang, W. Hu, X. Zhou, N. Guo, H. Huang, S. Sun, H. Shen, T. Lin, M. Tang, L. Liao, A. Jiang, J. Sun, X. Meng, X. Chen, W. Lu, J. Chu. Ultrasensitive and broadband MoS_2 photodetector driven by ferroelectrics. *Advanced Materials* 27, 6575-6581 (2015).

[18] M. Choi, G.-H. Lee, Y.-J. Yu, D.-Y. Lee, S. Lee, P. Kim, J. Hone, W. Yoo. Controlled charge trapping by molybdenum disulphide and graphene in ultrathin heterostructured memory devices. *Nature Communications* 4, 1624 (2013).

[19] S. Bertolazzi, D. Krasnozhon, A. Kis. Nonvolatile memory cells based on MoS_2/graphene heterostructures. *ACS Nano* 7 (2013).

[20] M. Chen, H. Nam, S. Wi, G. Priessnitz, I. Gunawan, X. Liang. Multibit data storage states formed in plasma-treated MoS_2 transistors. *ACS Nano* 8 (2014).

[21] J. Wang, X. Zou, X. Xiao, L. Xu, C. Wang, C. Jiang, J. C. Ho, T. Wang, J. Li, L. Liao. Floating gate memory-based monolayer MoS_2 transistor with metal nanocrystals embedded in the gate dielectrics. *Small* 11, 208-213 (2015).

[22] K. Roy, M. Padmanabhan, S. Goswami, P. T. Sai, G. Ramalingam, S. Raghavan, A. Ghosh. Graphene-MoS_2 hybrid structures for multifunctional photoresponsive memory devices. *Nature Nanotechnology* 8, 826-830 (2013).

[23] S. Lei, F. Wen, B. Li, Q. Wang, Y. Huang, Y. Gong, Y. He, P. Dong, J. Bellah, A. George, L. Ge, J. Lou, N. J. Halas, R. Vajtai, P. M. Ajayan. Optoelectronic memory using two-dimensional materials. *Nano Letters* 15, 259-265 (2015).

[24] S. Najmaei, Z. Liu, W. Zhou, X. Zou, G. Shi, S. Lei, B. I. Yakobson, J.-C. Idrobo, P. M. Ajayan, J. Lou. Vapour phase growth and grain boundary structure of molybdenum disulphide atomic layers. *Nature Materials* 12, 754-759 (2013).

[25] A. M. van der Zande, P. Y. Huang, D. A. Chenet, T. C. Berkelbach, Y. You, G.-H. Lee, T. F. Heinz, D. R. Reichman, D. A. Muller, J. C. Hone. Grains and grain boundaries in highly crystalline monolayer molybdenum disulphide. *Nature Materials* 12, 554-561 (2013).

[26] Y. H. Lee, X. Q. Zhang, W. Zhang, M. T. Chang, C. T. Lin, K. D. Chang, Y. C. Yu, J. Wang, C. S. Chang, L. J. Li, T. W. Lin. Synthesis of large-area MoS_2 atomic layers with chemical vapor deposition. *Advanced Materials* 24 (2012).

[27] G.-H. H. Lee, Y.-J. J. Yu, X. Cui, N. Petrone, C.-H. H. Lee, M. S. Choi, D.-Y. Y. Lee, C. Lee, W. J. Yoo, K. Watanabe, T. Taniguchi, C. Nuckolls, P. Kim, J. Hone. Flexible and transparent MoS_2 field-effect transistors on hexagonal boron nitride-graphene heterostructures. *ACS Nano* 7, 7931-7936 (2013).

[28] J. Jeon, S. Jang, S. Jeon, G. Yoo, Y. Jang, J.-H. Park, S. Lee. Layer-controlled CVD growth of large-area two-dimensional MoS_2 films. *Nanoscale* 7, 1688-1695 (2014).

[29] K. Dolui, I. Rungger, S. Sanvito. Origin of the n-type and p-type conductivity of MoS_2 monolayers on a SiO_2 substrate. *Physical Review B* 87 (2013).

[30] S. Ghatak, A. Pal, A. Ghosh. Nature of electronic states in atomically thin MoS_2 field-effect transistors. *ACS Nano* 5, 7707-7712 (2011).

[31] K. Mak, K. He, C. Lee, G. Lee, J. Hone, T. F. Heinz, J. Shan. Tightly bound trions in monolayer MoS_2. *Nature Materials* 12, 207-211 (2012).

[32] M. M. Furchi, D. K. Polyushkin, A. Pospischil, T. Mueller. Mechanisms of photoconductivity in atomically thin MoS_2. *Nano Letters* 14, 6165-6170 (2014).

[33] C. Lan, C. Li, Y. Yin, Y. Liu. Large-area synthesis of monolayer WS_2 and its ambient-sensitive photo-detecting performance. *Nanoscale* 7, 5974-5980 (2015).

[34] N. R. Pradhan, J. Ludwig, Z. Lu, D. Rhodes, M. M. Bishop, K. Thirunavukkuarasu, S. A. McGill, D. Smirnov, L. Balicas. High photoresponsivity and short photoresponse times in few-layered WSe_2 transistors. *ACS Applied Materials & Interfaces* 7 (2015).

[35] A. Abderrahmane, P. J. Ko, T. V. Thu, S. Ishizawa, T. Takamura, A. Sandhu. High photosensitivity few-layered $MoSe_2$ back-gated field-effect phototransistors. *Nanotechnology* 25 (2014).

[36] S. Jeon, S.-E. Ahn, I. Song, C. Kim, U. I. Chung, E. Lee, I. Yoo, A. Nathan, S. Lee, K. Ghaffarzadeh, J. Robertson, K. Kim. Gated three-terminal device architecture to eliminate persistent photoconductivity in oxide semiconductor photosensor arrays. *Nature Materials* 11, 301-305 (2015).

[37] A. Vijayaraghavan, S. Kar, C. Soldano, S. Talapatra, O. Nalamasu, P. M. Ajayan. Charge-injection-induced dynamic screening and origin of hysteresis in field-modulated transport in single-wall carbon nanotubes. *Applied Physics Letters* 89, 162108 (2006).

[38] M. V. Konnik, E. A. Manykin, S. N. Starikov. Optical-digital correlator with increased dynamic range using spatially varying pixels exposure technique. *Optical Memory and Neural Networks* 18, 61-71 (2009).

[39] K. C. Gendreau, G. Y. Prigozhin, R. K. Huang, M. W. Bautz. A technique to measure trap characteristics in CCD's using X-rays. *IEEE Transactions on Electron Devices* 42, 1912-1917 (1995).

[40] N. S. Saks. A technique for suppressing dark current generated by interface states in buried channel CCD imagers. *IEEE Electron Device Letters* 1, 131-133 (1980).

[41] T. Leydecker, M. Herder, E. Pavlica, G. Bratina, S. Hecht, E. Orgiu, P. Samorì. Flexible non-volatile optical memory thin-film transistor device with over 256 distinct levels based on an organic bicomponent blend. *Nature Nanotechnology* 11, 769-775 (2016).

6. Conclusions

6.1. Summary

This thesis has focused mainly on investigating the synthesis and the electronic applications of TMDC monolayers and heterostructures/alloys. In order to achieve these goals, the following experiments have been conducted: (1) synthesis and understanding of large-sized and highly crystalline TMDC monolayers under thermally stable conditions via a solution-processed precursor deposition, and characterization of MoS_2/WS_2 vertical heterostructured devices, (2) synthesis and understanding of TMDC lateral heterostructures and alloys, controlling various growth parameters, and (3) fabrication of MoS_2 monolayer optical memory devices.

For the growth of TMDC monolayers, the low supersaturation level, triggered by the evaporation of an extremely thin precursor layer, reduces the nucleation density dramatically under a thermodynamically stable environment, yielding uniform and clean monolayer films and large crystal sizes. As a result, the resultant PL spectrum exhibits a significantly small full-width-half-maximum, comparable to that of exfoliated and suspended TMDC monolayer crystals. It is confirmed that this growth procedure can be extended to the synthesis of other TMDC monolayers, and robust MoS_2/WS_2 heterojunction devices have been readily prepared, using this synthetic procedure, due to the large-sized crystals. The heterojunction devices show a fast response time and a significantly high photoresponsivity because of the built-in potential and the majority carrier transport at the unipolar n-n junction. These findings indicate an efficient pathway for the fabrication of high-performance 2D optoelectronic devices.

The solution-processed precursor deposition technique has been extended to the one-step CVD synthesis of lateral core/shell-structured MoS_2/WS_2 heterostructures and $Mo_{1-x}W_xS_2$ alloys, through the precise control of the timing for introduction of the precursors and the supersaturation level of all the precursors. The metal oxide precursors can be vaporized controllably with this growth strategy, thus a variety of types of heterostructures and alloys have been synthesized. In addition, the crystal size of the heterostructures was increased up to 160 μm. Raman/PL spectra and TEM results have shown that high-quality heterostructures can be grown using this growth method. Specifically, a one-step synthesis prevents the exposure of the crystal to ambient environments during the growth procedure and provides a relatively clear interface between the core and the shell layers, compared to the two-step growth process. In addition, alloyed monolayer structures are easily obtained by vaporizing all of the precursors simultaneously. Interestingly, bound excitons are observed in the alloyed region using low-temperature PL measurements because of the trapped sites that are formed from the random distribution of Mo and W atoms.

Finally, monolayer MoS_2 optical memory devices based on artificially-structured charge trap layers have been presented. The charge trap sites are intentionally introduced by the functionalization of the monolayer/dielectric interfaces, leading to localized electronic states in the electronic band structure. As a result, the optical memory devices can be operated on the basis of electrically-induced charge trapping and optically-mediated charge release. It is found that the optical memory devices exhibit excellent photo-responsive memory characteristics with a large linear dynamic range coupled with a low OFF-state current, and a long storage lifetime. Additionally, the multi-level storage capability of up to 8 optical states

is successfully demonstrated. These results represent a significant step toward the development of future monolayer optoelectronic memory devices.

6.2. Future work

In this thesis, the synthesis of TMDC monolayers and the fabrication of useful TMDC monolayer devices have been investigated. However, this research area is still in its early stages with several major challenges ahead. Therefore, it is believed that much more effort is required to make further progress in the field of TMDC monolayers in the near future.

From the point of view of material synthesis, the growth of semiconducting TMDC monolayer is far less mature, particularly when compared to graphene. Even though the strategy for growing large-sized TMDC monolayers (centimetre level) has been suggested in this study, a way to increase the size of the TMDC films up to the metre scale still needs to be developed. In addition, the size of the single crystals (< 1 mm) is still far smaller than that of single crystalline graphene (centimetre level). It is, therefore, highly desirable to increase the size of the single crystalline domains because grain boundaries can have a significantly detrimental effect when operating TMDC monolayer-based electronic and optoelectronic devices. Finally, there are still some ambiguities regarding the growth mechanism of the TMDC monolayers, especially regarding the role of the substrates. Therefore, the effects of various substrates on the nucleation behaviour and the grain size should be studied in the future.

Furthermore, in terms of device applications, much more work is needed to solve several problems regarding the utilization of TMDC monolayers as building blocks for practical electronic and optoelectronic devices. Most of the MoS_2-based devices reported to

date exhibit only n-type properties. It is highly desirable to achieve ambipolar conduction so as to fabricate a variety of practical devices based on p-n junctions. Therefore, further investigations on the p-n junctions between n-type TMDC monolayers and other p-type 2D materials such as black phosphorous should be conducted in great detail.

As this thesis has demonstrated, atomically thin TMDC semiconducting monolayers have emerged as one of the potential candidates to overcome the limitations of semi-metallic graphene. Still, a lot of exciting and interesting work remains in the area of the 2D materials. It is believed that it is just a matter of time when advanced technology based on 2D materials will exceed the limits of current silicon-based electronics and optoelectronics in the future.

List of Publications

First author papers

1. **J. Lee**, S. Pak, Y.-W. Lee, Y. Cho, J. Hong, P. Giraud, H. Shin, S. Morris, J. Sohn, S. Cha, J. M. Kim. Monolayer optical memory cells based on artificial trap-mediated charge storage and release. *Nature Communications* **8**, 14734 (2017).
2. **J. Lee**, S. Pak, P. Giraud, Y. Lee, Y. Cho, J. Hong, A. Jang, H. Chung, W. Hong, H. Jeong, H. Shin, L. Occhipinti, S. Morris, S. Cha, J. Sohn, J. M. Kim. Thermodynamically stable synthesis of large-scale and highly crystalline transition metal dichalcogenide monolayers and their unipolar n–n heterojunction devices. *Advanced Materials* 29, 1702206 (2017) *(Front Cover).*
3. **J. Lee** et al. One-step synthesis of lateral MoS_2 and WS_2 heterostructured and alloyed monolayers via a solution-processed precursor deposition. *Submitted.*

Co-author papers

1. Y. –W. Lee, J. Hong, G. –H. Ah, S. Pak, **J. Lee**, Y. Cho, S. Lee , S. Cha, J. I. Sohn, J. M. Kim, "Synergistic Effects of Engineered Spinel Hetero-Metallic Cobaltites on Electrochemical Pseudo-Capacitive Behaviors", *Journal of Materials Chemistry A*, 6, 15033-15039 (2018).
2. Y. Cho, B. Hou, J. Lim, S. Lee, S. Pak, J. Hong, P. Giraud, A. –R. Jang, Y. –W. Lee, **J. Lee**, J. E. Jang, H. J. Snaith, S. M. Morris, J. I. Sohn, S. Cha, J. M. Kim, "Balancing Charge Carrier Transport in a Quantum Dot P-N Junction toward Hysteresis-Free High Performance Solar Cells", *ACS Energy Letters*, 3, 1036-1043 (2018).
3. A. –R. Jang, Y. –W. Lee, S. –S. Lee, J. Hong, S. –H. Beak, S. Pak, **J. Lee**, H. S. Shin, D. Ahn, W. –K. Hong, S. Cha, J. I. Sohn, I. –K. Park, "Electrochemical and electrocatalytic reaction characteristics of boron-incorporated graphene via a simple spin-on dopant process", *Journal of Materials Chemistry A*, 6, 7351-7356 (2018).
4. Y. Cho, P. Giraud, B. Hou, Y. -W. Lee, J. Hong, S. Lee, S. Pak, **J. Lee**, J. E. Jang, S. M. Morris, J. I. Sohn, S. Cha, J. M. Kim, "Charge Transport Modulation of a Flexible

Quantum Dot Solar Cell using a Piezoelectric Effect", *Advanced Energy Materials*, 8 1700809 (2018).

5. S. Pak, **J. Lee**, Y. -W. Lee, A. -R. Jang, S. Ahn, K. Y. Ma, Y. Cho, J. Hong, S. Lee, H. Y. Jeong, H. Im, H. S. Shin, S. M. Morris, S. Cha, J. I. Sohn, J. M. Kim. Strain-mediated interlayer coupling effects on the excitonic behaviors in an epitaxially-grown MoS_2/WS_2 van der Waals heterobilayer. *Nano Letters* 17, 5634-5640 (2017).
6. E. M. Alexeev, A. Catanzaro, O. V. Skrypka, P. K. Nayak, S. Ahn, S. Pak, **J. Lee**, J. I. Sohn, K. S. Novoselov, H. S. Shin, and A. I. Tartakovskii. Imaging of interlayer coupling in van der Waals heterostructures using a bright-field optical microscope. *Nano Letters* 17, 5342-5349 (2017).
7. J. Hong, Y.-W. Lee, D. Ahn, S. Pak, **J. Lee**, A. -R. Jang, S. -H. Lee, B. Hou, Y. Cho, S. M. Morris, H. S. Shin, S. Cha, J. I. Sohn, J. M. Kim. Highly stable 3D porous heterostructures with hierarchically-coordinated octahedral transition metals for enhanced performance supercapacitors. *Nano Energy* 39, 337-345 (2017).
8. Y. -W. Lee, B. -S. Kim, J. Hong, H. Choi, H. -S. Jang, B. Hou, S. Pak, **J. Lee**, S. -H. Lee, S. M. Morris, D. Whang, J. P. Hong, H. S. Shin, S. Cha, J. I. Sohn, J. M. Kim. Hierarchically assembled tubular shell-core-shell heterostructure of hybrid transition metal chalcogenides for high-performance supercapacitors with ultrahigh cyclability. *Nano Energy* 37, 15-23 (2017).
9. J. Hong, Y. -W. Lee, B. Hou, W. Ko, **J. Lee**, S. Pak, J. P. Hong, S. M. Morris, S. Cha, J. I. Sohn, and J. M. Kim. Solubility-dependent $NiMoO_4$ nanoarchitectures: Direct correlation between rationally designed structure and electrochemical pseudokinetics. *ACS Applied Materials & Interfaces* 8, 35227–35234 (2016).
10. J. Hong, B. Hou, J. Lim, S. Pak, B. -S. Kim, Y. Cho, **J. Lee**, Y. -W. Lee, P. Giraud, S. Lee, J. B. Park, S. M. Morris, H. J. Snaith, J. I. Sohn, S. Cha, J. M. Kim. Enhanced charge carrier transport properties in colloidal quantum dots solar cells via organic and inorganic hybrid surface passivation. *Journal of Material Chemistry A* 4, 18769-18775 (2016).
11. Y.-W. Lee, G. -H. An, B. -S. Kim, J. Hong, S. Pak, E. -H. Lee, Y. Cho, **J. Lee**, P. Giraud, S. Cha, H. -J. Ahn, J. I. Sohn, and J. M. Kim. Synergistic effects of a multifunctional graphene based interlayer on electrochemical behavior and structural stability. *ACS Applied Materials & Interfaces* 8, 17651-17658 (2016).

12. Y. -W. Lee, B. -S. Kim, J. Hong, **J. Lee**, S. Pak, H. -S. Jang, D. Whang, S. Cha, J. I. Sohn, J. M. Kim. A pseudo-capacitive chalcogenide-based electrode with dense 1-dimensional nanoarrays for enhanced energy density in asymmetric supercapacitors. *Journal of Materials Chemistry A* 4, 10084-10090 (2016).
13. Y. -W. Lee, G. –H. An, S. Lee, J. Hong, B. -S. Kim, **J. Lee**, D. -H. Kwak, H. -J. Ahn, W. Huh, S. Cha, K. -W. Park, J. I. Sohn, J. M. Kim. Synergistic incorporation of hybrid heterobimetal-nitrogen atoms into carbon structures for superior oxygen electroreduction performances. *Catalysis Science & Technology* 6, 2085-2091 (2016).
14. Y. Cho, J. B. Park, B. -S. Kim, **J. Lee**, W. -K. Hong, I. -K. Park, J. E. Jang, J. I. Sohn, S. Cha, J. M. Kim. Enhanced energy harvesting based on surface morphology engineering of P(VDF-TrFE) film. *Nano Energy* 16, 524–532 (2015).